# NUMERICAL SIMULATION OF FLOW THROUGH A PIPING SYSTEM - RECIRCULATION AND MIXING

A Dissertation

by

BYUNG-HEE CHOI

Submitted to the Graduate and Professional School of
Texas A&M University
in partial fulfillment of the requirements for the degree of

DOCTOR OF PHILOSOPHY

| | |
|---|---|
| Chair of Committee, | N.K. Anand |
| Co-Chairs of Committee, | Yassin A. Hassan |
| Committee Members, | Duy Thien Nguyen |
| | Sharath Girimaji |
| | Piyush Sabharwall |
| Head of Department, | Guillermo Aguilar |

August 2022

Major Subject: Mechanical Engineering

# ABSTRACT

This research presents the methodology and the results of numerical studies on turbulent flows in a piping system that resembles the geometry of the Fission Product Venting System (FPVS) in High-Temperature Gas-Cooled Fast Reactors (HTGR). The fission product includes graphite particulates carried by coolant as flows through the core and fission gases like Krypton, Xenon, Cesium, and Iodine produced from thermonuclear reaction. Knowing the location of mixing and the magnitude of various gaseous components is necessary to manage and mitigate the adverse effects of fission products on power generation. In this work, scaling analysis was used to identify the geometry, surrogate gases, and surrogate particles. The turbulent flow fields in the piping system were simulated using the openFOAM v7 and Large Eddy Simulation (LES). The grid independence was established using the Grid Convergence Index (GCI) concept. In addition, numerical simulations were validated against the experimental data and the Direct Numerical Simulation (DNS) data reported in the literature. The quantities of interest, such as reattachment length and critical point of flows through axisymmetric expansion and the Absolute Mixing Index (AMI) through a piping system with 90 deg bend, were calculated. The reattachment length represents the length of the recirculation region, and the critical points ($Cr_1$ and $Cr_2$) represent the cross-over points from laminar to transition region, and the transition region to turbulent flow. A series of parametric runs were made by varying flow Reynolds number ($Re$), turbulence intensity (TI) at the inlet, and surrogate gas concentration at the injection point. Using the parametric runs design, correlation expressions for reattachment length and the critical point were developed. The gradient of $\log_{10}$AMI represents the mixing rate, and the highest value is observed downstream of the pipe's expansion. The AMI is the standard deviation of the concentration of the surrogate gas Argon in the piping system. The Proper Orthogonal Decomposition (POD) technique was used to study the coherent turbulent structure downstream of a sudden expansion. Finally, simulation of the surrogate solid particles was carried out using the Lagrangian approach. The deposition velocity particles in a square horizontal channel were estimated using a discrete random walk model.

# DEDICATION

To my mother, father and sister

# ACKNOWLEDGMENTS

I would like to thank my committee chair, Dr. Anand, my committee co-chair Dr. Hassan, and my committee Dr. Nguyen, Dr. Girimaji and Dr. Sabharwall. Thanks to my colleagues, Daniel and Reynoldo for performing experimental work required in my research. Thanks to my colleague, Robert for understanding me POD technique. Thanks to my friends SeungHwan, SeRo, WooSeok, JunSur, MoonJoo and ChangKyu. I was able to overcome adversity. Finally, thanks to my family for their encouragement and limitless support.

CONTRIBUTORS AND FUNDING SOURCES

## Contributors

This work was supported by dissertation committee consisting of Professor N.K. Anand [advisor], Yassin A. Hassan [co-advisor], Sharath Girimaji, Piyush Sabharwal of the Department of Mechanical Engineering and Professor Duy Thien Nguyen of the Department of Nuclear Engineering.

The experimental measurement of fluid flow and particle velocity profiles for Chapter II, IV and V was provided by Daniel Orea and Reynolds Chavez and were published in (2020) in an article listed in the Journal of Aerosol Science and Technology.

All other work conducted for this dissertation was completed by the student independently.

## Funding Sources

Graduate study was supported by Idaho National Laboratory (INL). INL's work was supported by the U.S. Department of Energy, Office of Nuclear Energy under Contract Number DE-AC07-05ID14517. The work reported in this summary is the result of ongoing efforts supporting the Versatile Test Reactor.

Portions of this research were conducted with the advanced computing resources provided by Texas A&M High Performance Research Computing.

NOMENCLATURE

**Acronym**

| | |
|---|---|
| ARSM | algebraic Reynolds stress model |
| CFD | Computational Fluid Dynamics |
| CFL | Courant-Friedrichs-Lewy value |
| CL | Cartridge Loop |
| DNS | Direct Numerical Simulation |
| DRW | Discrete Random Walk Model |
| FPVS | Fission Product Venting System |
| GFR | Gas Cooled Fast Reactor |
| HTA | High-Temperature absorber |
| LB model | Lam-Bremhors low-Reynolds number $k$-$\epsilon$ Model |
| LC model | Lien-Chen-Leschziner low-Reynolds number $k$-$\epsilon$ Model |
| LDA | Laser Doppler anemometer |
| LES | Large Eddy Simulation |
| LL model | Lien-Leschziner low-Reynolds number $k$-$\epsilon$ Model |
| LPLT | Low Pressure Low Temperature |
| LRR model | Launder-Reece-Rod RSTM Model |
| LS model | Launder-Sharma low-Reynolds number $k$-$\epsilon$ Model |
| MRI | Magnetic resonance imaging |
| NS | Numerical Simulation |
| PIV | Particle Image Velocimetry |
| POD | Proper Orthogonal Decomposition |

| | |
|---|---|
| RANS | Reynolds Averaged Navier-Stokes |
| RMS | Root Mean Square |
| RSTM | Reynolds Stress Transport Model |
| SSG model | Speziale-Sarkar-Gatski RSTM Model |
| STD model | Standard k-epsilon model |
| TKE | Turbulence Kinetic Energy |
| UVP | Ultrasonic Velocity Profiling |
| VTR | Versatile Test Reactor |
| WALE model | LES Wall-adapting local eddy-viscosity Model |

**Variables**

| | |
|---|---|
| AMI | Absolute Mixing Index |
| $C_0$ | Particle Concentration near the wall |
| $C_c$ | Cunningham correction factor |
| $C_D$ | Schiller-Naumann drag correlation |
| $Cr_1$ | Critical point 1 for laminar-transition |
| $Cr_2$ | Critical point 2 for transition-turbulent |
| CR | Curvature Ratio, $D/2R_c$ |
| $d$ | Diameter of small pipe |
| $d_p$ | Diameter of particle |
| $D$ | Diameter of large pipe |
| $D_h$ | Hydraulic diameter |
| $D_p$ | Particle mass diffusivity |
| ER | Expansion Ratio $D/d$ |
| GCI | Grid Convergence Index, GCI= $F_s\epsilon/(r^p - 1)$ |

| | |
|---|---|
| $f_D$ | Darcy friction factor |
| $f_1$ | Damping factor 1 |
| $f_2$ | Damping factor 2 |
| $f_\mu$ | Damping factor $\mu$ |
| $F_d$ | Drag Force |
| $F_g$ | Gravity Force |
| $g$ | Gravity acceleration |
| $h$ | Step height $(D-d)/2$ for a sudden expansion |
| $h$ | Half of the height for a square duct |
| $J$ | Particle flux to the wall |
| $k$ | Turbulence Kinetic Energy |
| $U$ | Instantaneous velocity, $U = \bar{U} + u$ |
| $u$ | Fluctuation velocity |
| $u_{rms}$ | Root mean square of fluctuation velocity |
| $u_d^+$ | Non-dimensionless deposition velocity |
| $\overline{u_i u_j}$ | Reynolds stress |
| $\overline{U}$ | Temporal-averaged velocity |
| $U_\tau$, $U^*$ | Friction velocity |
| $U_b$ | Bulk velocity |
| $U_c$ | Centerline velocity |
| $U_f$ | Fluid velocity |
| $U_{in}$ | Inlet velocity |
| $U_{old}$ | Velocity of previous time step |
| $U_p$ | Particle velocity |
| $U_{ref}$ | Reference velocity |

| | |
|---|---|
| $Lr$ | Reattachment length |
| $m$ | Mass |
| $\dot{m}_i$ | Mass flow rate at the inlet |
| $\dot{m}_p$ | Mass flow rate at the porous wall |
| $p$ | Pressure |
| $p1$, $p2$, $p3$, and $p4$ | Pattern 1, 2, 3 and 4, respectively |
| $P_k$ | Production term |
| $R_c$ | Radius of curvature for pipe bend |
| $Re$, $Re_b$ | Reynolds number, $U_b d/\nu$ |
| $Re_c$ | Critical Reynolds number |
| $Re_\tau$ | Friction Reynolds number, $U^* h/\nu$ |
| $Re_p$ | Particle Reynolds number, $d_p\|U_f - U_p\|/v$ |
| $\mathbb{R}$ | Random function ranged between -0.5 to 0.5 |
| $S$ | Universal solution expression of $Lr$ |
| $S_L$ | Solution expression of $Lr$ for laminar region, $S_L = A(Re - B)$ |
| $S_T$ | Solution expression of $Lr$ for turbulent region, $S_T = C/Re + D$ |
| $Sc$ | Schmidt number, $\nu/D_p$ |
| $Stk$ | Stokes number, $\frac{\tau_p}{\tau_f} = \frac{\rho_p d_p^2 C_c}{18\mu}\frac{U_f}{W}$ |
| TI, $I$ | Turbulence Intensity [%] |
| $w_i$ | Mass fraction of i |
| $\overline{w}_i$ | Temporal-averaged mass fraction of species i |
| $\langle w_i \rangle$ | Spatial-averaged mass fraction of species i over cross-section area |
| $W$ | width/height of square duct |
| $\delta$ | Flow disturbance |
| $\epsilon$ | Dissipation rate |

| | |
|---|---|
| $\epsilon_r$ | Absolute pipe roughness |
| $\lambda$ | Intermittency factor |
| $\lambda^{(i)}$ | POD eigenvalue |
| $\nu$ | Kinematic viscosity |
| $\nu_t$ | turbulent viscosity |
| $\xi^{(i)}(t)$ | Temporal POD coefficient |
| $\rho$, $\rho_f$ | Density of fluid |
| $\rho_p$ | Density of particle |
| $\sigma_w$ | standard deviation of mass fraction over a cross-section |
| $\tau_{ij}$ | Reynolds stress |
| $\tau_w$ | Wall shear stress |
| $\tau_f$ | Flow relaxation time, $\frac{W}{U_b}$ |
| $\tau_p$ | Particle relaxation time, $\frac{\rho_p d_p^2 C_c}{18\mu}$ |
| $\tau^+$ | Particle relaxation time, normalized, $\frac{d_p^2 (u_\tau^*)^2 \rho_p C_c}{18\nu^2 \rho_f}$ |
| $\psi^{(i)}(x)$ | POD eigenmode |
| $\overline{x}$ | Temporal-averaged variables |
| $\tilde{x}$ | Filtered variables |

TABLE OF CONTENTS

Page

LIST OF FIGURES

FIGURE Page

LIST OF TABLES

# 1. INTRODUCTION

The main objective of this dissertation study is to characterize transport of fission products in High Temperature Gas-cooled Fast Reactors (GFR). Fission products include both particulate matter and fission gases such as krypton, xenon, cesium, iodine, and the like. These fission products are removed from the primary loop to prevent the deterioration of the thermal performance of gas-cooled reactors. The Fission Product Venting System (FPVS) of GFR remove both particulate and gaseous fission products. To accommodate these studies in an university environment a scaling analysis was performed to determine geometry of the experimental setup that would mimic the FPVS, thermodynamic operating conditions, and surrogate particles and gases. The test facility of the scaled FPVS contains two distinct geometric features: flow and mixing downstream of an expansion and $90^{\circ}$ bends. A detailed numerical studies were performed using scaled geometric and thermodynamic parameters. Turbulent mixing studies were conducted using surrogate primary coolant and fission gases. The studies reported in this dissertation focus on characterizing the transport of fission products in gas-cooled fast reactors; the results of this study are sufficiently applicable to heat exchangers, microfluidic devices, and biomechanics applications.

Computational Fluid Dynamics (CFD) is a versatile tool for understanding and characterizing turbulent flow and mixing through complex geometries. Unlike the experimental study, the CFD techniques have very few limitation for examining the flow characteristics furthermore, it is very economical and safe compared to conducting experiments at extreme temperatures and pressures with toxic fluids. In the last couple of decades, advancements in the computer hardware have made the Large Eddy Simulation (LES) and Direct Numerical Simulation (DNS) techniques ubiquitous to study turbulent flows. Further, the a deeper insights into the coherent turbulence structure can be obtained by decomposing stack data using the proper orthogonal decomposition (POD) technique.

chapter 2 discusses turbulence models used for flows confined by the wall. The validation for Reynolds Averaged Navier-Stokes (RANS) and LES models made for confined flows are evaluated. Numerical results with models such as the low Reynolds number turbulence model, Reynolds

Stress Transport Model (RSTM), and Wall-Adopting Local Eddy viscosity model (WALE) are compared with the experimental measurements of developing flows [1] and DNS reference data for the fully developed flows [2, 3]. Chapter 3 reports the results of the LES of flow through an axisymmetric sudden expansion. The effects of the inlet condition, such as the Reynolds number ($Re$) and turbulence intensity (TI) at the inlet, were investigated with respect to the reattachment length $Lr$. Two critical points, demarcating laminar, transition, and turbulence regions, were found and their correlation was suggested as a function of Reynolds number and turbulence intensity at the inlet. Next, the universal correlation for the reattachment length was suggested and found to have a good agreement with the experimental data reported in the literature [4, 5]. To enhance the understanding of the coherent turbulence structure, the Proper Orthogonal Decomposition (POD) analysis was performed and results are reported. Flow characteristics obtained using the POD analysis were found to be similar to the experimental data. Chapter 4 presents the validated numerical model for the pipe flow used to simulate the flow of the isothermal multicomponent gas in a scaled low-pressure, low-temperature test facility of the Fission Product Venting System (FPVS) of a Gas Cooled Fast Reactor (GFR). The geometry of the FPVS test facility was an open loop that includes the gradual expansion coupling and two 90° pipe elbows. The surrogate primary fluid, air, flows throughout the pipe while surrogate fission gas, argon, was injected through a porous wall to study mixing. The concept of Absolute Mixing Index (AMI) was used to characterize mixing and its slope was used to characterize the mixing rate in a scaled FPVS. Chapter 5 shows the numerical simulation of the transport of surrogate particles through a rectangular channel. The numerical studies included the prediction of the turbulent flow field in the Eulerian frame of reference using the RSTM Model and tracking surrogate particles using a Langrangian frame of reference. Deposition velocity of particles was predicted and compared with references. Particle penetration through the channel was determined by tracking the trajectories of a large number of particles to obtain penetration efficiency independent of the number of tracked particles. The details of the methodology and results are presented in Chapter 5. Finally, the conclusions of this study are reported in Chapter 6.

# 2. TURBULENCE MODELS FOR CHANNEL FLOWS

In this chapter a variety of turbulence models such as the modified $k - \epsilon$ model, Reynolds Stress Transport model (RSTM), and Large Eddy Simulation (LES) are evaluated by comparing model predictions with the Direct Numerical Simulation (DNS) results and the experimental data for channel flows reported in the literature.

## 2.1 Turbulence model for flow through a pipe

The continuity and Navier-Stokes equations mathematically describe the conservation of mass and momentum for fluid flow that fulfils the continuum hypothesis (Eqs. 2.1 and 2.2). The Direct Numerical Simulation (DNS) technique is the most straight forward approach to numerically solve Navier-Stokes equations and to resolve fine turbulent flow structures. DNS studies are considered to be the most accurate compared to other modeling techniques, because all small turbulent scales are resolved. However, performing DNS is not computationally efficient. Each mesh in the domain should be smaller than the Kolmogorov scale to capture the smallest turbulence structure, which requires a large amount of computational power. Therefore, It is important to identify a turbulence model that is both reasonably accurate and computationally efficient. There are several DNS studies of pipe flows reported in the literature. Eggel [3] performed a DNS study for circular pipe, and Gavrilakis [2] was the first to perform a DNS study of square duct flow with a low Reynolds number of $Re_\tau$ = $hu_\tau/\nu$ = 150 (where $h$ is the half-width of a square channel, $u_\tau = (\tau_w/\rho)^{0.5}$ is the mean friction velocity, $\rho$ is the fluid density and $\tau_w$ is the mean wall shear stress). Zhang [6] performed a DNS study of square duct flow with a Reynolds number of up to $Re_\tau$ = 600, and Pirozzoli [7] conducted a DNS study with a Reynold number of up to $Re_\tau$=1,000 and elucidated the physical phenomena in the square duct flow based on the DNS result. Uhlmann [8] conducted a DNS study at a low Reynolds number to determine the minimal requirements for self-sustaining turbulence, which yielded a minimum $Re_\tau$ of 80 (equivalent to a bulk Reynolds number of 2,200). Sekimoto [9] performed a DNS study with a temperature gradient between walls, showing that the

shape of the secondary vortices changed as the temperature gradient became severe.

$$\frac{\partial U_i}{\partial t} + \frac{\partial U_i}{\partial x_i} = 0 \tag{2.1}$$

$$\frac{\partial U_i}{\partial t} + \frac{\partial U_i U_j}{\partial x_i} = -\frac{\partial p}{\partial x_i} + \frac{\partial}{\partial x_i}\left[\nu\left(\frac{\partial U_i}{\partial x_j} + \frac{\partial U_j}{\partial x_i}\right)\right] \tag{2.2}$$

### 2.1.1 Low Reynolds number RANS model

The Reynolds-averaged Navier–Stokes (RANS) model consists of time-averaged equations of motion for fluid flow, wherein flow quantities are decomposed into time-averaged and fluctuation components. By calculating turbulence quantities (e.g. Reynolds stress) using closure models the computational effort and memory requirements can be reduced. A RANS turbulence model is the standard $k-\epsilon$ turbulence (STD) model, which is comprised of a RANS model and two additional evolution equations for turbulence kinetic energy (TKE) represented by $k$ and the dissipation rate of TKE represented by $\epsilon$. The $k-\epsilon$ model assumes that turbulent flows to be isotropic. Considering flow through apipe at high Reynolds number is a reasonable assumption. The pipe flow in the low Reynolds turbulence region, on the other hand, is known to be an anisotropic [10], and thus assumption of isotropic turbulence distorts the results. Therefore, the equations of the model need to be adjusted by adopting an additional term and a damping function, and changing the boundary conditions. OpenFOAM v7 has several $k-\epsilon$ model-based low Reynolds number turbulence models such as, Launder–Sharma (LS) model [11], Lam–Bremhorst (LB) model [12], Lien–Leschziner (LL) model, [13], and Lien–Chen–Leschziner (LC) model [14]. The equations are given below Eqs. (2.3-2.6). The additional terms, the damping function, and the boundary conditions are tabulated in [Tables 2.1-2.2].

$$\frac{\partial \bar{U}_i}{\partial x_i} = 0 \tag{2.3}$$

$$\frac{\partial \bar{U}_i \bar{U}_j}{\partial x_i} = \frac{\partial \bar{p}}{\partial x_i} + \frac{\partial}{\partial x_i}\left[\nu\left(\frac{\partial \bar{U}_i}{\partial x_j} + \frac{\partial \bar{U}_j}{\partial x_i}\right) - \overline{u_i' u_j'}\right] \tag{2.4}$$

$$\frac{\partial \bar{U}_i k}{\partial x_i} = \frac{\partial}{\partial x_i}\left[\left(\nu + \frac{\nu_t}{\sigma_t}\right)\frac{\partial k}{\partial x_j}\right] + P_k - \tilde{\epsilon} \tag{2.5}$$

$$\frac{\partial \bar{U}_i \tilde{\epsilon}}{\partial x_i} = \frac{\partial}{\partial x_i}\left[\left(\nu + \frac{\nu_t}{\sigma_{\tilde{\epsilon}}}\right)\frac{\partial \tilde{\epsilon}}{\partial x_j}\right] + C_{\epsilon 1} f_1 \frac{\tilde{\epsilon}}{k} P_k + C_{\epsilon 2} f_2 \frac{\tilde{\epsilon}^2}{k} + E \tag{2.6}$$

where $\bar{U}_i$ is the average velocity; $\overline{u_i u_j}$ is the average Reynolds stress; $\nu$ and $\nu_t$ are the viscosity and turbulence viscosity, respectively; $k$ is the TKE; $\tilde{\epsilon}$ is the modified dissipation rate of TKE ($\tilde{\epsilon} = \epsilon - D_k$); $P_k$ is the production term; $f_\mu$, $f_1$, and $f_2$ are damping factors; $C_\mu$, $C_{\epsilon 1}$, $C_{\epsilon 2}$, $\sigma_k$, $\sigma_\epsilon$ are closure coefficients of 0.09, 1.44, 1.92, 1.0, and 1.3, respectively, for the $k - epsilon$ model [10].

An algebraic Reynolds stress model (ARSM) is a simplified version of the Reynolds stress model. Rodi [15] introduces an algebraic equation that is simplified from the differential equation in the RSTM by assuming that the change of the anisotropic tensor is zero (approximation for slowly-evolving flow), and that the diffusive transport of the Reynolds stress anisotropy is small. The LC model is a kind of ARSM model.

Table 2.1: Damping coefficients for turbulence models

| Model | $f_\nu$ | $f_1$ | $f_2$ |
|---|---|---|---|
| STD | 1 | 1 | 1 |
| LS | $\exp(-3.4/(1 + Re_\tau/50)^2)$ | 1 | $1 - 0.3\exp(-Re_\tau^2)$ |
| LL | $\frac{1-\exp(-0.016\, l_n^*)}{1-\exp(-0.263\, l_n^*)}$ | $1 + P_k'/P_k$ | $1 - 0.3\exp(-Re_\tau^2)$ |
| LB | $(1 - \exp(-0.0165\, l_n^*))$ | $1 + (0.05/f_\mu)^2$ | $1 - \exp(-Re_\tau^2)$ |

Here, $Re_\tau = k^2/\nu$, $\epsilon$ is the turbulence Reynolds number, $l_n^* = l_n k^{0.5}/\nu$ is the normalized distance from the wall, $P_k' = C_{\epsilon 2}\ k^{1.5}/[3.53\ l_n\{1 - \exp(-0.63\ l_n^*)\}]\exp(-0.00222\ l_n^*)$ is the modified production term as a function of $l_n^*$, and $l_n$ is distance from the wall.

Table 2.2: Terms and boundary conditions for turbulence models

| Model | $\nu_t$ | $P_k$ | D | E | Wall BC |
|---|---|---|---|---|---|
| STD | $C_\nu f_\nu \frac{k^2}{\epsilon}$ | $-\overline{u_i u_j}\frac{\bar{U}}{x_j}$ | 0 | 0 | $k = \epsilon = 0$ |
| LS | $C_\nu f_\nu \frac{k^2}{\epsilon}$ | $-\overline{u_i u_j}\frac{\bar{U}}{x_j}$ | $2\nu(\frac{\sqrt{k}}{y})^2$ | $2\nu\nu_t(\frac{^2\bar{U}}{y^2})^2$ | $k$=0, $\epsilon$=wall function |
| LL | $C_\nu f_\nu \frac{k^2}{\epsilon}$ | $-\overline{u_i u_j}\frac{\bar{U}}{x_j}$ | 0 | 0 | $k = \epsilon = 0$ |
| LB | $C_\nu f_\nu \frac{k^2}{\epsilon}$ | $-\overline{u_i u_j}\frac{\bar{U}}{x_j}$ | 0 | 0 | $\frac{dk}{dy}$=0, $\epsilon$=wall function |

### 2.1.2 Reynolds stress transport model

The RSTM employs the Reynolds stress evolution equation instead of the TKE evolution equation. It is referred to as a seven equations model because six components of the symmetric stress tensor evolution equation and the dissipation rate evolution equation are required to be solved. The Reynolds stress transport equation is comprised of transport of turbulent quantities by diffusion; production; dissipation and redistribution; and the equation is expressed as follows:

$$\frac{D}{Dt}\overline{u_i u_j} + \frac{\partial T_{kij}}{\partial x_k} = P_{ij} + R_{ij} - \epsilon_{ij} \tag{2.7}$$

The key feature of the RSTM is to establish a model for the pressure-rate-of-strain tensor. The redistribution term can be divided into three different parts: the slow term, which is related to inherent turbulence quantities; the raid term, which is related to mean strain rate; and the near-wall term, which is related to the wall-reflection effect. Launder–Reece–Rodi (LRR) model [16] was established with the first order model for the rapid redistribution term. Speziale–Sarkar–Gatski (SSG) model [17] was developed using an advanced quadratic pressure-rate-of-strain model. For the SSG model, the production tensor $P_{ij}$, Reynolds-stress flux $T_{kij}$, dissipation-rate tensor $\epsilon_{ij}$, and pressure-rate-of-strain redistribution tensor $R_{ij}$ are, respectivley, are represented in Eqs. 2.8 - 2.11.

The diffusion model developed by Daly and Harlow [18] is introduced for the Reynolds stress flux.

$$P_{ij} = -\overline{u_i u_j}\frac{\partial \overline{U}_j}{\partial x_k} - \overline{u_i u_j}\frac{\partial \overline{U}_i}{\partial x_k} \tag{2.8}$$

$$T_{kij} = -\nu\frac{\partial \overline{u_i u_j}}{\partial x_k} - C_s\frac{k}{\epsilon}\overline{u_i u_j}\frac{\partial \overline{u_i u_j}}{\partial x_l} \tag{2.9}$$

$$\epsilon_{ij} = \frac{2}{3}\epsilon\delta_{ij} \tag{2.10}$$

$$\begin{aligned} R_{ij} = & -(C_1\epsilon + C_1^* P_{kk})b_{ij} + C_2\epsilon(b_{ik}b_{kj} - \frac{1}{3}b_{kl}b_{kl}\delta_{ij}) + (C_3 - C_3^*\sqrt{b_{kl}b_{kl}})k\overline{S}_{ij}^* \\ & + C_4 k(b_{ik}\overline{S}_{jk} + b_{jk}\overline{S}_{ik} - \frac{2}{3}b_{mn}\overline{S}_{mn}\delta_{ij}) + C_5 k(b_{ik}\overline{\Omega}_{jk} + b_{jk}\overline{\Omega}_{ik}) \end{aligned} \tag{2.11}$$

where $\overline{U}_i$ is the averaged velocity, $\overline{u_i u_j}$ is the Reynolds stress, $\overline{p}$ is averaged pressure, $\epsilon$ is the dissipation rate, $\nu$ is the viscosity, $\nu_k = C_\mu k^2$ is turbulent viscosity, $k = \frac{1}{2}\overline{u_k u_k}$ is TKE, $b_{ij} = \overline{u_i u_j}/\overline{u_i u_j} - \frac{1}{3}\delta_{ij}$ is a normalized anisotropy tensor, $\overline{S}_{ij} = \frac{1}{2}(\frac{\partial \overline{U}_i}{\partial x_j} + \frac{\partial \overline{U}_j}{\partial x_i})$ is the averaged strain-rate tensor, $\overline{S}_{ij}^* - \frac{1}{3}\overline{S}_{kk}\delta_{ij}$ is the averaged traceless strain-rate tensor, and $\overline{\Omega} = \frac{1}{2}(\frac{\partial \overline{U}_i}{\partial x_j} - \frac{\partial \overline{U}_j}{\partial x_i})$ is the averaged rotation-rate tensor. The equation for the transport of the dissipation rate ($\epsilon$) is given below:

$$\frac{D}{Dt}(\epsilon) = C_{\epsilon 1}\frac{\epsilon^2}{k}P_{kk} - C_{\epsilon 2}\frac{\epsilon^2}{k} + \frac{\partial}{\partial x_j}\left[\left(\nu + C_{eps}\frac{k}{\epsilon}\right)\frac{\partial \epsilon}{\partial x_j}\right] \tag{2.12}$$

### 2.1.3 Large Eddy Simulation (LES)

The LES approach resolves large scale flow structures and models small scale flow structures as they are universal. For incompressible flows, the filtered Navier–Stokes Equation for LES is as follows:

$$\frac{\partial \tilde{\boldsymbol{U}}_i}{\partial t} + \frac{\partial}{\partial x_j}(\tilde{\boldsymbol{U}}_i\tilde{\boldsymbol{U}}_j) = -\frac{1}{\rho}\frac{\partial \tilde{p}}{\partial x_i} + \nu\frac{\partial^2 \tilde{\boldsymbol{U}}_i}{\partial x_j^2} + \frac{1}{\rho}\frac{\partial \boldsymbol{\tau}_{ij}}{\partial x_j} \tag{2.13}$$

$$\boldsymbol{\tau}_{ij} = -\tfrac{2}{3}k_{sgs}\delta_{ij} + 2\nu_{sgs}\tilde{\boldsymbol{S}}_{ij}^* \tag{2.14}$$

where $\tilde{\boldsymbol{U}}_i$ is filtered instantaneous velocity; $\tilde{p}$ is filtered pressure; $\boldsymbol{\tau}_{ij}$ is residual stress tensor; $\nu_{sgs}$ is subgrid-scale viscosity; $k_{sgs}$ is subgrid-scale TKE, which can be calculated by $\nu_{sgs} = C_k \Delta \sqrt{k_{sgs}}$; $C_k$ is a constant; $\Delta$ is the sub-grid characteristic length scale; $\tilde{\boldsymbol{S}}^*_{ij}$ is the deviatoric tensor of the filtered strain rate; and $\delta_{ij}$ is the Kronecker delta.

In this study an LES having the wall-adapting local eddy-viscosity (WALE) model proposed by Nicoud and Ducros [19] is adopted. In this model subgrid, the eddy-viscosity is proportional to the cube of the wall-normal component ($\nu_{sgs} \sim y^3$), and approaches zero near the wall; hence, neither constant adjustment nor damping function is required for wall-bounded flows. They revised the Smagorinsky eddy-viscosity model by employing velocity gradient tensor $\tilde{\boldsymbol{g}}_{ij} = \frac{\partial \tilde{\boldsymbol{U}}_i}{\partial x_j}$, yielding the following subgrid-scale viscosity model:

$$\nu_{sgs} = (C_w \Delta)^2 \frac{(\boldsymbol{S}^d_{ij} \boldsymbol{S}^d_{ij})^{1.5}}{(\tilde{\boldsymbol{S}}_{ij} \tilde{\boldsymbol{S}}_{ij})^{2.5} + (\boldsymbol{S}^d_{ij} \boldsymbol{S}^d_{ij})^{1.25}} \tag{2.15}$$

where $\nu_{sgs}$ is subgrid-scale viscosity; $C_w$ is a constant; $\Delta$ is the sub-grid characteristic length scale; $\boldsymbol{S}^d_{ij}$ is the traceless symmetric part of the square of the velocity gradient tensor, defined by Eq.2.16; and $\tilde{\boldsymbol{S}}_{ij}$ is filtered strain rate, defined by Eq.2.17.

$$\boldsymbol{S}^d_{ij} = \tfrac{1}{2}(\tilde{\boldsymbol{g}}^2_{ij} + \tilde{\boldsymbol{g}}^2_{ji}) - \tfrac{1}{3}\delta_{ij}\tilde{\boldsymbol{g}}^2_{kk} \tag{2.16}$$

$$\tilde{\boldsymbol{S}}_{ij} = \frac{1}{2}\left(\frac{\partial \tilde{\boldsymbol{U}}_i}{\partial x_j} + \frac{\partial \tilde{\boldsymbol{U}}_j}{\partial x_i}\right) \tag{2.17}$$

Partial differential equations for Reynolds stress, subgrid-scale viscosity, and dissipation rate are not required because the WALE model is an algebraic eddy viscosity model. This modified eddy-viscosity model allows simulating both laminar and turbulent regions of flows in a pipe. As the model produces zero eddy-viscosity in the case of pure shear, the laminar–turbulent transition process can be reproduced.

Li [20] conducted LES with the WALE model to reproduce the turbulent flows of twin parallel jets and observed good agreement with particle image velocimetry (PIV) measurements. Choi[21]

also compared the results of an LES model with the PIV measurements made in the Low Pressure Low Temperature (LPLT) Fission Product Venting System (FPVS) test facility at Texas A&M University and found a reasonable agreement. Therefore, The WALE LES model was selected to study turbulent flow in this study.

### 2.1.4 Friction Factor

The friction factor is used to calculate the energy loss due to the friction in a pipe flow. The shear stress exerted on the wall is proportional to the friction factor, and can be expressed as follows:

$$\tau = \frac{1}{8} f_D \rho U_b^2 \tag{2.18}$$

where $\tau$ is the shear stress at the wall, $\rho$ is the density of the fluid, and $U_b$ is the bulk velocity.

The friction velocity $u_\tau$ (also known as shear-stress velocity) is defined as the square root of shear stress divided by density. This quantity has the dimensions of velocity, and the important scaling velocity is used in the study of boundary layers for pipe flows. It is also used for the definition of shear Reynolds number $Re_\tau$.

$$(u_\tau)^2 = \tau/\rho \tag{2.19}$$

$$Re_\tau = (d/2)u_\tau/\nu \tag{2.20}$$

where $d$ is the diameter of the pipe; $u_\tau$ is friction velocity; $\nu$ is kinematic viscosity; $y^+$ is the non-dimensional length representing thickness of the viscous layer, which is defined by $yu_\tau/\nu$; $y$ is the length from the wall; The value of the shear Reynolds number is equal to the length of the hydraulic radius of the channel in the unit of $y^+$.

The Colebrook–White equation represents the relationship of the Darcy friction factor $f_D$ to the Reynolds number, pipe roughness, and the diameter of pipe. The following equation can be

used to calculate the friction factor in gas pipelines in turbulent flows:

$$\frac{1}{\sqrt{f_D}} = -2\log_{10}\left(\frac{\epsilon_r}{3.7D} + \frac{2.51}{Re\sqrt{f_D}}\right) \tag{2.21}$$

where $f_D$ is the Darcy friction factor, $D$ is the diameter of the pipe, $\epsilon_r$ is absolute pipe roughness, and $Re$ is the Reynolds number.

The Darcy friction factor can also be estimated by the Darcy–Weisbach equation, and is a function of the pressure drop per unit length $\Delta p/L$ in the pipe. Because the constant pressure gradient of pipe flow is easy to extract and pipe roughness is an ambiguous concept in numerical simulation, this is the common method for the numerical simulation of pipe flow. Note that pressure calculated from the OpenFOAM for incompressible flow is actually kinematic pressure (pressure over density).

$$f_D = \frac{2D_h}{U_b^2}\frac{\Delta p/\rho}{L} \tag{2.22}$$

where, $\rho$ is the density of the fluid, $D_h$ is the hydraulic diameter of the pipe ($= 4A/P$ for a pipe of cross-sectional area $A$ and perimeter $P$), and $U_b$ is the bulk velocity.

### 2.1.5 Secondary Flows

The existence of a secondary flow in a non-circular duct was first reported by Prandtl [22], who classified it as Prandtl flow of the second kind. A pair of counter-rotating secondary vortices was formed at each corner, which yield a total of eight vortices in a square duct in the turbulent flow regime. The direct numerical simulation (DNS) of turbulent flows in square ducts makes it possible to resolve this phenomenon. Secondary vortices arise from the anisotropy and inhomogeneity of the Reynolds stress of a non-circular channel flow. Gavrilakis [2] was the first to perform a DNS study of square duct flow with a low Reynolds number of $Re_\tau = hu_\tau/\nu = 150$, showing secondary vortices.

Table 2.3: Boundary Conditions

| Variable | Inlet | Outlet | Side (Wall) |
|---|---|---|---|
| U | 2D profiles measured from exp. | Zero gradient | No slip |
| p | Zero gradient | Fixed value: 0 | Zero gradient |
| k or $R_{ij}$ | 2D profiles estimated from exp. | Zero gradient | Given as Table 2.2 |
| $\epsilon$ | 2D profiles estimated from exp. | Zero gradient | Given as Table 2.2 |

## 2.2 Numerical setup

To study the particle transport in a square channel, the simulation domain was based on the geometrical dimensions of the proof-of-concept test facility as seen on Figure 2.1. The proof-of-concept test facility had three test sections, each with a 3-inch-square cross-section and a length of 24 in. Similarly, the simulation domain has an $8\pi h$-long duct with the same cross-sectional shape, where $h$ is half the height of a channel. Details of the experimental design and preliminary measurements can be found in reference [1]. The simulation grid was generated by *blockMesh*, which is a built-in program in OpenFOAM v7. The grid spacing along the stream-wise direction (x-axis) was constant, except near the entrance, while the cross-stream (y- axis) and span-wise directions (z-axis) had uniform grids, fulfilling the grid size independence test. The boundary condition is specified in Table 2.3. The upstream flow characteristics for a square duct were obtained using PIV measurements. The values in Chavez et al. [1] were used as boundary conditions at the inlet of the computational domain for the simulation.

To begin the simulation, the grid independence was established. A grid convergence index (GCI) test was conducted for the center-line velocity. The results showed that the centerline velocity converged to an asymptotic value as the grid became finer. Considering the computational power and measurement error, a $101 \times 101$ uniform mesh in the cross-section and 101 mesh along streamwise was determined to be acceptable because the center-line velocity has a deviation of less than $2\%$ from the asymptotic value.

To achieve a fully developed flow conditions a very long channel is required. It is known that

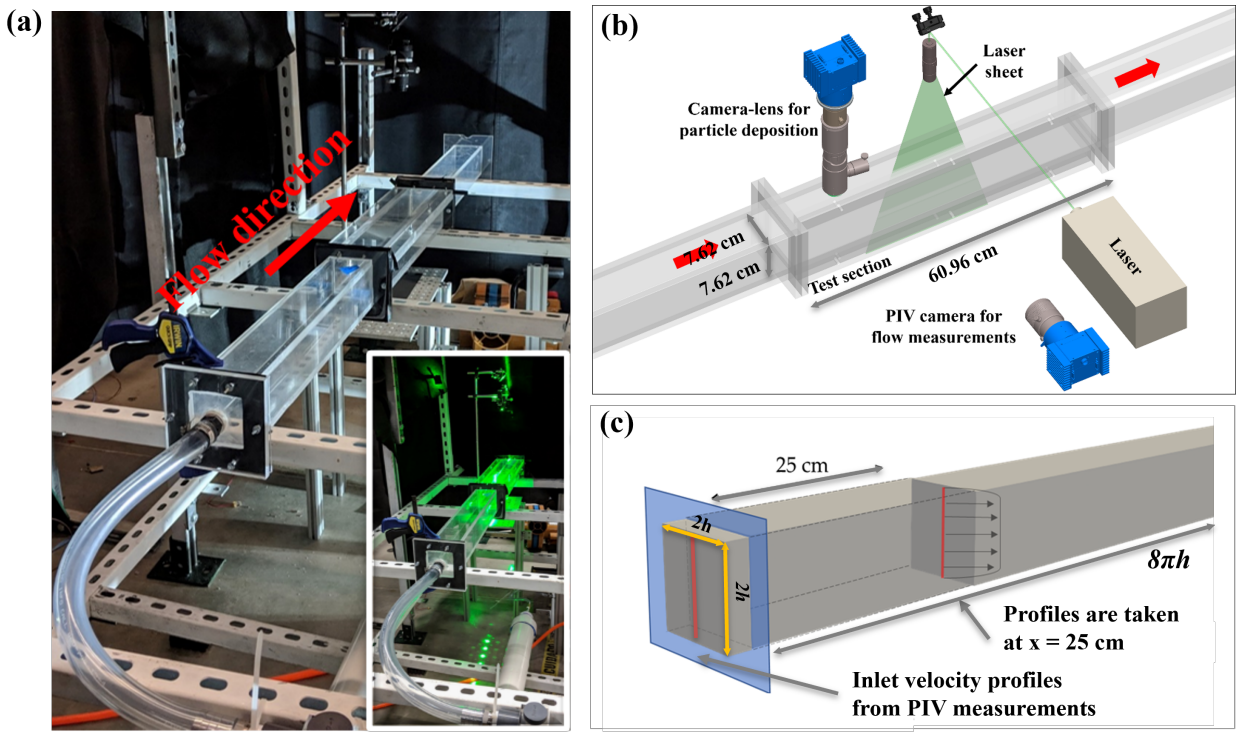


Figure 2.1: (a) The proof-of-concept test facility, (b) schematic diagram for the PIV measurements in the test facility, and (c) the domain employed for numerical simulation of developing flow

a length of approximately $30d$ is required for flow to be fully developed, while that of $100d$ is required for laminar flow, resulting in a high computational cost. There is alternative method to reduce the computational power. By using a cyclic boundary condition instead, the size of the domain can be reduced. The cyclic boundary condition assumes that the inlet conditions are the same as the outlet conditions. To properly generate turbulence flow in a channel, two steps are required. First, turbulence is artificially initiated before running the simulation. One of the easiest ways to initiate the turbulence spontaneously is to utilize a backward-facing step flow. Turbulence is induced downstream of the step, and thus velocity information downstream of the step can be employed as an initial condition of the flow domain. In OpenFOAM, velocity information obtained from geometry of the backward-facing step can be copied to a new domain with cyclic boundary conditions using *mapFields*. Figure 2.2 represents the procedure for initiating the turbulence before running cyclic boundary conditions in openFOAM. Second, turbulence loss by dissipation should

be compensated for. Otherwise, flow loses its turbulence, turning into a laminar-like flow. In openFOAM, an artificial force term can be applied using the *fieldsAverage* option in *fvOption* to maintain a constant bulk velocity.

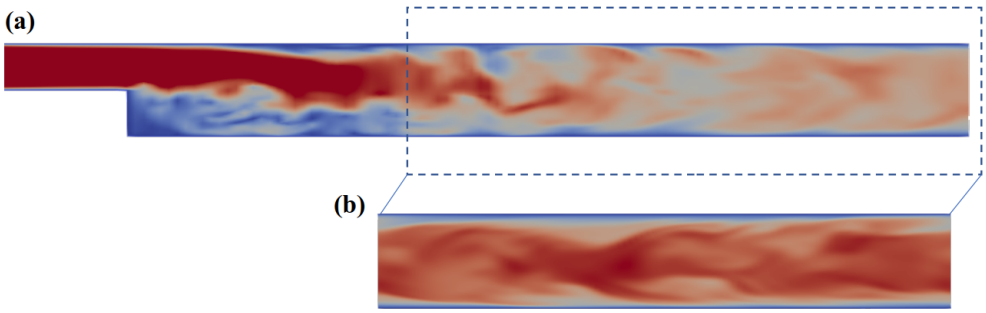


Figure 2.2: Stream-wise Instantaneous Velocity Contours for (a) backward-facing step, and (b) cyclic boundary condition

## 2.3 Results and Discussion

### 2.3.1 Developing Flows in a Square Duct

Some turbulence models such as the standard $k-\epsilon$ model [23] are known to have been designed only for stationary, fully developed flow simulation. Turbulence model candidates should be validated for a developing flow by comparing them with experimental data. Figure 2.3 shows the stream-wise velocity profile at $z = h$ (where $h$ is half of the channel height) with respect to the lateral direction. Markers $\times$ and $\circ$ represent the velocity profiles measured by Chavez [1] for the case of $Re_c$=5,833 for upstream and mid-stream locations. Those lines are 25 cm apart at the mid-section, which illustrated as the red lines in Figure 2.1-(c). The solid line in the Figure 2.3 represents the velocity profile at the midstream location (25 cm from the entrance) estimated by a numerical simulation, in which the velocity marked with an $\times$ is employed as the inlet condition. The velocity profiles estimated using the LS model [11] and LL model [13] compared well with the experimental data at the center of the channel, whereas that obtained from the SSG model [17]

performed better in the proximity of the wall. Similarly, Figure 2.3 shows TKE profiles measured using the PIV as a reference and predictions from numerical simulations with various turbulence models. In Figure 2.3, the TKE values computed using various turbulence models are compared to the measured data of [1]. In the mid-stream region (25 cm from the entrance of the mid-section), the calculated results are underestimated compared with the experimental data. Again, the $\times$ curve shows the experimentally- measured TKE at the entrance of the mid-section. Turbulence model candidates are expected to reproduce the secondary vortices in a numerical simulation. Among the six different models considered in this study, only the SSG model of [17] was clearly able to capture the secondary vortices at each corner of the channel. Each corner had a pair of vortices, thus there were eight vortices in a given channel cross-section.

### 2.3.2 Fully Developed Flow in a Square Duct

The model prediction of the mean axial velocity was obtained for the bulk Reynolds number ($Re_b$) of 4,400 and is compared with the reference DNS data of [2] in a fully developed flow region with an $Re_\tau$ value of 150, which is equivalent to a $Re_b$ value of 4,410 and a $Re_c$ value of 5,883 in Figure 2.4. Figure 2.4 shows the streamwise velocity normalized to the center-line streamwise velocity calculated using different models at the middle of the cross-section for fully developed flows. The stream-wise velocities of the STD [23] and SSG model [17] compared well with the DNS simulation data [2] near the center, whereas there are some deviations on the velocity gradient near the wall. On the other hand, the damping function used in other models, such as the LS model [11], LB model [12], and LL model [13], fits well near the wall but distorts the shapes of the velocity profiles near the axis. The ratios of the center-line velocity to the bulk velocity listed in Table 2.4 indicate that the STD model [23] deviates the most ($+5.72\%$) compared with the DNS data [2] at $Re_\tau$ = 150. From Table 2.4, the LL model [13] compares the best with the DNS data [2], with a deviation of $-0.37\%$. Figure 2.4 shows profiles of the TKE obtained using various turbulence models $k$ at $y = h$ for a fully developed flow ($Re_\tau = 150$). In the middle of the channel, the TKE obtained from the LS model [11] or LL model [13] compares well with the DNS data [2], while the SSG model [17] performs better in the near-wall region. Because the turbulence

effects near the wall impact the particle deposition, in this study the SSG model [17] was used to simulate the flow field in Chapter 5.

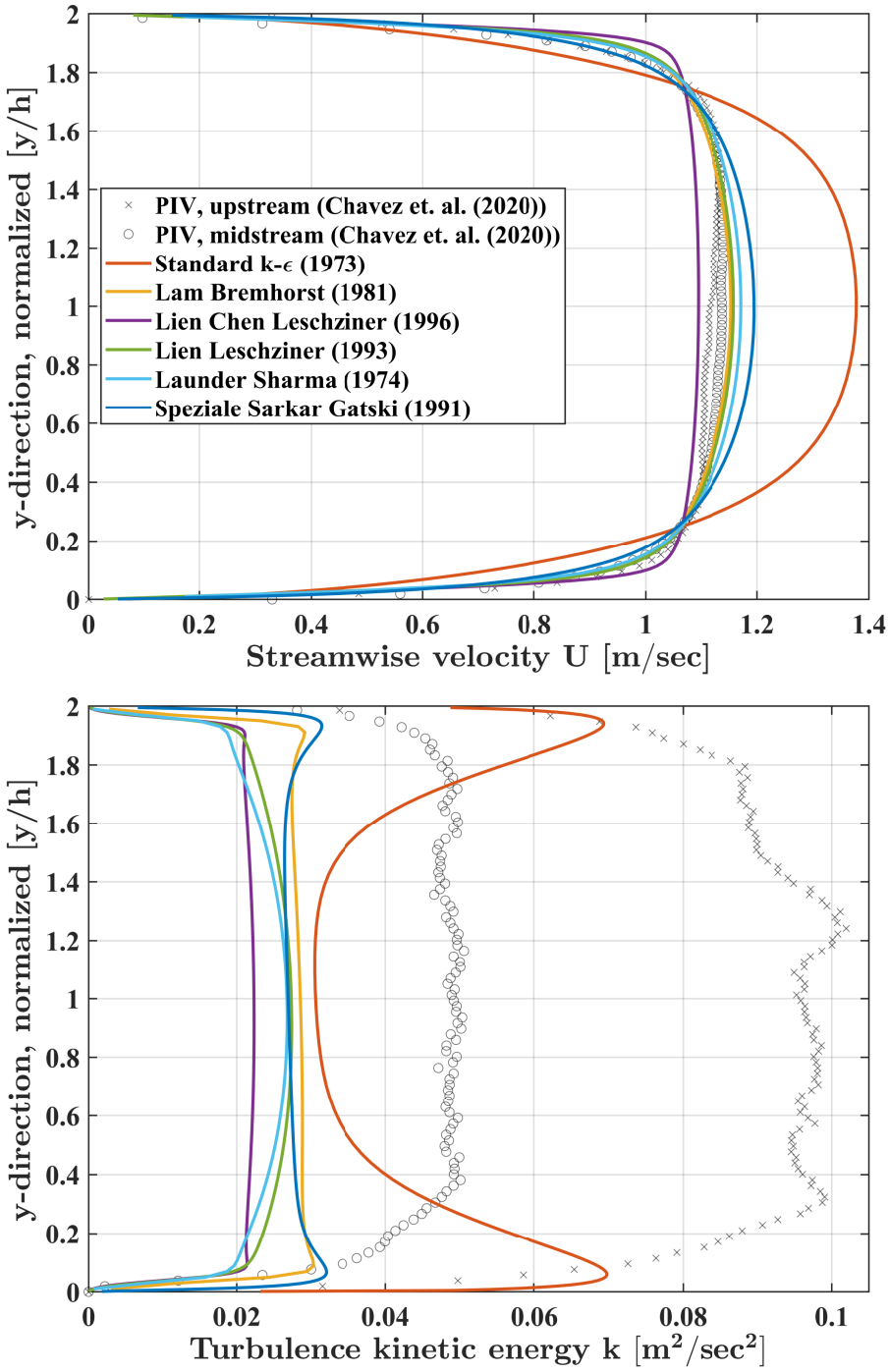


Figure 2.3: Flow profile from the wall to center for developing flow at $Re_c$=5,883 (a) Streamwise velocity, and (b) turbulence kinetic energy

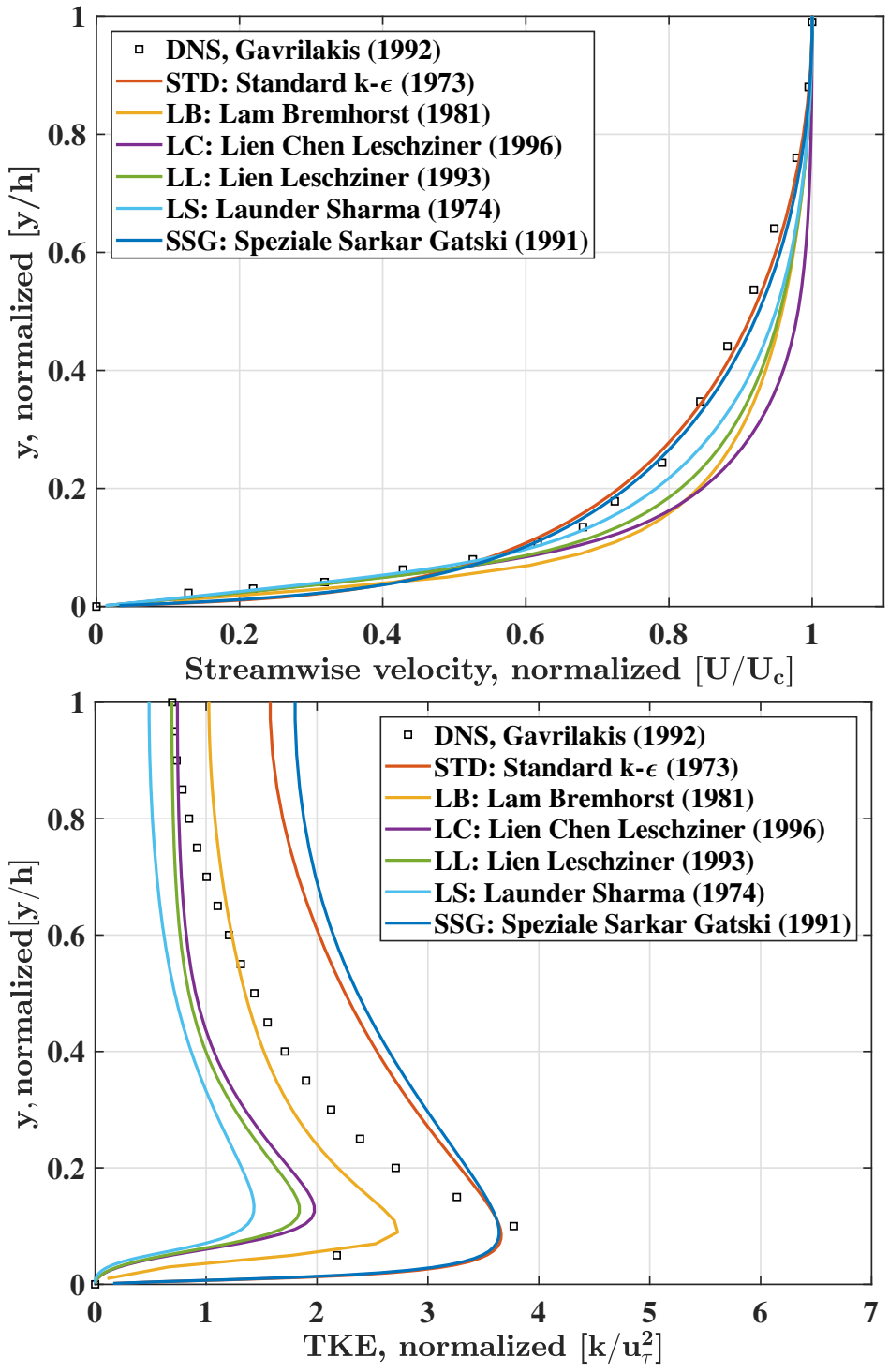


Figure 2.4: Fully Developed Flow Profiles (a) Streamwise velocity, and (b) Turbulence Kinetic Energy

Table 2.4: Ratio of the centerline Velocity to Bulk Velocity

| Model | DNS | STD | LB | LC | LL | LS | SSG |
|---|---|---|---|---|---|---|---|
| $U_c/U_b$ | 1.33 | 1.406 | 1.281 | 1.280 | 1.325 | 1.361 | 1.359 |
| Deviation from the DNS[2] | - | +5.72% | -3.71% | -3.74% | -0.37% | +2.32% | +2.16% |

A LES-WALE model study was also conducted for flow with $Re_b$ = 4,000, and compared with reference DNS data [2] of $Re_b$ = 4,410, as shown in Figure 2.5. Square markers represent stream-wise velocity and Reynolds stress profiles on the line bisecting the cross-section vertically, whereas the solid line denotes the for DNS results of [2]. A viscous sublayer and log-law regions are clearly seen in the LES predictions, and has good agreement with the DNS results in Figure 2.5-(a). In the viscous sublayer, the velocity parallel to the wall normalized by the friction velocity is equal to th $y^+$ value. In the log-law region, the normalized velocity is proportional to log($y^+$). Gavrilakis suggested $U^+ = 3.2\ln(y^+) + 3.9$ for flow through a square duct with $Re_b$ of 4,410 [2]. Figure 2.5-(b) shows the root-mean-square of fluctuation velocity; the profiles near the wall have good agreement with the DNS results of [2]. Figure 2.6 illustrates the cross-sectional contours of the channel for averaged streamwise velocity, instantaneous velocity, secondary velocity, and TKE. It is evident that amongst all considered models in this study the LES-WALE model performs the best. Hence, the LES-WALE model was selected as the turbulence model for numerical simulations reported in Chapters 3 and 4.

Another important criteria for selecting the turbulence model is its ability to capture secondary flows at corners of non-circular channels. Figure 2.6-(c) shows secondary velocity fields as arrows and the magnitude as contours obtained from result of LES-WALE model. A pair of vortices are located at each corner. The magnitude of the secondary flow is approximately $1 - 2\%$ of that of the stream-wise flow located at a diagonal line near the corner, which is in good agreement with the DNS data of [2, 6, 7]. The secondary flow cannot be ignored in a long non-circular duct. Zhang's particle simulation [24] shows that secondary flow can affect particle behavior. According to the theoretical derivation by Speziale [25], the $k - \epsilon$ model does not have a mechanism to

model secondary flows. Similarly, only the RSTM-SSG model and LES-WALE model were able to capture the secondary flow in our simulation.

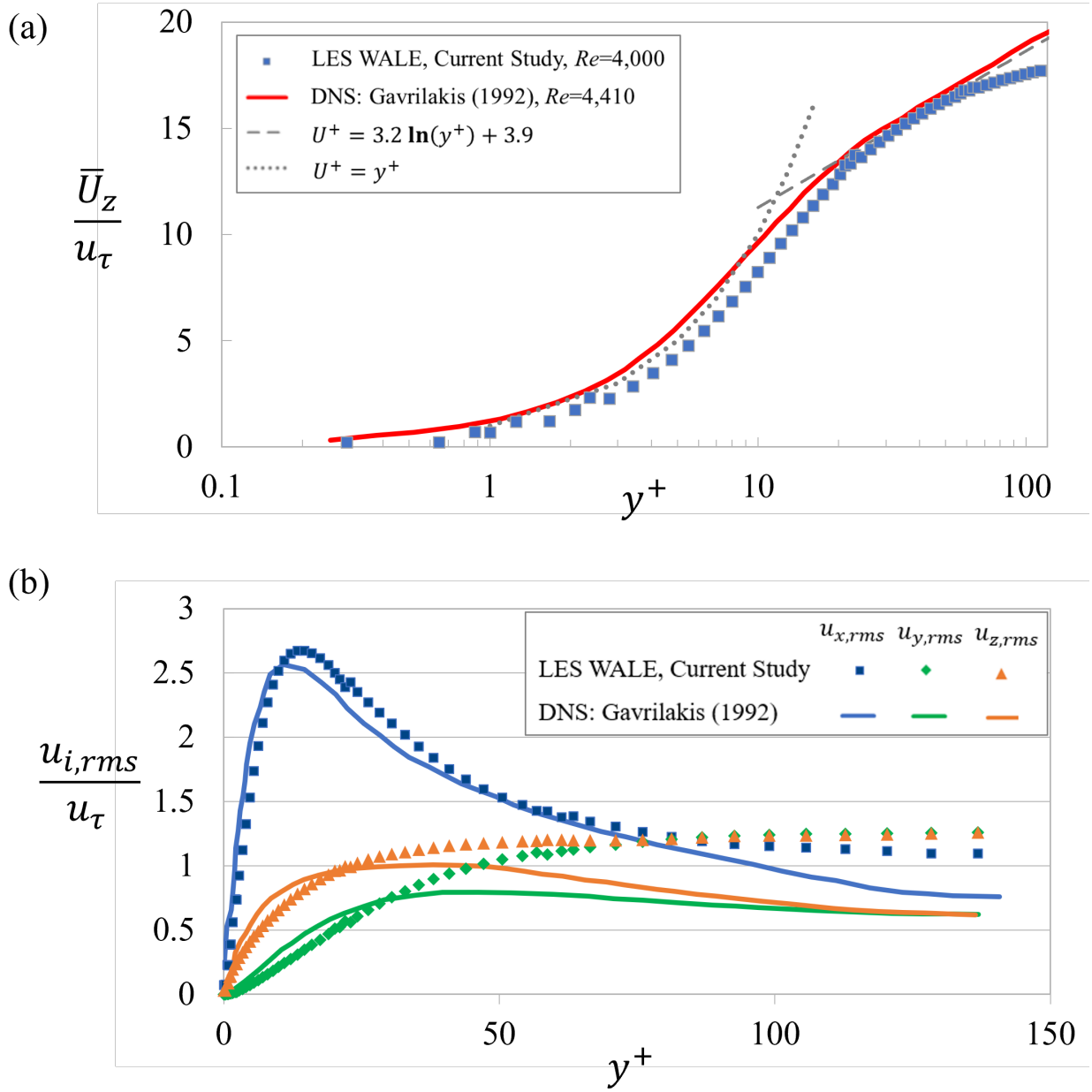


Figure 2.5: (a) Stream-wise velocity and (b) $u_{rms}$ as a function of $y^+$ in square duct flow obtained by LES study

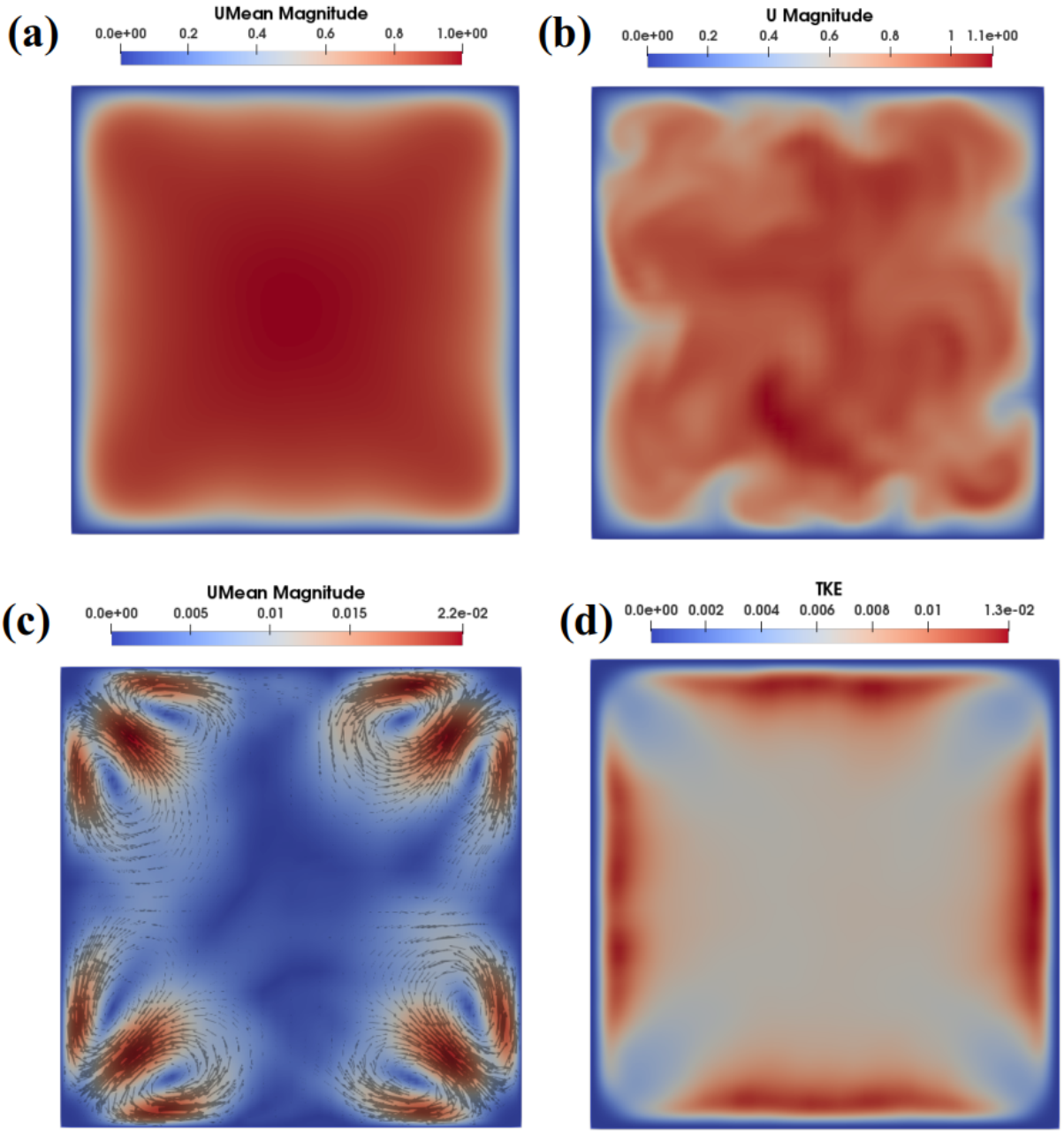


Figure 2.6: Cross-sectional contours of (a) temporal-averaged velocity, (b) instantaneous velocity, (c) secondary velocity, and (d) turbulence kinetic energy

## 2.4 Conclusion

Seven different turbulence models were tested for low Reynolds number turbulent flow through a square duct. The results for developing flow were compared with the PIV measurements [1], and those of developed flow were compared with the DNS results [2]. The Streamwise velocity, TKE (or Reynolds stress), ratio between maximum velocity $U_c$ and bulk velocity ($U_b$), and the secondary flow calculated using seven different turbulence models were compared with the DNS results [2].

In developing flow comparisons, the STD model [23] results demonstrated significant differences for streamwise velocity compared to the PIV measurements ([1]), proving that the STD model is not adequate for pipe flow simulations. On the other hand, the other low-Reynolds $k-\epsilon$ model and SSG model displayed acceptable velocity profiles. Compared with the PIV measurements ([1]), all models under predicted TKE. This may be because coefficients of the closure models considered in this study were obtained from the fully developed flow cases.

For developed flows, $k-\epsilon$ models with damping coefficients (LS model [11], LB model[12], LL[13], and LC model[14]) were able to reproduce the velocity profile near the wall, and TKE near the axis of the pipe, whereas the RSTM-SSG model [17] performed well for the velocity profile near the axis and the TKE near the wall. Because the Reynolds stress near the wall plays an important role on mixing for both multicomponent gaseous and solid particle simulations, the SSG model is preferred. In addition, the SSG model can capture the secondary flows at corners of non-circular ducts. Therefore, it is concluded that the SSG model is the best turbulence model for low-Reynolds number turbulent flow among the RANS family of models considered in this study.

If one has access to greater computational power, the LES-WALE model [19] is a better option. Both stream-wise velocity and Reynolds stress obtained from the LES-WALE model have good agreement with the DNS results [2] near the wall. The viscous sublayer region and logarithmic law region as well as secondary recirculating flows were clearly captured in Figures 2.5 and 2.6-(c). As an additional benefit, the LES-WALE model can be used to simulate the cases wherein both laminar and turbulent flows coexist, and it captures flow structure in the transition region. Therefore, in this study, the LES-WALE turbulence model is employed to simulate flow through an axisymmetric

sudden expansion in Chapter 3, and the fission product venting system (FPVS) in chapter 4. To optimize the computational cost, the SSG model is selected for the particle simulations in Chapter 5.

# 3. FLOW THROUGH AN AXISYMMETRIC SUDDEN EXPANSION*

The contents of this chapter were published by the author in the *Physics of Fluids* [26]. The Large Eddy Simulation (LEs) stduy is performed for flow through an axisymmetric flow to investigate effect of inlet condition such as turbulence intensity (TI) and Reynolds number ($Re$) at the inlet. Correlation for both critical points and reattachment length are proposed.

## 3.1 Introduction

Fluid flow through an axisymmetric sudden expansion flow system is complex and rich in flow physics. The flow recirculation occurs at the corner of the expansion and spatial and temporal fluctuations (or localized turbulence) may be observed based on upstream flow. This phenomenon must be understood from an engineering point of view because this phenomena relates to (a) flow mixing downstream of the expansion joint, (b) energy required to transport the fluid through the piping system, and (c) the impact of flow-induced vibration on the structural integrity of piping systems.

There are several experimental measurements of velocity profiles and reattachment lengths of flow through an axisymmetric expansion in the literature. Chaturvedi [27] determined the reattachment length ($Lr$) and turbulent characteristics at very high Reynolds numbers ($Re = U_b d/\nu = 200,000$) by using hot-wire anemometry to measure velocity profiles at different axial locations. Here, $U_b$ is the bulk velocity at the entrance of the upstream pipe, $d$ is the diameter of the upstream pipe, and $\nu$ is kinematic viscosity of the fluid. Yang [28], Khezzar [29], So [30, 31], and Durrett [32] used a laser Doppler anemometer (LDA) to measure the velocity profile in a circular pipe; Lukacs and Vad [33] measured velocity profiles in a square duct. Experiments with LDA are usually performed at High Reynolds number ($Re > 10,000$), resulting in a normalized reattachment length ($Lr/h$) between $5 \sim 10$, regardless of the expansion ratio (ER) or Reynolds number[30]. Iribarne [34] used a fluorescent dye to measure the velocity profile with UV light and a high-

*This chapter is reprinted/adapted with permission from [26]

speed camera. Back and Roschke [35], Latornell [5], and Pak [4] injected dye downstream of an axisymmetric expansion joint at various stream-wise locations to study reattachment.

Several efforts have been made to measure the critical value of $Re$ that separates laminar and transition regimes. However, there is no consensus on the value of the critical Reynolds number, which is denoted as $Re_c$. Sreenivasan et al. [36] studied the flow through an asymmetric expansion using a hot wire anemometer; They observed fluctuations and oscillations in the flow downstream of the expansion. Mullin [37] measured the velocity profile using magnetic resonance imaging (MRI) and found the critical Reynolds number ($Re_c$) to be 1,139. Above the critical Reynolds number, the asymmetry of velocity profiles increased with Reynolds number whereas a constant low asymmetry was observed below the critical Reynolds number. Further, Gach [38] measured the reattachment length by using MRI. The transition region is characterized by a decrease in the reattachment length with an increase in $Re$ ($Re^{-1.1}$). Furuichi [39] measured the axial velocity using an ultrasound technique; the velocity profiles suggested that the critical Reynolds number was 1,500. The ambiguity in the value of the critical Reynolds number was attributed to the complexity of the expansion flow in the transition region. Selvam [40] conducted numerical simulations for gradual expansion. Localized turbulence was triggered for $Re$ = 1,680 or higher with this level of disturbance mentioned above. Sanmiguel-Rojas [41] calculated the critical Reynolds number ($Re_c$) using the global mode analysis for a sudden expansion flow with an ER of 2. The flow became linearly unstable at a critical Reynolds number of 3,273 or higher; it corresponds to an oscillatory bifurcation with wave number $|m| = 1$ located at the end of the recirculation region which implies that that localized turbulence was generated regardless of the inlet condition.

The characteristics of sudden expansion flow is usually quantified by the reattachment length ($Lr$). The results from both dye injection experiments of Latornell [5] and Pak [4] represent that there are three possible flow regions downstream of the sudden expansion as a function of Reynolds number: laminar, transition, and turbulent. In the laminar region, the reattachment length is directly proportional to the flow Reynolds number ($Re$). For a pipe flow with an ER of 2 investigated in this work, the correlation is found as $Lr/h = 0.0885\,Re$ where $h$ is the step height. Futher, a

similar result is also found in Fletcher's numerical simulation[42] for the laminar flow, and it is expressed as $Lr/h = 0.0898\,Re$. The slope of this correlation is dependent on the ER, and a larger ER provides a smaller slope. In these cases, the upstream Reynolds number is defined as $U_b d/\nu$, where $U_b$ is the bulk velocity at the inlet, $d$ is the diameter of the upstream pipe, and $\nu$ is the kinematic viscosity of the fluid.

As Reynolds number increases and exceeds a certain threshold value, the relationship between reattachment length and Reynolds number reverses; the reattachment length decreases with an increase in the Reynolds number. The stratified flow becomes unstable and collapses at a shorter distance downstream in laminar flows due to localized turbulence. One explanation for this is that the Kelvin–Helmholtz instability is initiated between the mainstream and recirculation flow due to the velocity difference as Reynolds number is increased. As Reynolds number increases further, the reattachment length becomes less dependent on Reynolds number and can eventually be considered independent of Reynolds number, converging to an asymptotic value. Moallemi et al. [43] estimated the reattachment length for the sudden expansion flow as a function of Reynolds number using the Direct Numerical Simulation (DNS) technique; however, their results overestimated the reattachment lengths in the transition region compared with the experimental data reported in the literature [5, 4].

In addition to Reynolds number, the reattachment length is also affected by the shape of the inlet flow profile and the turbulent intensity at the flow inlet. It is difficult to study the effect of flow disturbance because it is hard to maintain the exact desired amount of the disturbance and unexpected disturbances from external sources (i.e. pumping systems) can impact the flow. So [30] reported that there is a clear trend on the reattachment length as a function of parameter $u_{rms}/\bar{U}_m$. For 2.5% < $u_{rms}/\bar{U}_m$ < 17.5%, the reattachment length decreases as $u_{rms}/\bar{U}_m$ increased [27, 32, 30, 31, 28]. Here, $u_{rms}$ is the root mean square of fluctuation velocity, and $\bar{U}_m$ is averaged bulk velocity.

Latornell [5] conducted a dye injection experiment for flow in a circular pipe and concluded that the reattachment length depends on the shape of the inlet profile. The reattachment length with

a plug profile at the inlet (high turbulence kinetic energy (TKE)) is shorter than that for the case of a fully developed inlet velocity profile. Pak [4] mentioned that the reattachment length is sensitive to artificially induced disturbances, such as small vibrations in the inlet feed line or from the test bench during the experiment. The reattachment length longer than $30h$ broke down quickly when a small external disturbance was applied.

Numerical simulation studies [21] showed that the shape of the velocity profiles is very different in absence of any artificial disturbance when compared to the experimental results reported in the literature [37, 39, 5, 4]. Without artificial disturbances, the reattachment length trend may follow the trend of the laminar flow at higher Reynolds numbers ($Re$ =2,000). There are several numerical[44, 40, 45, 46, 47, 48] and experimental[49] studies about the amplitude threshold of flow disturbance (or critical value). Sanmiguel-Rojas [44] and Selvam [40] showed a small flow perturbation perpendicular to the main flow impacts both the magnitude and location of the onset of the instability in their DNS study. The method used to generate an artificial disturbance at inlet is one of the independent parameters for this study. A small constant distortion of amplitude $\delta$ was applied to the fully-developed laminar flow $U_r = 2(1 - 4r^2)$, giving an inlet velocity $\boldsymbol{U}_{in}$ of

$$\boldsymbol{U}_{in} = 2(1 - 4r^2)\mathbf{e}_z + \delta\mathbf{e}_y \tag{3.1}$$

where $r$ is the radial coordinate, $\mathbf{e}_z$ is the axial coordinate vector, and $\mathbf{e}_y$ is the traverse coordinate vector.

Selvam [40], Lebon [45], Nguyuen [46], and Shenoy [47], on the other hand, applied a simple localized perturbation at the inlet in the form of a vortex. Nguyen [46] introduced a vortex perturbation in a DNS model of a sudden expansion flow and showed that the critical amplitude for vortex perturbation is proportional to $Re^{-3}$. Shenoy [47] studied flow through a gradual expansion and the critical amplitude was found to be proportional from $Re^{-2.1}$ to $Re^{-4.6}$ for a gradual angle $\theta$ from 45° to 4.76°, respectively, and the resulting equation for the inlet velocity is,

$$\boldsymbol{U}_{in} = U(r)\mathbf{e}_z - y\delta\Omega\mathbf{e}_x + x\delta\Omega\mathbf{e}_y \tag{3.2}$$

$$\Omega = \begin{cases} 1 & s \leqslant \mathcal{R}/2 \\ 2(\mathcal{R} - s)\mathcal{R} & \mathcal{R}/2 < s \leqslant \mathcal{R} \\ 0 & s > \mathcal{R} \end{cases} \tag{3.3}$$

where $U(r)$ is base axial velocity profile at the inlet, $\delta$ and $\Omega$ are the amplitude and the intensity of the vortex perturbation, $\mathcal{R}$ is the radius of the vortex, and $s = \sqrt{(x - x_0)^2 + (y - y_0)^2}$ is the distance between the center of the vortex $(x_0, y_0)$ to any point $(x, y)$ in the cross-section.

However, the methods mentioned above have limited applicability because in reality it is not practical to reproduce and control the flow disturbance. Introduction of flow disturbance with a random variable can be an alternative. The strength of this method is that the amount of disturbance can be correlated with turbulence intensity ($u_{rms}/\bar{U}_m$), which is a widely employed turbulence property, enabling direct comparison with the experimental data in the literature. Current and previous [21] studies employed this inlet boundary condition (Eq. 3.5), considering both randomized disturbance and the velocity of the previous time step. Luciano [48] employed similar concept that only considered a random disturbance, written as Eq. 3.4.

$$\boldsymbol{U}_{in} = \boldsymbol{U}_{ref} + \delta|\boldsymbol{U}_{ref}|(2\mathbb{R}) \tag{3.4}$$

where, $\boldsymbol{U}_{ref}$ is the reference velocity (fully-developed laminar flow), $\mathbb{R}$ is the random function ranged between $-0.5$ to $0.5$

Various studies on flow through an axisymmetric expansion mentioned above are summarized in Table 3.1.

The present study builds upon the results reported in the literature. The unique features of this work are: (a) turbulence intensity was used to characterize the flow disturbance at the inlet; (b) Large Eddy Simulation (LES) with the WALE model [19] was used to study the flow characteristics through an axisymmteric sudden expansion; (c) the numerical results generated as part this study matches with experimentally measured values of reattachment lengths in laminar, transition, and turbulent flow regimes at physically reasonable turbulence intensity values; (d) new classification of the flow characteristics for flow through a sudden expansion is suggested and a correlation

expression for the critical Reynolds number is developed; (e) using the generated numerical data a correlation was developed for reattachment length ($Lr$) as a function of Reynolds number ($Re$) and turbulence intensity (TI) at the inlet for the ER value of $2.0$; and (f) Proper Orthogonal Decomposition (POD) analysis was performed to gain deeper understanding of characteristics of flow through an axisymmteric expansion.

## 3.2 Numerical Procedure

### 3.2.1 Geometry, Inlet Conditions, and Mesh

Figure 3.1 illustrates the the geometry of the axisymmetric sudden expansion used in current study, comprised of two different sizes of concentric pipe with inner diameters of 25 mm for upstream ($d$) and 50 mm for downstream ($D$), yielding ER = 2. The upstream length from the sudden expansion is set to $5d$ to minimize attenuation of turbulent energy for laminar flows while the length of downstream pipe is set to $40d$ or more to minimize the exit effects on the reattachment length.

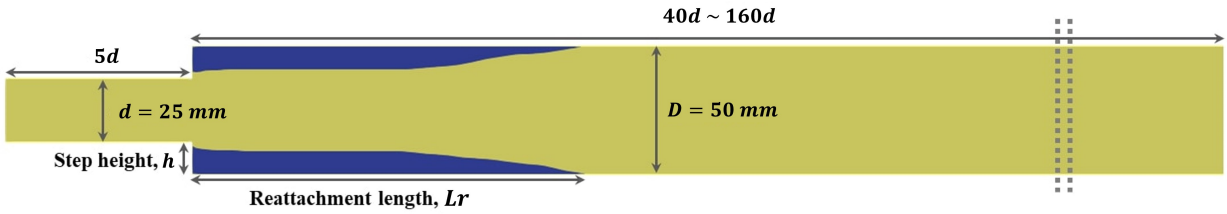


Figure 3.1: An axisymmetric sudden expansion flow geometry. Blue-colored area is the region where axial velocity is negative. Reprinted with permission from [26]

A fully-developed parabolic velocity profile for laminar flow, is specified as a base boundary condition at the inlet. To introduce the turbulent disturbance on the flow, a randomly generated fluctuation velocity based on turbulence intensity (TI) is appended to the boundary condition at the inlet. Turbulence intensity is defined as the ratio of the fluctuation velocity to the mean velocity ($u_{rms}/\bar{U}_m$). The in-house coded boundary condition based on *turbulentInlet* of the OpenFOAM v7

Table 3.1: A Summary of papers on flow through an axisymmetric sudden expansion in transitional region, reprinted with permission from [26]

| Name | ER | Method | Measured properties | $Re_C$ ($Lr_C$) | Correlation |
|---|---|---|---|---|---|
| Iribarne et al. (1972) [34] | 2.0 | Dye | Reattachment Length | 296 (27.0) | $Lr \sim Re^{-0.77}$ |
| Latornell and Pollard (1986) [5], FD | 2.0 | Dye | Reattachment Length | 915 (86.5) | $Lr \sim Re^{-2.012}$ |
| Latornell and Pollard (1986) [5], NZ | 2.0 | Dye | Reattachment Length | 617 (40.8) | $Lr \sim Re^{-1.993}$ |
| Sreenivasan and Strykowski (1983) [36] | 2.0 | Hot Wire | Flow Characteristics | 1,500∼1,700 | |
| Fletcher et al. (1985) [42] | 2.0 | NS | Reattachment Length | - | $Lr/h = 0.0898Re$ (laminar) |
| Pak et al. (1990) [4] | 2.0 | Dye | Reattachment Length | 688 (50.0) | $Lr \cong 1.321 \times 10^{10}\, Re^{-3.003} + 10.43$ |
| Gach and Lowe (2000) [38] | 2.0 | MRI | Reattachment Length | 526 (24.0) | $Lr \sim Re^{-1.07}$ |
| Furuichi et al. (2003) [39] | 1.8 | UVP | POD study | 1,500 | - |
| Mullin et al. (2009) [37] | 2.0 | MRI | Asymmetry | 1,139 | - |
| Sanmiguel-Rojas et al. (2010) [41] | 2.0 | - | Global Mode Analysis | 3,273 | - |
| Sanmiguel-Rojas and Mullin (2012) [44] | 2.0 | DNS | Amplitude Threshold Curves | 1,500 | $\delta \sim Re^{-0.006}$ |
| Selvam et al. (2015) [40] | 2.0 | DNS | Asymmetry of Flow Field | 912 | - |
| Selvam et al. (2015) [40] | 2.0 | DNS | Friction coefficient | 1,680 | - |
| Selvam et al. (2016) [50] | 2.0 | DNS | POD study | - | - |
| Howard et al. (2017) [51] | 2.0 | LES | POD study | - | - |
| Lebon et al. (2018) [49] | 2.0 | PIV | Amplitude Threshold Curves | - | $V_{r,c} \sim Re^{-2.3}$ |
| Lebon et al. (2018) [45] | 2.0 | DNS | Amplitude Threshold Curves | - | $\delta \sim Re^{-2.8}$ |
| Moallemi and Brinkerhoff (2018) [43] | 2.0 | DNS | Reattachment Length | 1,003 (81.7) | $Lr \cong 3.537 \times 10^{7}\, Re^{-2.03} + 52.84$ |
| Nguyen et al. (2019) [46] | 2.0 | DNS | Amplitude Threshold Curves | - | $\delta \sim Re^{-3}$ |
| Shenoy et al. (2020) [47] | 2.0 | DNS | Amplitude Threshold Curves | - | $\delta \sim Re^{-2.1}$ to $\delta \sim Re^{-4.6}$ |
| Luciano et al. (2022) [48] | 2.0 | DNS | Amplitude Threshold Curves | - | $\delta \sim Re^{-9.6}$ |
| Luciano et al. (2022) [48] | 2.0 | DNS | Reattachment Length, | - | - |
| Choi et al. (2022) [21] | 2.0 | LES | Reattachment Length | 816 (69.4) | $Lr \cong 4.646 \times 10^{6}\, Re^{-1.672} + 7.471$ |
| Choi et al. (2022) [26] | 2.0 | LES | Reattachment Length | Eq.3.8 | Eq.3.10, 3.11, 3.12, and 3.13 |
| Choi et al. (2022) [26] | 2.0 | LES | POD study | Table 3.3 | |

is employed as an inlet boundary condition for the simulation. The velocity equation at the inlet is written as:

$$\boldsymbol{U}_{in} = (1-\alpha)\boldsymbol{U}_{old} + \alpha(\boldsymbol{U}_{ref} + C_{rms}|\boldsymbol{U}_{ref}|I\mathbb{R}) \tag{3.5}$$

$$\boldsymbol{U}_{ref} = 2U_b(1-(r/R)^2)\,\mathbf{e_z} \tag{3.6}$$

where $\boldsymbol{U}_{in}$ is the velocity at the inlet, $\boldsymbol{U}_{old}$ is the inlet velocity of previous time step, $\boldsymbol{U}_{ref}$ is the reference velocity, $|\boldsymbol{U}_{ref}|$ is the magnitude of the reference velocity, $\alpha$ is the fraction of new random component added to previous time value and is specified as 0.1 in the current study, $C_{rms}$ is the RMS coefficient, defined as $\sqrt{12(2\alpha-\alpha^2)}/\alpha$ and specified as 15.10 in the current study, $\mathbf{e}_z$ is the axial coordinate vector, $r$ is the radial location, $R$ is the radius of pipe, $U_b$ is the bulk velocity, $I$ is the turbulence intensity and $\mathbb{R}$ is the random function ranged between -0.5 and 0.5. .

The blue color in Fig.3.1 represents a region in which the flow reversal of averaged axial velocity exists. The time-averaged velocity profiles adjacent to the wall are extracted parallel to the axis every $5^\circ$ sections to calculate the reattachment point and averaged.

The mesh used in current study is shown in Figure 3.2. Grid information follows previous a study of the author [21]. Grid independence was established by monitoring the Grid Convergence Index [52] (GCI), and grid independence was declared when the GCI ceased to vary by more than $1\%$. The mesh size in the axial direction was kept constant at 3.33 mm, equivalent to $\Delta z^+$ =11.82, 29.50, and $45.6$ for $Re$ =1,000, 3,000, and 5,000, respectively. The cross-sectional mesh has non-uniformly sized 1,536 cells as illustrated in Figure 3.2-(left). The smallest mesh element adjacent to the wall in the upstream pipe section is specified as $7.20 \times 10^{-5}$ m, whereas in the downstream section it is $1.03 \times 10^{-4}$ m. The cell sizes in the vicinity of the wall were small enough to resolve finer gradients and were of the order of $y^+ = 1$, which is equivalent to $2.82 \times 10^{-4}$ m, $1.13 \times 10^{-4}$ m, and $0.731 \times 10^{-4}$ m for $Re$ = 1,000, 3,000, and 5,000, respectively. Figure 3.3 represents the size of meshes in radial direction for different Reynolds number.

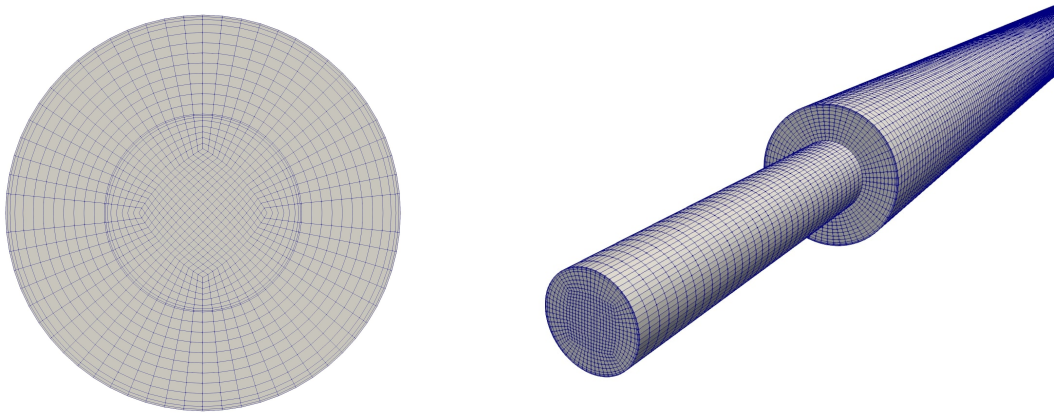

Figure 3.2: Mesh used in present study:(left) Cross-sectional view of the mesh at the outlet, (right) Three dimensional view near the sudden expansion, reprinted with permission from [26]

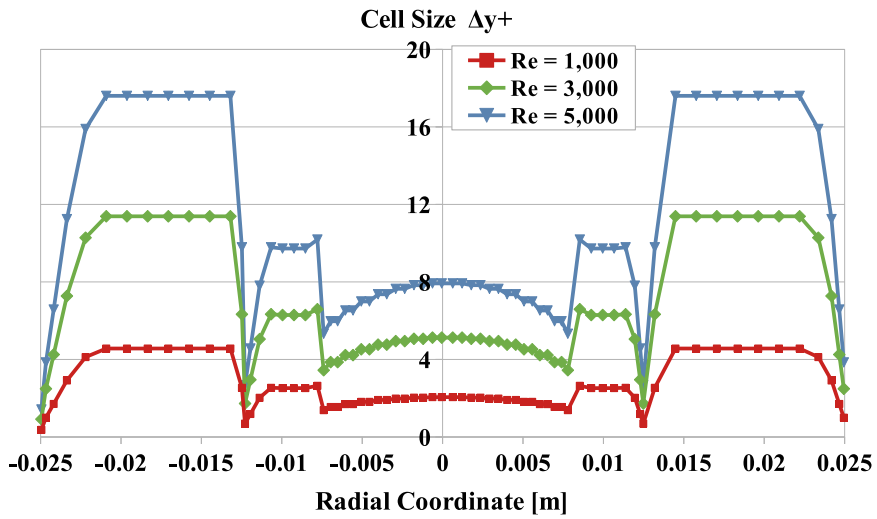


Figure 3.3: Size of meshes in radial direction for $Re$ = 1,000, 3,000 and 5,000, respectively, reprinted with permission from [26]

### 3.2.2 Settings for OpenFOAM

Time-dependent computational fluid dynamics (CFD) simulations were conducted using OpenFOAM v7, an open-source CFD simulation program. Each case was run for 48 hours or more with 48 CPUs on GRACE, comprised of Intel Xeon 6248R processor, in the high performance research computing center of Texas A&M University. The *pimpleFOAM* solver was employed. The *pimpleFOAM* iteration settings, *nOuterCorrectors*, *nCorrectors* and *nNonOrthogonalCorrectors* were set as 5, 2, and 1, respectively. Convergence at each time-step is achieved when the residual of each property was less than $1 \times 10^{-5}$ except for the final loop the criterion was $1 \times 10^{-6}$. A second-order backward difference scheme was used to calculate the temporal derivatives. The Linear-Upwind Stabilized Transport (LUST) scheme was used to calculate the first order spatial derivative of velocity, and the second-order central difference scheme was used to compute other spatial derivatives. Simulation runs were made for 24 seconds or more, and the temporally averaged velocity and turbulence quantities were calculated. Information obtained during the first one third of data was excluded from the calculation of the average of properties.

The effect of time step was investigated for Reynolds number of 1,300 with three different turbulence intensities (TI= 0.1%, 1%, and 10%). Figure 3.4 shows dependence of the reattachment length on time step. Based on GCI calculations (GCI $= (F_s\epsilon/(r^p - 1))$, a minimum time step of $5 \times 10^{-4}$ seconds was required to maintain 7% relative error for the case of TI=0.1%. A summary of time step independence studies is given in Figure 3.4 and Table 3.2. Here, $F_s$ is safety factor of 1.25, $\epsilon$ is relative error of the reattachment length between two different mesh sizes, $r$ is the ratio of mesh size, and $p$ is the order of convergence. Time steps ($\Delta t$) for $Re \leqslant$ 1,600; 1,600 $\leqslant Re \leqslant$ 5,000 and 5,000 $\leqslant Re \leqslant$ 15,000, were determined to be $5 \times 10^{-4}$ s, $4 \times 10^{-4}$ s, and $2 \times 10^{-4}$ s, respectively. Normalized time step $\Delta t^+ = \Delta t/(h/U_b)$ is 0.02572, 0.06174, and 0.1029 for $Re$ =1,000, 3,000, and 5,000, respectively.

In this study maximum Courant number varied from 0.1 to 5 depending on the $Re$, TI, and time step. However, Only a small number of cells experienced a Courant number larger than unity. Furthermore, in all cases the convergence criterion of $1 \times 10^{-6}$ was met and the GCI criteria was

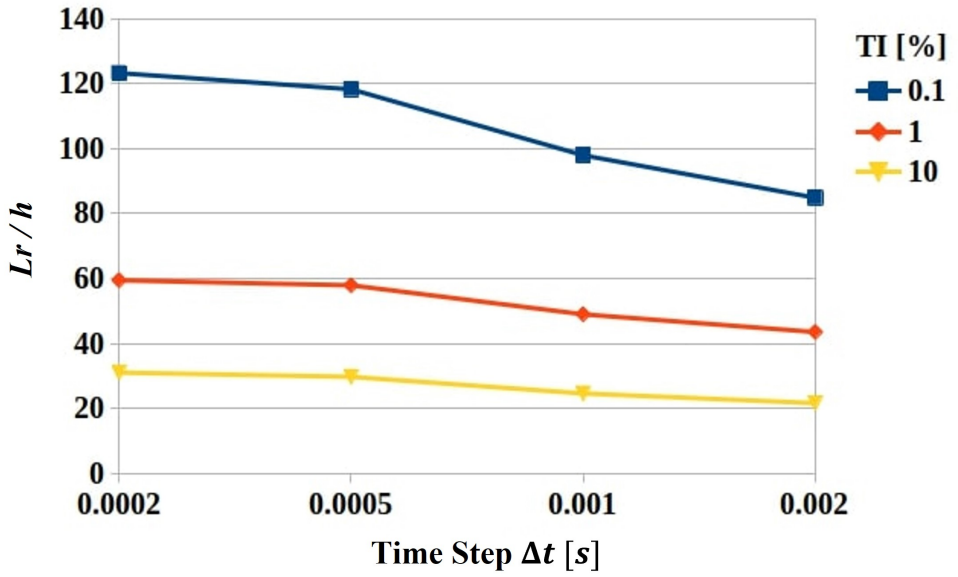


Figure 3.4: Dependence of the reattachment length on time step, reprinted with permission from [26]

used for different time steps to declare convergence. Most importantly, with current mesh size and time step size we were able to reproduce results for reattachment length similar as in the literature [4, 5, 48] to validate the current numerical simulation.

To validate the adopted mesh size , pressure gradient, stream-wise velocity, and Reynolds shear stress profiles downstream sudden expansion are calculated and compared with DNS references data [3] in Figure 3.5. Far downstream of the sudden expansion, flow can be considered as fully developed turbulent flow. The LES study for this geometry with $Re_b$=10,000 (or $Re_b$=5,000 based on downstream pipe) is compared with Eggel's DNS study for circular pipe with $Re_b$ of 5,300

Table 3.2: Grid Convergence Test for Time Step ($Re$=1,300), reprinted with permission from [26]

| TI [%] | 0.1 | 1.0 | 10 |
|---|---|---|---|
| $GCI_{12}$ [%] | 1.651 | 0.661 | 1.820 |
| $GCI_{23}$ [%] | 6.998 | 3.973 | 7.414 |

subscript 1,2 and 3 represents $\Delta t$ = 0.0002s, 0.0005s and 0.001s, respectively

[3]. As shown in Figure 3.5-(b), Pressure gradient along the pipe ($\frac{d(p/\rho)}{dx}$) obtained from the LES study is calculated as -0.9384. Using Eq.2.18, 2.19 and 2.22, shear velocity $U^*$ becomes 0.11085. Figure 3.5-(c) and (d) represents the velocity and Reynolds stress profiles as a function of $y^+$ at $100h$ far away from the sudden expansion (white line on Figure 3.5-(a), respectively, showing that LES results have good agreement with the DNS study results [3].

### 3.2.3 Proper Orthogonal Decomposition (POD)

The Proper Orthogonal Decomposition (POD) refers to a modal decomposition technique in which a set of data are expressed as a linear summation of a set of orthonormal modes with corresponding temporal coefficients [53]. Each mode is expected to describe a feature of the system. POD analysis was first introduced by Lumley [54] in the field of fluid dynamics/turbulent flows to capture the coherent structure in a temporally oscillating and spatial fluctuating turbulent flows. The set of velocity profiles in a time series can be expressed as a linear summation of the mode with corresponding temporal coefficient written as Eq. 3.7. Each mode is expected to have a coherent structure of the fluctuating flow. Since this technique enables the decomposition of a set of data into a minimal number of modes to capture as much as energy (information) as possible, velocity profiles can be expressed a sum of minimum number of modes. The method of snapshot [55] is employed to calculate eigenvalue, temporal coefficient, and mode.

$$\boldsymbol{U}(\boldsymbol{x},t) - \bar{\boldsymbol{U}}(\boldsymbol{x},t) = \sum_{i=1}^{N} \zeta^{(i)}(t)\psi^{(i)}(x) \tag{3.7}$$

where $\boldsymbol{U}(\boldsymbol{x},t)$ is instantaneous velocity, $\bar{\boldsymbol{U}}(\boldsymbol{x},t)$ is temporally averaged velocity, $\zeta^{(i)}(t)$ is temporal POD coefficient, and $\psi^{(i)}(x)$ is mode. The order of the mode is determined by the eigenvalue $\lambda^{(i)}$ in descending order, representing their energy level.

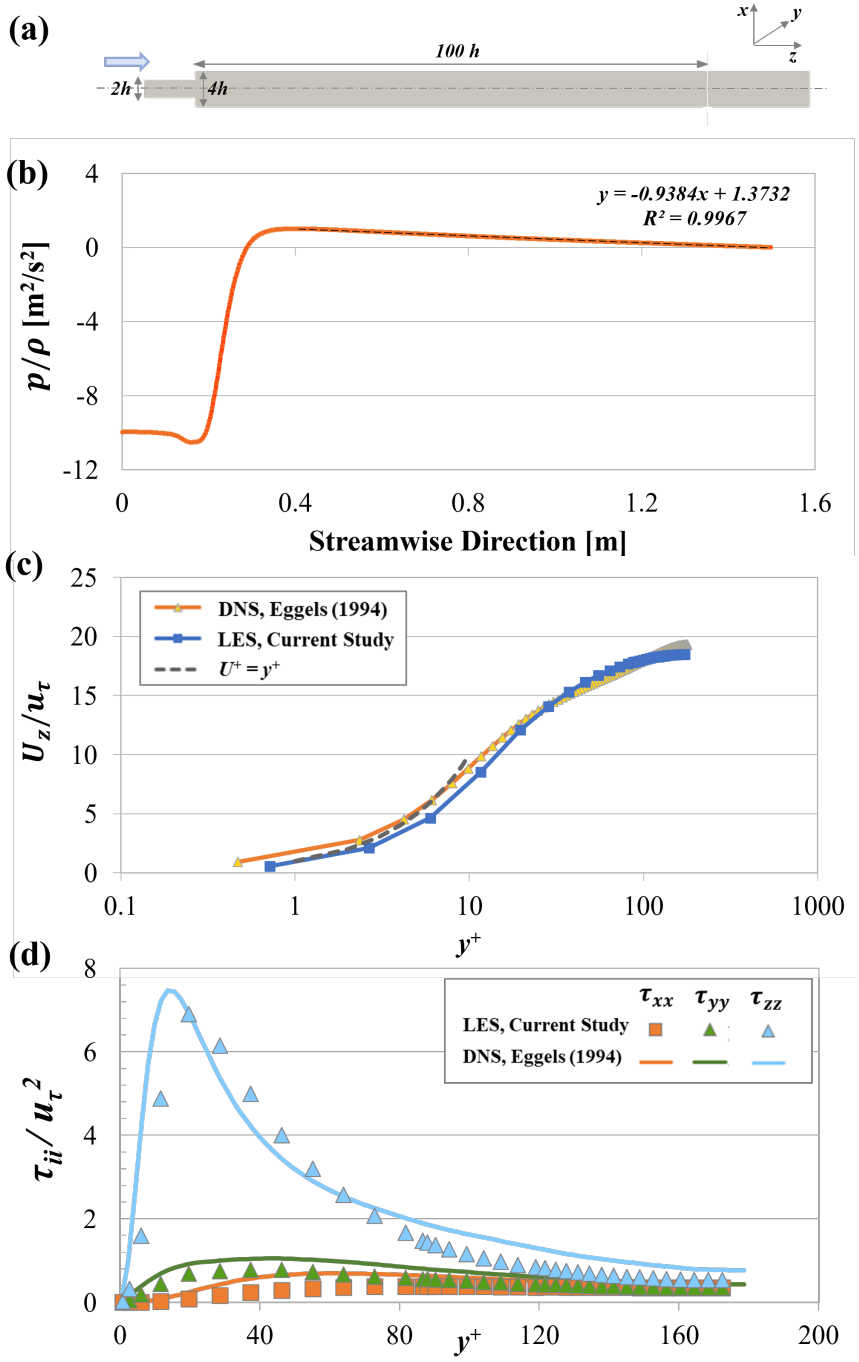


Figure 3.5: Comparison between DNS results with $Re$=5,300 for turbulence pipe flow [3] and the current study of LES downstream of an axisymmetric sudden expansion ($100h$ downstream of the expansion) with $Re$=5,000: (a) Geometry of the sudden expansion; (b) kinematic pressure on the axis obtained from LES; (c) axial mean velocity, normalized by the wall friction velocity, as a function of $y^+$; (d) Reynolds shear stress, normalized by square of the wall friction velocity, as a function of $y^+$

## 3.3 Results and Discussion

### 3.3.1 Critical points to Demarcate Laminar, Transition, and Turbulent Regions

Large eddy simulations were performed for different Reynolds numbers for the geometry of axisymmetric pipes. The reattachment length normalized by the step height ($Lr/h$) in the pipe flow is presented in Figure 3.6 as a function of Reynolds number. Solid markers represent data reported in the literature [5, 4, 43]. Hollow markers are the data obtained from the current LES calculations with different turbulence intensities. Error bars represent the range of the reattachment length in the circumferential direction. The dashed line is the universal correlation for the reattachment length proposed in this study for a given turbulence intensity (Eq. 3.12).

In absence of disturbance at the inlet, the reattachment lengths obtained from the numerical simulation maintains the trend of the laminar flow region wherein the reattachment length is linearly proportional to the Reynolds number. This trend, however, is shown to change around $Re = 2,000$ wherein the reattachment length is no longer linearly proportional to Reynolds number and becomes nearly independent of Reynolds number, as seen in the left top corner inset of Figure 3.6. With assigned numerical convergence criterion of $1 \times 10^{-6}$ the numerical error can generate flow fluctuation. The magnitude of flow disturbance due to absolute numerical error is maintained regardless of Reynolds number unlike the turbulent intensity disturbance. However, the reattachment length does not change regardless of Reynolds number in turbulent region.

With a proper amount of turbulence disturbance introduced (Eq. 3.5), the reattachment length calculated from current study is in good agreement with data reported in the literature. Latornell and Pollard [5] performed experiments with two different inlet conditions: fully developed flow (FD) depicted as a green square and Nozzle flow (NZ) depicted as a red circle in the Figure 3.6. For the FD case, inlet velocity profile is controlled by parabolic fully developed laminar flow by introducing a very long upstream, ( $> 40d$). It is expected that turbulence intensity is low at the entrance of the expansion as flow disturbances at the inlet are attenuated as fluid flows through the pipe for cases for which Reynolds number was less than 2,000. Nozzle flow, on the other hand,

employed a short nozzle upstream of the expansion and was measured as plug flow in which the turbulence intensity was expected to be high. This trend is consistent with the current study. Both the FD and NZ cases of Latornell and Pollard [5] match the current study with turbulence intensities of 1% and 20% respectively. Similarly, Pak [4] also used a short nozzle upstream of the expansion and that compared well with the results for the turbulence intensity of 20%. The current results are consistent with the explanation given by So [30] that the reattachment length decreases as the turbulence intensity increases. Moallemi [43] performed a DNS study using a different method to introduce disturbance at the flow inlet. The decreasing rate in transition and turbulent regions do not agree with the numerical results of the current study. Luciano et al. [48] also performed DNS study, showing a similar decreasing rate compared with the experimental data [5] and the current LES results. Luciano's DNS study with $\delta = 5\%$ matches the present study with TI$= 1\%$, while the case with $\delta = 1\%$ matches current study with TI$= 0.2\%$. It appears that $\delta$ is 5 times lager than TI. TI is the range of a random variable, whereas $\delta$ is the amplitude of the random variable used in Eq.3.4. The range of random variable is half of the amplitude of the random variable, and thus the two times difference is attributed to the range of random variable. Another reason $\delta$ appears larger than TI is due to the fact that the present study considered information of the previous time-step while Luciano's study [48] does not.

Flow characteristics are clearly classified in the graph of reattachment length as a function of the turbulence intensity in Figure 3.7. The marker X on the graphs in Figure 3.7 indicate the reattachment length calculated from the numerical simulation with different turbulence intensities for a specified Reynolds number. Plots of the reattachment length as a function of turbulence intensity have three distinct parts. A region in which the reattachment length has constant value, and two regions described by lines with different negative slopes on a semi-log x-axis scale plot. Flow is not affected by flow disturbance at the inlet in the laminar region as shown by the constant blue lines in Figure 3.7. On the other hands, in transition and turbulent regions flow behavior depends on the flow disturbance at the inlet. The magnitude of slope of second region (yellow line) is lower than that of third region (red line) for $Re \leqslant 800$, as shown in Figure 3.7(a-d), while it is opposite

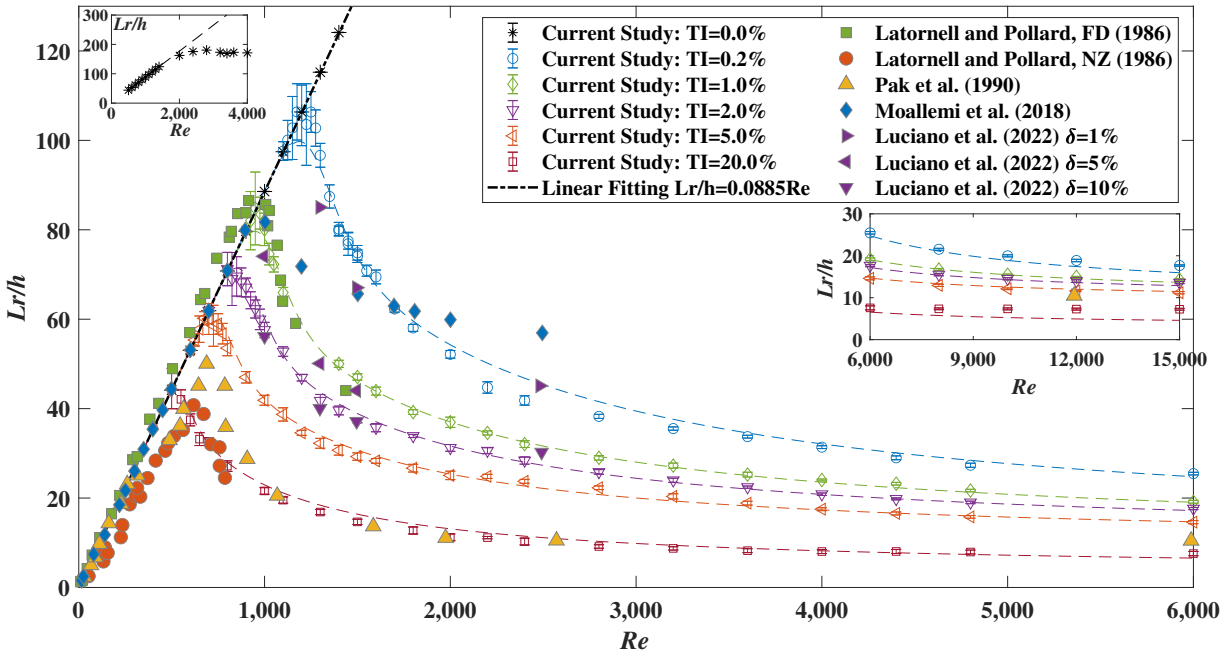


Figure 3.6: Comparison of normalized reattachment length ($Lr/h$) for an axisymmetric pipe flow as a function of Reynolds number, reprinted with permission from [26]

for cases with $Re > 800$ as shown in Figure 3.7(e-n). Three regions make two cross-over points ($Cr_1$ and $Cr_2$) between adjacent lines, which are critical points that distinguish laminar-transition (red circle, $Cr_1$) and transition-turbulent regions (blue square, $Cr_2$). To obtain the relationship between critical Reynolds number and critical turbulent intensity, parametric studies were performed by varying Reynolds number from 500 to 2,000. The critical points obtained are shown in Figure 3.8. Dashed lines are curve fitting expressions for the results of parametric study. The the relation between critical Reynolds number ($Re_{Cr_1}$, $Re_{Cr_2}$) and critical turbulent intensity ($\mathrm{TI}_{Cr_1}$, $\mathrm{TI}_{Cr_2}$) are shown in Equation 3.8 and 3.9.

Critical point dividing laminar-transition region ($Cr_1$)

$$\boldsymbol{Re}_{Cr_1} = 151.71 \ln(540.84/\mathbf{TI}_{Cr_1}[\%]) \tag{3.8}$$

Critical point dividing transition-turbulent region ($Cr_2$)

$$\boldsymbol{Re}_{Cr_2} = 217.45 \ln(231.74/\mathbf{TI}_{Cr_2}[\%]) \tag{3.9}$$

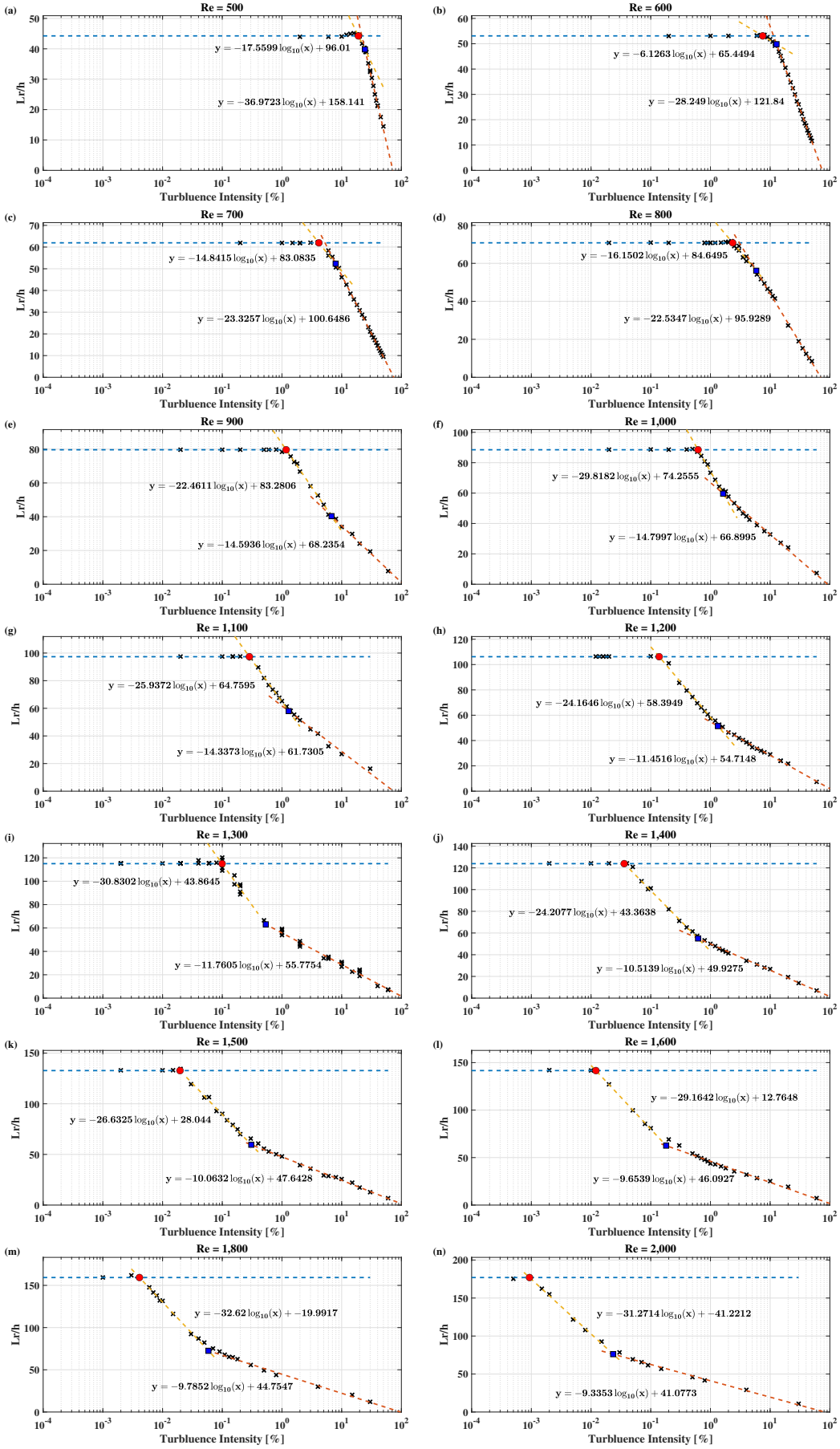


Figure 3.7: The reattachment length as a function of turbulence intensity, some subfigures are reprinted with permission from [26]

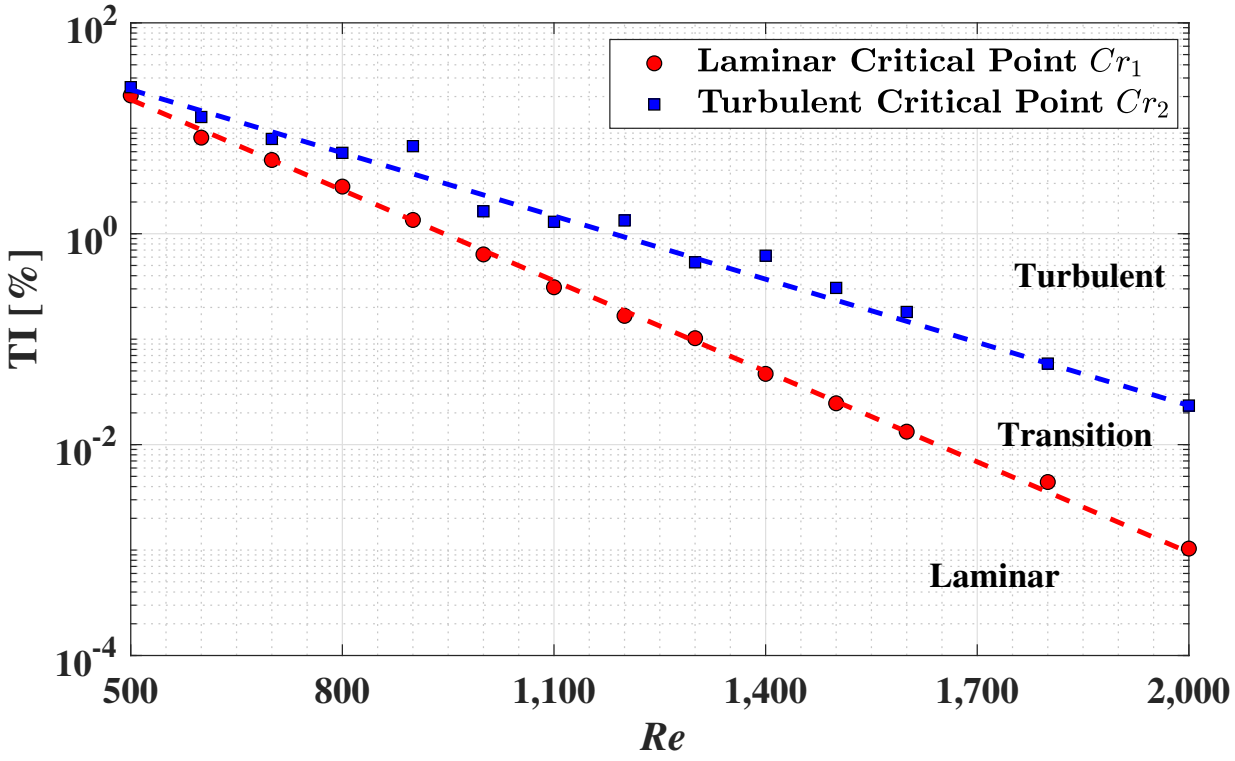


Figure 3.8: Flow Map showing Laminar, Transition, and Turbulent regions, reprinted with permission from [26]

### 3.3.2 Flow Behavior in Transitional Region

Oscillation of flow is an interesting behavior in the transitional region as shown in Figure 3.9. Figure 3.9-(a) shows a contour plot of temporally averaged axial velocity, Figure 3.9-(b) shows the mode 1 achieved from POD analysis using fluctuation velocity, Figure 3.9-(c-i) are contour graphs of instantaneous velocity as a function of time. Around the reattachment point separated shear layers suddenly break down in the middle region and the shear layer shortens while the downstream breakaway region disappears. Then, separated shear layers are elongated and recovered over time. This flow phenomena repeats with time. The spatial range of flow oscillation is similar to the first mode of the fluctuation velocity near the reattachment length.

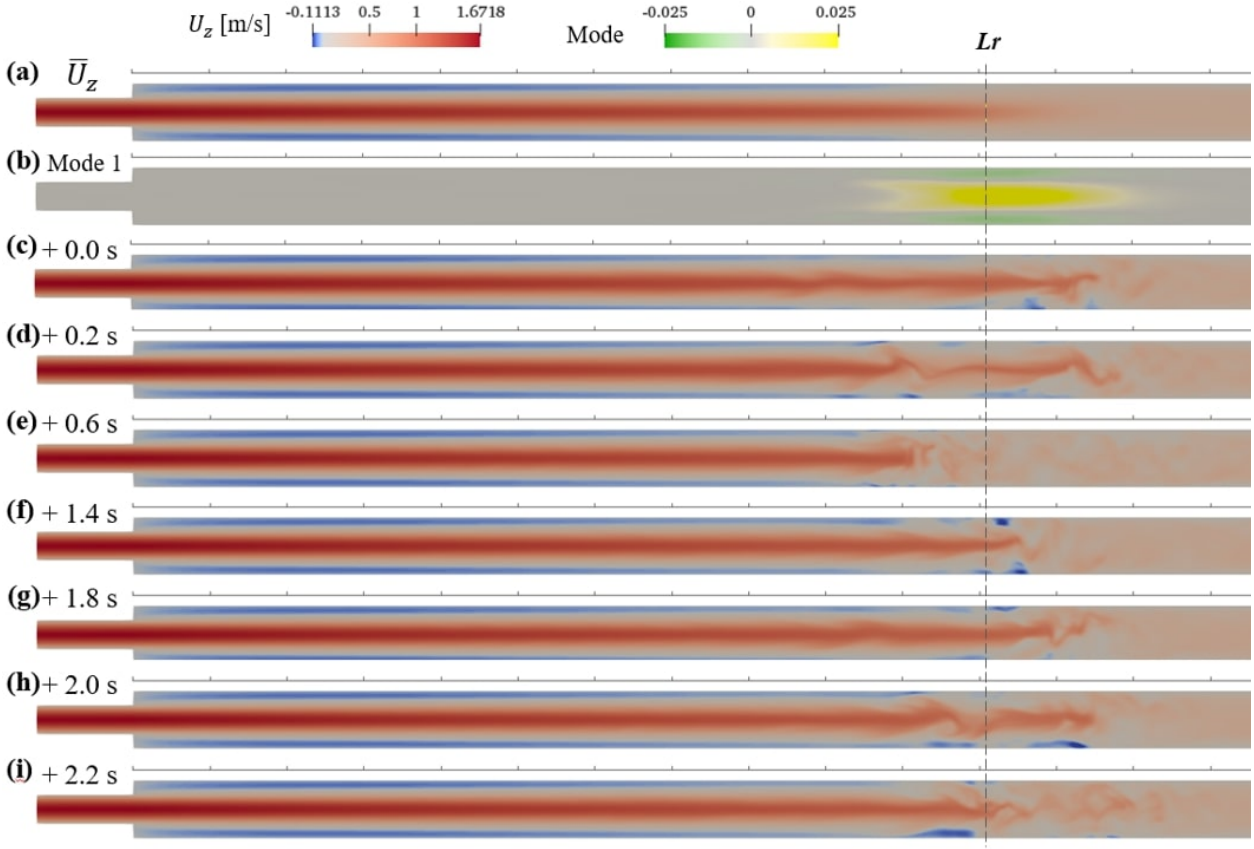


Figure 3.9: Flow oscillation over time for a flow with inlet condition of $Re$=1,300 and TI=0.2%: Contour of (a) averaged axial velocity, (b) mode 1 of POD analysis, (c-i) instantaneous velocity at the time of +0.0, +0.2, +0.6, +1.4, +1.8, +2.0 and +2.2 seconds, respectively, reprinted with permission from [26]

Asymmetricity is the another interesting flow behavior in transitional region. It can be seen from the error bars in Figure 3.6 that the asymmetric reattachment length is observed around the circumference near critical points ($Cr_1$) even though the fluid flows through an axisymmetric sudden expansion. Reattachment lengths presented in Figure 3.6 are based on integration over 16 s however, the calculations were carried out for 100 s to verify asymmetry still remained. The asymmetric reattachment is severe near the laminar critical point ($Cr_1$). The asymmetric reattachment length, is also observed in parallel plate channel expansion flow when Reynolds number exceeds the critical Reynolds number [56, 43]. A second critical point $Cr_2$ is the cross-over point of two curve fitted lines with different negative slopes observed in TI Vs $Lr$ graph (Figure 3.7). The key characteristics of this critical point is that the reattachment length obtained above this critical Reynolds number ($Cr_2$) can be represented by an expression $Lr \sim 1/Re$ regardless of turbulence intensity at the inlet.

The Fast Fourier Transform (FFT) analysis was performed for two different inlet conditions: transition case of $Re$=1,000 with TI=2% in Figure 3.10 (b-d); and turbulent case of $Re$=2,000 with TI=20% in Figure 3.10 (f-h). The calculations at which fluctuation velocities are extracted are marked in the figure 3.10 (a) and (e) showing contour of averaged axial velocities. The markers $\times$, $\triangle$, and $\bigcirc$ lies at the mesh adjacent to the wall (1.999$h$ away from the axis in the radial direction), at 1.2$h$ away from the axis in the radial direction, and on the axis, respectively. The slope of $-5/3$ is plotted as solid line, whereas that of $-4$ is plotted as dashed line. The FFT results showed the slope of $-5/3$ in mid frequency range where the energy cascade occurs. The FFT results also presents the slope of $-4$ in high frequency range where the energy is dissipated. These trends are especially observed downstream of the reattachment point where turbulence is well developed. Blue line in Figure 3.10 (b-d) and orange line in Figure 3.10 (f-h) are FFT results obtained near the reattachment length where flow oscillation and fluctuation are most severe, demonstrating that it has more small eddies than at other locations. The FFT results obtained at points near the expansion, such as point $(0,\ 1.999h,\ 16h)$ and $(0,\ 1.999h,\ 40h)$ in 3.10-(b) and point $(0,\ 1.999h,\ 40h)$ in Figure 3.10-(d), does not follow the turbulent process mentioned above. Instead, only slope of

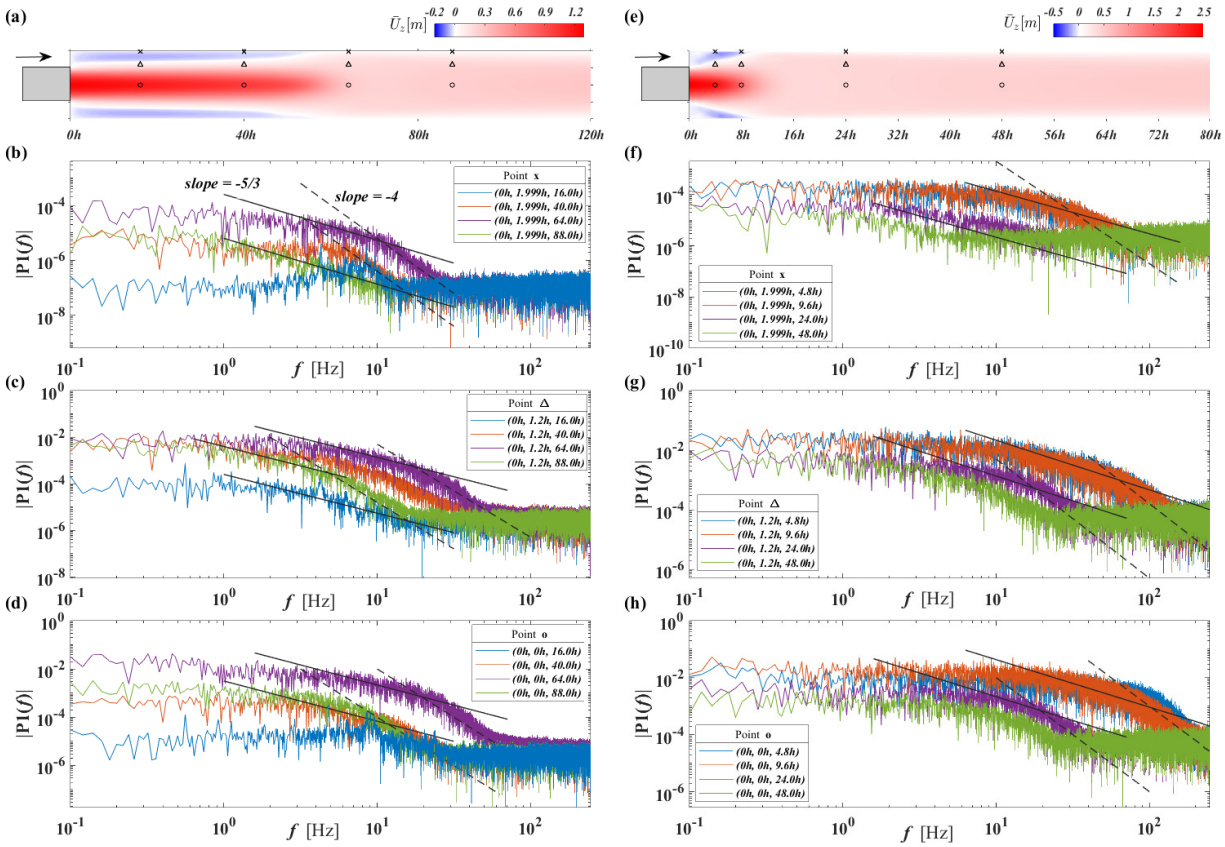


Figure 3.10: Fast Fourier transform analysis of axial fluctuating velocity at different locations: (a-d) transition case of $Re$=1,000 with TI=2%, (a) contour of averaged axial velocity, (b-d) FFT results adjacent to the wall ($\times$), at $y = 1.2h$ from the axis ($\triangle$), and on the axis ($\bigcirc$), respectively; (e-h) turbulent case of $Re$=2,000 with TI=10%, (e) contour of averaged axial velocity, (f-h) FFT results adjacent to the wall ($\times$), at $y = 1.2h$ from the axis ($\triangle$), and on the axis ($\bigcirc$), respectively, reprinted with permission from [26]

$-4$ is observed. It seems that turbulence kinetic energy is dissipated before they are fully evolved and cascaded to smaller eddies. This can be considered as the characteristics of transition flow through an axisymmetric expansion.

### 3.3.3 Results of Proper Orthogonal Decomposition Study

To identify the coherent structure of the flow through an axisymmetric sudden expansion, 2D (axial and transverse) POD analysis was performed. Eigenmode and Eigenvalue are used to classify the flow characteristics in axisymmetric sudden expansion flows. Data was sampled at every $2 \times 10^{-3}$ seconds for a period of 50 seconds giving 25,000 snapshots. Figure 3.11 represents the

first mode obtained from POD analysis of axial fluctuation velocity for different Reynolds numbers at a fixed inlet turbulence intensity (TI=2%). Note that Figure 3.11 shows the first Eigen mode (mode 1) of the fluctuating axial velocity not the actual fluctuation velocity itself. The red and blue colors indicate positive and negative modal values, respectively. The temporal coefficients could either be positive or negative and may change with time. However, the positive and negative values of mode 1 presented in Figure 3.11 do not indicate the direction of flow. Four different patterns of the first mode were observed: (p1) alternating pattern on zero shear layer ($Re \leqslant 725$); (p2) single directional strong spot pattern with twin tip ends where localized turbulence was observed ($750 \leqslant Re \leqslant 1,200$); (p3) strong spot pattern with single tip end accompanied with twin-tail-like pattern (in blue) in opposite directions ($1,300 \leqslant Re \leqslant 2,800$); and (p4) single vortex spot (Re $\geqslant$ 3,200). Note the color legend in Figure 3.11 is only employed for showing relative direction in the same mode. As sign of the temporal POD coefficient is temporally oscillating, axial velocity due to this mode can move either forward or backward. Pattern (p1) can be treated as Laminar flow where strongest fluctuation of the flow characteristics is induced by the Kelvin-Helmholtz instability on zero shear layer, whereas a strong mode spot is observed on the place where separated shear layers breakdown on pattern (p2), (p3), and (p4), which can be considered as localized turbulence near the reattachment point. Since the sign of values in the first mode of patterns (p2) and (p3) are biased to certain directions, the length of the separated shear layer is based on temporal coefficients explaining the temporal oscillation of the flow downstream of the expansion. On the other hand, in the pattern (p4), flows are not oscillating because half negative and positive values of mode 1 coexist.

This POD analysis was performed for different turbulence intensity values (TI = 0,2, 0.5 , 1, 2, 5, 10 and 20%). The results are tabulated in Table 3.3 and employed to study the flow characteristics. The interface between each pattern can be considered as the critical value of $Re$ corresponding to reattachment length. The interface between patterns p1 and p2 of mode 1 corresponds to $Cr_1$ obtained from Eq.3.8. The critical value decreases as turbulence intensity increases. This critical value from mode 1 is slightly smaller than the what was obtained by tracking the reattachment

length (Figure 3.6). It is consistent with the flow physics as the reattachment length is the result of the competition between recirculation due to laminar flow characteristics and localized turbulent flow characteristics. Similarly, the p2/p3 interface is a candidate for $Cr_2$ but it is not distinct because pattern p2 and p3 look similar and are thus hard to clearly demarcate. In addition, POD mode analysis also shows the presence of another interface between p3 and p4. Reynolds number of this interface increases as turbulence intensity decrease as shown in Table 3.3. The decreasing rate of interface p3/p4 is steeper than that of interface p1/p2.

There are other methods of using POD to estimate the critical point[39]. Figure 3.12 represents first ten eigenvalues ($\lambda^{(i)}$) normalized to the total energy of the eigenvalue ($\Sigma\lambda^{(i)}$) as a function of Reynolds number. High peak is clearly seen for mode 1 (blue line), near the critical Reynolds number characterized by the reattachment length ($Cr_1$).

Table 3.3: Critical Reynolds number, reprinted with permission from [26]

| TI [%] | $Re_c$ | $Re_c$ | Interface by first mode's pattern (Fig.3.11 and Suppl. of [26]) | | |
|---|---|---|---|---|---|
| | $Lr/h$ (Eq. 3.8) | $\lambda^{(i)}$ (Fig. 3.12) | p1/p2 | p2/p3 | p3/p4 |
| 0.2 | 1198.90 | 1,075 | 1,050 < Re < 1,075 | 1,800 < Re < 2,000 | 5,400 < Re < 6,000 |
| 0.5 | 1059.89 | 950 | 900 < Re < 925 | 1,400 < Re < 1,500 | 4,400 < Re < 4800 |
| 1 | 954.73 | 850 | 800 < Re < 850 | 1,250 < Re <1,400 | 3,200 < Re < 3,600 |
| 2 | 849.58 | 750 | 700 < Re < 725 | 1,200 < Re < 1,300 | 2,800 < Re < 3,200 |
| 5 | 710.56 | 600 | 600 < Re < 625 | 1,000 < Re < 1,100 | 2,000 < Re < 2,200 |
| 10 | 605.41 | 525 | 575 < Re < 600 | 700 < Re < 800 | 1,300 < Re <1,400 |
| 20 | 500.25 | - | 500 < Re < 525 | not distinct | 1,000 < Re < 1,100 |

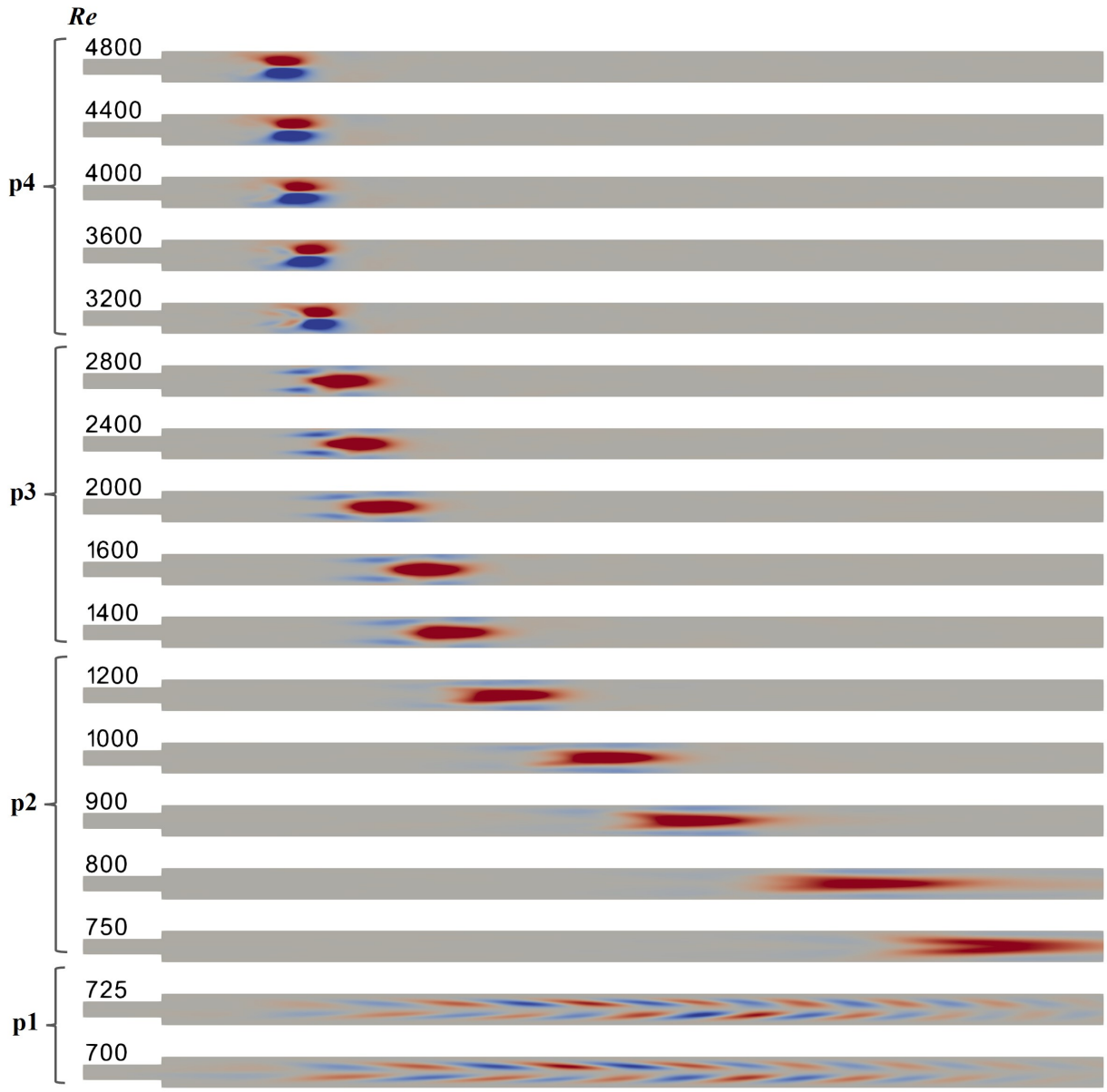


Figure 3.11: Contour graph of first mode and its classification with varying $Re$ and TI=2%, reprinted with permission from [26]

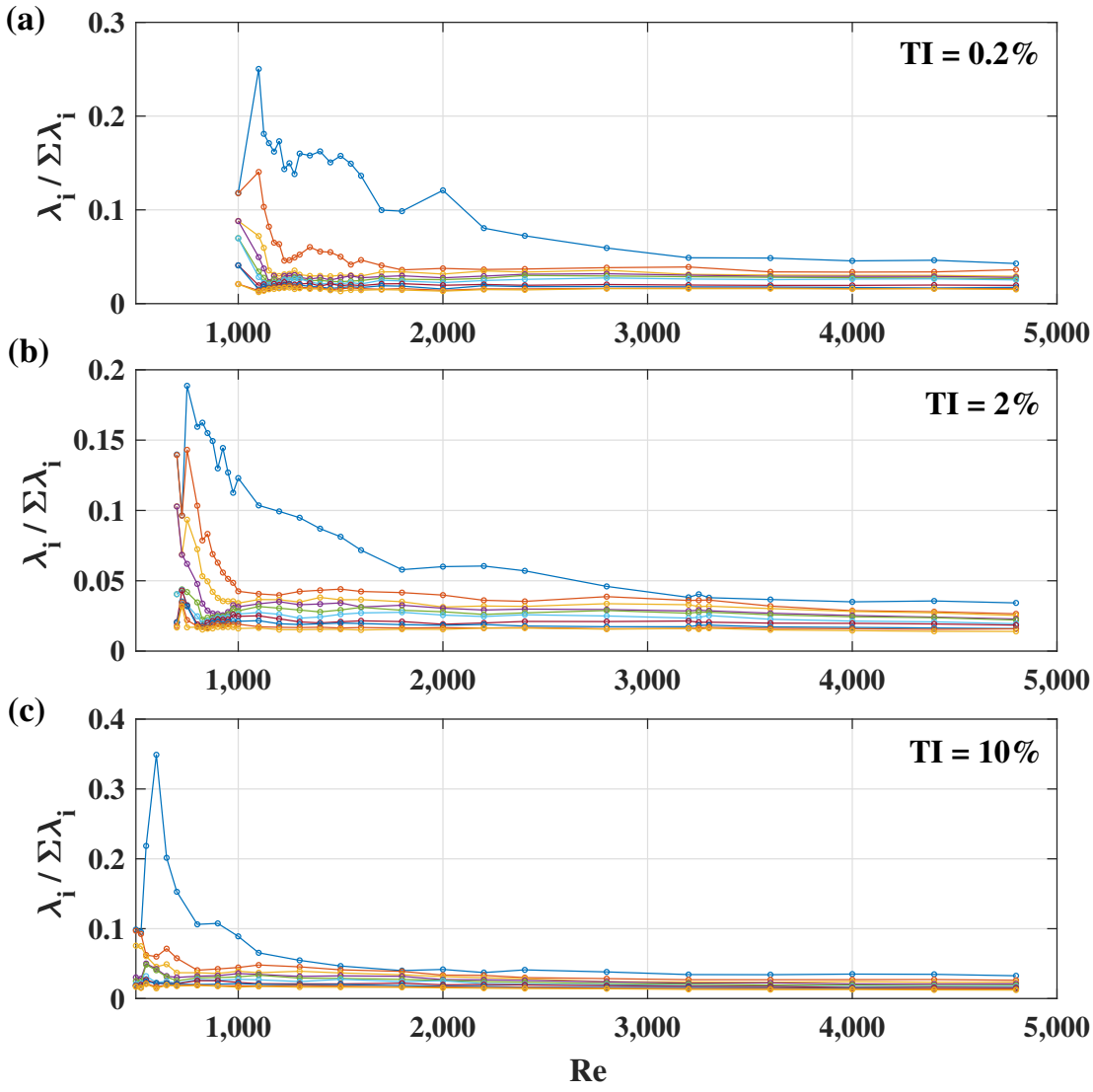


Figure 3.12: Variation of normalized eigenvalue $\lambda^{(i)}$ for varying $Re$ and TI=0.2, 2 and 10%, reprinted with permission from [26]

### 3.3.4 Overall Correlation for Reattachment Length

In Figure 3.13 curve fits for normalized reattachment length calculated using the LES approach as a function of Reynolds number for laminar, transitional, and turbulent regions are presented. An overall expression for the reattachment length of axisymmetric expansion flow is suggested in this section. Li and Djilali [57] presented an analysis for general flow including separation bubble (or flow recirculation) by using scaling analysis of the Navier-Stokes equation. The solution has three different parts: linear expression; a curve with an inverse relation to $Re$; and a constant. Papadopoulos' scaling analysis[58] includes the effect of the inlet flow condition and has two equations describing laminar ($S_L$, Eq.3.10) and turbulent ($S_T$, Eq.3.11) flow regions, respectively. The Laminar region is one in which the reattachment length linearly increases with the Reynolds number (Eq.3.10). On the other hand in turbulent region the reattachment length is inversely proportional to the Reynolds number (Eq.3.11). If the Reynolds number goes to infinity, only constant coefficient D remains in (Eq.3.11), consistent with the current calculations that the Reattachment length is independent of the Reynolds number.

$$S_L = Lr/h = A(Re - B) \tag{3.10}$$

$$S_T = Lr/h = C/Re + D \tag{3.11}$$

Avila and Hof [59] showed that laminar-turbulence intermittency is an intrinsic feature of shear flow. The flow switched intermittently between turbulent and laminar flow regiemes. Papadopoulos [58] introduced intermittency factor $\lambda$ and a solution for the transition region can be expressed as proportional summation between solutions for laminar and turbulent regions as written below

$$S = (1 - \lambda)S_L + \lambda S_T \tag{3.12}$$

where, $\lambda = 1 - 1/[1 + n(Re/Re_{Cr_1})^m]$ is intermittency factor with parameter $n$ and $m$, $Re_{Cr_1}$ is Critical Reynolds number for laminar/transition region

In this chapter, coefficients in Eq.3.10, Eq.3.11, and Eq.3.12 are estimated by using a parametric study. The value of coefficients is estimated for each constant turbulence intensity and their relationships are established. The LES results are divided into three different regions based on the critical point expressions suggested in this study (Eq.3.8 and Eq.3.9) and used for obtaining expressions for coefficients. A curve fitting tool in MATLAB R2020a was employed. Figure 3.13 shows how coefficients are divided into three different regions and how they are estimated. Coefficients A and B in Eq.3.10 do not depend on the turbulence intensity as shown in Figure 3.6 and are estimated as 0.0885 and 0, respectively. Coefficients C and D in Eq.3.11 can be expressed as the function of turbulence intensity as shown in Figure 3.14. The coefficients for the expression yield

$$A = 0.0885 \tag{3.13a}$$

$$B = 0 \tag{3.13b}$$

$$C = 72,527.81\ (\mathbf{TI\ [\%]})^{-.22} - 18,430.95 \tag{3.13c}$$

$$D = 10.28/(1 + (\mathbf{TI\ [\%]}/15.00)^{1.95}) \tag{3.13d}$$

Once the coefficient expression for laminar and turbulent flow regions and critical Reynolds number (Eq.3.8) are determined, coefficients $n$ and $m$ in the intermittency factor $\lambda$ are estimated. Coefficients $n$ and $m$ are determined to be 0.3 and 15, respectively, to minimize the total error defined as the summation of relative error between the entire LES results and the curve fitted expression Eq.3.12. The correlation has maximum error of 10% compared with the LES results for TI $\leqslant$ 10% and that of 17.3% for TI = 20% near the laminar critical point. For most cases the error is under 5%, which is an acceptable error band for the correlation. A dashed line in Figure 3.6 represents the overall correlation of Eq. 3.12 as a function Reynolds number, which fits well with the LES results depicted as same-colored markers on the figure. Each color represents a different turbulence intensity.

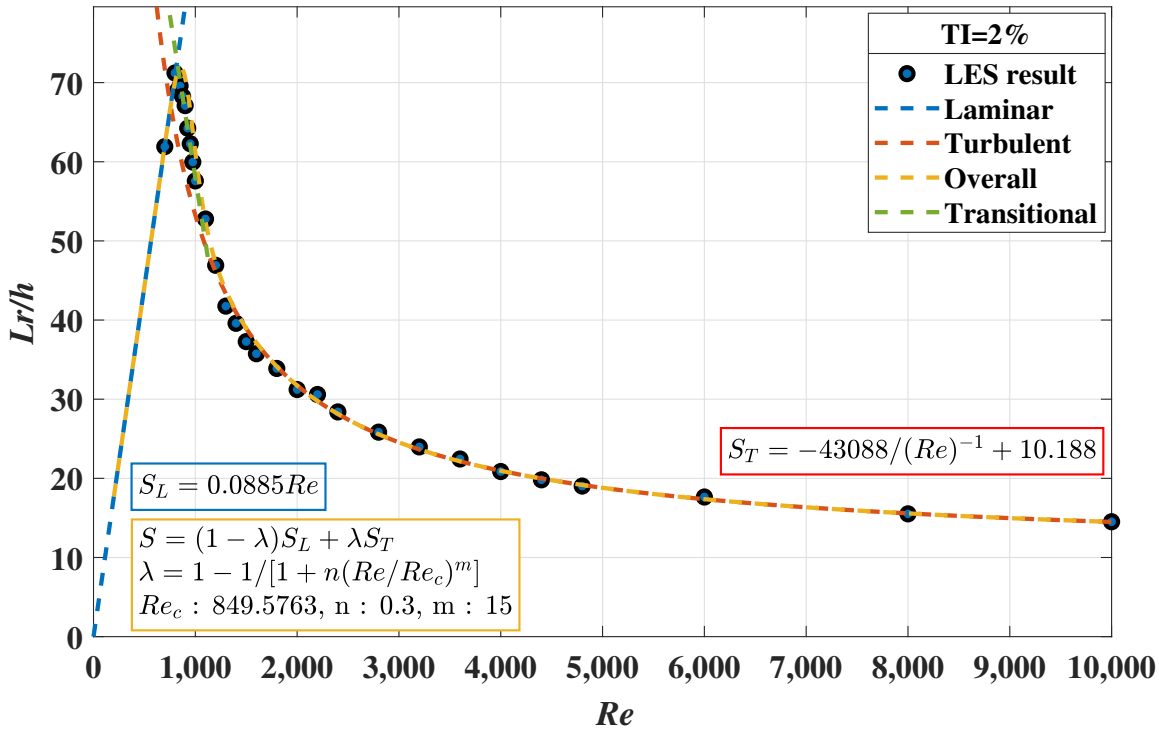


Figure 3.13: Curve Fitting for Laminar, Transition, and Turbulent Regions, reprinted with permission from [26]

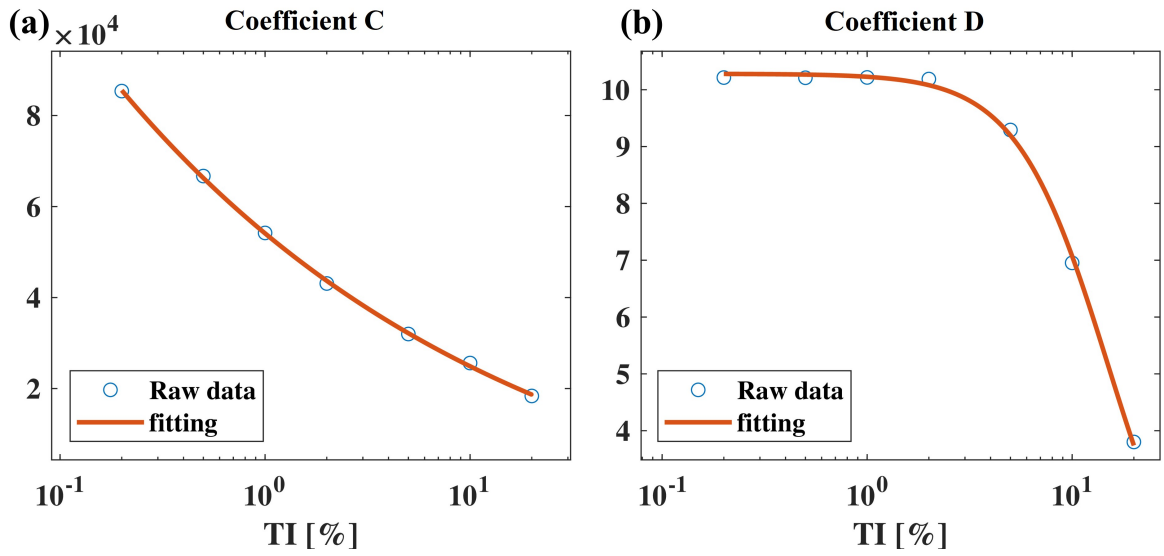


Figure 3.14: Curve Fits for (a) coefficient C , (Eq. 3.13c); and (b) coefficient D (Eq. 3.13d), reprinted with permission from [26]

## 3.4 Conclusion

Large Eddy simulations were performed for flows through an axisymmetric sudden expansion to investigate the effects of the inlet condition such as Reynolds number and turbulence intensity. The reattachment lengths calculated in the present study are in good agreement with the experimental results [5, 4] and numerical simulations in the literature [48] with the proper introduction of turbulence intensity values in the range of 0.2% to 20% as seen in Figure 3.6. It can be concluded that the turbulence intensity (TI), a commonly used parameter to quantify flow disturbance, captures the impact of the effect of flow disturbance not only on the reattachment length but also on critical threshold values for dividing laminar/transition and transition/turbulent regions of flows through an axisymmetric sudden expansion.

Three critical points are observed in a flow through an axisymmetric sudden expansion and investigated in this study. The laminar region can be defined as the region that the reattachment length is independent of turbulent disturbance at the inlet for a given Reynolds number, whereas the reattachment length decreases as the turbulence intensity decreases in the transition region. This threshold value is denoted $Cr_1$ and the correlation is established as Eq.3.8. This critical point is also clearly seen in the region between pattern p1 and p2 calculated from mode 1 of the POD analysis (Figure 3.11), and corresponds to the peak Eigenvalue of mode 1 (Figure 3.12). The second critical point $Cr_2$ is the cross-over point of two curve fitted lines with different slopes observed on TI vs. $Lr$ graph (Figure 3.7). The correlation expression achieved in this study is Eq.3.9. The key characteristic of this critical point is that reattachment lengths obtained above this critical Reynolds number can be represented by $Lr \sim 1/Re$ regardless of turbulence intensity at the inlet. We determined that flow conditions above $Cr_2$ are in the turbulent region. This critical region is also seen in the POD analysis. The critical point between pattern p2 and p3 of mode 1 might be a candidate for the $Cr_2$ but requires processing of inordinate amounts of data. POD mode analysis also clearly presents another interface between p3 and p4. However, further study is necessary to understand its physical meaning.

Finally, universal correlation for the reattachment length is established (Eq.3.12). One of the

reasons why there is no consensus on the critical value of flow disturbance is that many of the studies reported in the literature try to develop one curve fit equation for both transitional and turbulent regions. But in this study not only correlations for reattachment length for laminar, transition, and turbulent regions are presented also, an universal curve fit is presented (Eq.3.12). Eq.3.10 and its coefficients A and B (Eq.3.13a and Eq.3.13b) are employed for the region below the $Cr_1$, whereas Eq.3.11 and its coefficients C and D are employed for the region (Eq.3.13c, Eq.3.13d) above $Cr_2$. The transition region between $Cr_1$ and $Cr_2$ can be expressed as a summation of solutions for laminar and turbulent regions with intermittency factor $\lambda$ (Eq.3.12). The intermittency factor $\lambda$ can be calculated with parameter $Cr_1$ (Eq. 3.8), $n = 0.3$ and $m = 15$. Since the intermittency factor goes to zero in the laminar region while going to unity in the turbulent region, this expression can be used for both laminar and turbulent regions. The correlation expression for the reattachment length normalized to the step height can be expressed as a function of Reynolds number and turbulence intensity for $500 \leqslant Re \leqslant 15,000$ and 0.2% $\leqslant$ TI $\leqslant$ 10% within 10% error. Error might increase up to 32% at TI=20%.

# 4. MIXING IN A PIPING SYSTEM SIMULATING THE FISSION PRODUCT VENTING SYSTEM**

The contents presented in this chapter was published by the author in *Nuclear Engineering and Design* [21]. The results of numerical studies on quantification of multicomponent mixing in a scaled Fission Product Venting System (FPVS) test facility is detailed in this chapter.

## 4.1 Introduction

Texas A&M University is participating in the Versatile Test Reactor (VTR) project by the Department of Energy (US DOE) to study the transport of gaseous fission products in the fission product venting system (FPVS) test facility of the Gas Fast Reactor Cartridge Loop (GFR-CL). The VTR programs aim to incorporate multiple cartridge loops, each operating with different coolants (i.e., liquid metal, molten salt, sodium, and helium) to accelerate the testing of advanced nuclear fuels, materials, coolants, instrumentation, and controls. Several industry partners, such as General Atomics (GA), have invested in advanced nuclear reactor technology. The Energy Multiplier Module (EM2) is a conceptual design by GA for a helium-cooled fast reactor. Therefore, the helium-cooled CL is a candidate for testing in the VTR facility that will aid the design and construction of gas-cooled reactors in future.

The FPVS is designed to extract and transport an adequate amount of fission products produced in the GFR-CL, comprising the primary coolant in a circular cross-section loop along with fission gases such as xenon, krypton, and iodine, and similar fluids that flow through the FPVS loop. The transport phenomena inside the FPVS are quite complex because of the mixing of multicomponent fluids, which flow through curved sections at high pressures and temperatures. The flow within the FPVS can vary from laminar to turbulent. Heat generation in the reactor might induces a temperature gradient within the loop. Curved sections in the loop generate Dean flows, re-laminarization, and swirl-switching phenomena. The GFR-CL and its FPVS are operated under high pressure

**This chapter is reprinted/adapted with permission from [21]

and high temperature, with helium as the primary coolant or medium. The expected fission products are xenon, cesium, krypton, iodine, and like. Under accident conditions, the fission products might include solid particulates. These operating conditions and materials cannot be replicated in a university laboratory environment owing to safety considerations. Thus, a scaling analysis was performed. Air was identified as the primary coolant, and argon and carbon dioxide were identified as surrogate fission product gases. Thus, a low-pressure low-temperature (atmospheric conditions) transparent facility was constructed following a scaling exercise. The transparent loop was operated under standard atmospheric temperature and pressure conditions. Air was used as a surrogate primary coolant in lieu of helium and argon was used as a surrogate fission product gas. Other conditions, such as the flowrate, were modified based on similitude.

The numerical simulation conducted in this study focused on a low-pressure low-temperature transparent experimental test facility. There were two distinctive geometries in the loop that impacted the flow and mixing of the primary surrogate coolant and surrogate fission product gases. These included a pipe expansion where the diameter of the pipe was increased with a pipe coupling and elbows (90° bends).

The geometry of sudden/gradual expansion is one of interesting aspects with respect to mixing. Component mixing in the pipe flow is almost completed by localized turbulence observed downstream of the sudden expansion, which is demonstrated in the later part of this chapter. As discussed in Chapter 3, the reattachment length related to localized turbulence downstream of the sudden expansion depends on turbulence intensity (TI) at the inlet as well as on Reynolds number. Furthermore, it is very sensitive both turbulence intensity and Reynolds number. Thus, an appropriate amount of flow disturbance should be estimated and introduced for mixing simulation to obtain accurate results. For example, whether multicomponent is fully mixed or not upstream of the 90° bend could change entire mixing behavior within FPVS system. Another factor one needs to consider to simulate flow through the sudden expansion is that the localized turbulence could be generated even in the laminar region of a circular pipe flow with a Reynolds number below 2,100. This implies that laminar and turbulent flows can coexist in pipe expansion flows. Numerical simu-

lation of flow through the scaled FPVS test facility built at Texas A&M University had to consider the possibility of co-existence of both laminar and turbulent flows because the expected operating conditions of the facility includes Reynolds number range of 1,000 to 5,000. This fact prevents the conventional RANS-based turbulence models from being used. Hence, either the LES or the DNS approaches are required to simulate flows through the expansion geometry in the scaled FPVS test facility.

Flow through a 90° pipe bend displays an interesting flow behavior with respect to the mixing and is rich flow physics. Experimental measurement of velocity fields through 90° pipe bends flow with Reynolds number (Re) of 6x$10^4$ and Curvature ratio (CR) of 2.0 was performed by [60], showing that high axial velocity was observed at inner wall of the bend at 30° angle, and it was shifted to the outer wall of the bend downstream of the 90° pipe bend. Secondary flow and biased axial velocity distribution toward outer wall of the bend was remained even up to $10d$ downstream of the bend exit. Flow separation and reattachment were observed in the elbows. Numerical simulations with $k-\epsilon$ model [61] and [62] showed that for *Re* of 1x$10^5$, the separation angle was found to be 61°, 73° and 88.8° for CR values of 0.75, 1.0 and 1.25, respectively, and the reattachment point was observed to be 0.05D $\sim$ 0.31D downstream of the 90° elbow. Rütten [63] performed large eddy simulation (LES) of flow through a 90° pipe bend for *Re* of 5,000, 10,000, 27,000 and CR of 1.0 and 3.0. Rütten [63] reported that the flow separation was observed at the bend geometry with CR of 1.0 while no separation was found at the bend geometry with CR of 3.0. Also, a pair counter-rotating Dean vortices was observed in the pipe bend flow and the size and axis of each vortex was switching continuously, referred to as the swirl switching phenomena. The review paper written by Kalpakli-Vester [64] described flow through bends in detail. Carlsson [65] studied that very-large-scale motions (VLSMs) is related to switching in pipe bend flow by performing proper orthogonal decomposition (POD) analysis was performed using the LES results for the geometry with $Re$=34,000 and CR=1$\sim$1.67. There are some direct numerical simulation (DNS) results for flow through 90° pipe bend. Nooran [66] performed DNS for 90° pipe bend at moderate*Re* of 5,300 and 11,700 and curvature ratio of (CR) of 5. Hufnagel [67] studied swirl-

switching in pipe bend flow for *Re* of 11,700 and CR of 1.67 using 3D POD analysis with DNS.

The objective of this study is to numerically investigate the mixing in the scaled FPVS test facility. There are some challenges. First, pipe flow with moderate Reynolds number number (1,000∼5,000) estimated by the means of numerical simulation is unclear so far. It is expected that the flow separation and reattachment observed downstream of the expansion and the downstream of pipe bend can affect mixing in the pipe flow because separated recirculation layer might attenuate mixing. Furthermore, strong localized turbulence induced downstream of the expansion can enhance mixing. However, only a few numerical studies attempted to estimate reattachment length for transition flow through a sudden/gradual expansion. Moallemi [43] estimated the reattachment length for the sudden expansion flow as a function of Reynolds number using the DNS technique but their result is overestimated compared with other experimental data for flow in the transition region. Nguyen [46] and Shenoy [47] studied characteristics of flow through sudden/-gradual expansion as a function of turbulence disturbance at the inlet but they did not estimate the reattachment length. Furthermore, DNS requires enormous computational resource and thus is not feasible for parametric studies.

In this study, the validation of the LES model to estimate the reattachment length numerically for expansion flows is performed. The solver *reactingFoam* with the LES wall-adapting local eddy-viscosity (WALE) model in OpenFOAM v8 was selected for the CFD simulation. To validate the model, axial velocity profile calculated from the LES is compared with particle image velocimetry (PIV) measurement in the scaled FPVS test facility and the numerically calculated reattachment length is compared with the data reported in the literature. It was found that turbulent disturbance at the inlet flow is the key factor in estimating the reattachment length in flows through the expansions.

With the validated model, multi-component CFD simulation was performed for flows through the FPVS test facility with *Re* of 2,400, ER of 1.5, and CR of 4.0. The flow characteristics and mixing behavior in a scaled the FPVS test facility and the identification of best locations for measuring velocity and concentration for sampling. The concept of absolute mixing index (AMI) was

introduced to quantify the component mixing at each cross-section as a function of axial distance. The parametric study for the flow rate at the porous wall showed that the mixing length determined by AMI is related to the reattachment length of flow through the expansion flow.

## 4.2 Experimental and Numerical Setup

### 4.2.1 Geometric configuration and scaling

The system discussed in this chapter is shown in Figure 4.1-(a), referred to as low pressure low temperature (LPLT) FPVS test facility. The geometry of the domain to mimic the LPLT FPVS test facility is shown in Figure 4.1-(b). The LPLT FPVS test facility has a U-type loop and operates in an open-loop mode. During the open-loop test, the scaled high-temperature absorber (HTA) part shown on the left of Figure 4.1 is disassembled from the facility. Coolant gas is introduced at the "inlet" and surrogate gas is injected into the loop through the porous wall from the ambient surrogate gas surrounding to simulate the flow through GFR CL. The porous wall lies in the middle part of the thin pipe with a length of 76.2 mm. The region surrounding the porous tube was not simulated but was specified as a boundary condition in this study.

This loop is comprised of two different sizes of pipe, with inner diameters of 25.4 mm and 38.1 mm, respectively. Expansion ratio (ER = *d/D*) is 1.5. A part connecting two pipes of different diameters is called a reducer or enlarger coupling. The region downstream of the enlarger coupling from a thin pipe to a thick pipe is of interest and named as "expansion-flow region" in this study. Similarly, Dean flows occur at the pipe bend is of interest in this study as it impacts mixing, too. The "Dean-flow region" is comprised of two 90 degree elbows and connecting straight pipe between each elbow. Curvature ratio (CR = $R_c/D$) of each elbow is 4 in this study, where $R_c$ is radius of curvature of the loop, D is diameter of the pipe.

The surrogate fluids were chosen based on scaling performed to simulate the mixing of helium coolant and fission gas that occurs in the FPVS. Dimensionless parameters, such as the Froude, Schmidt, Richardson, and Reynolds numbers, which govern the thermal-fluid dynamics of the studied phenomena were applied in the scaling. The Thermal-fluid dynamics similarity of the

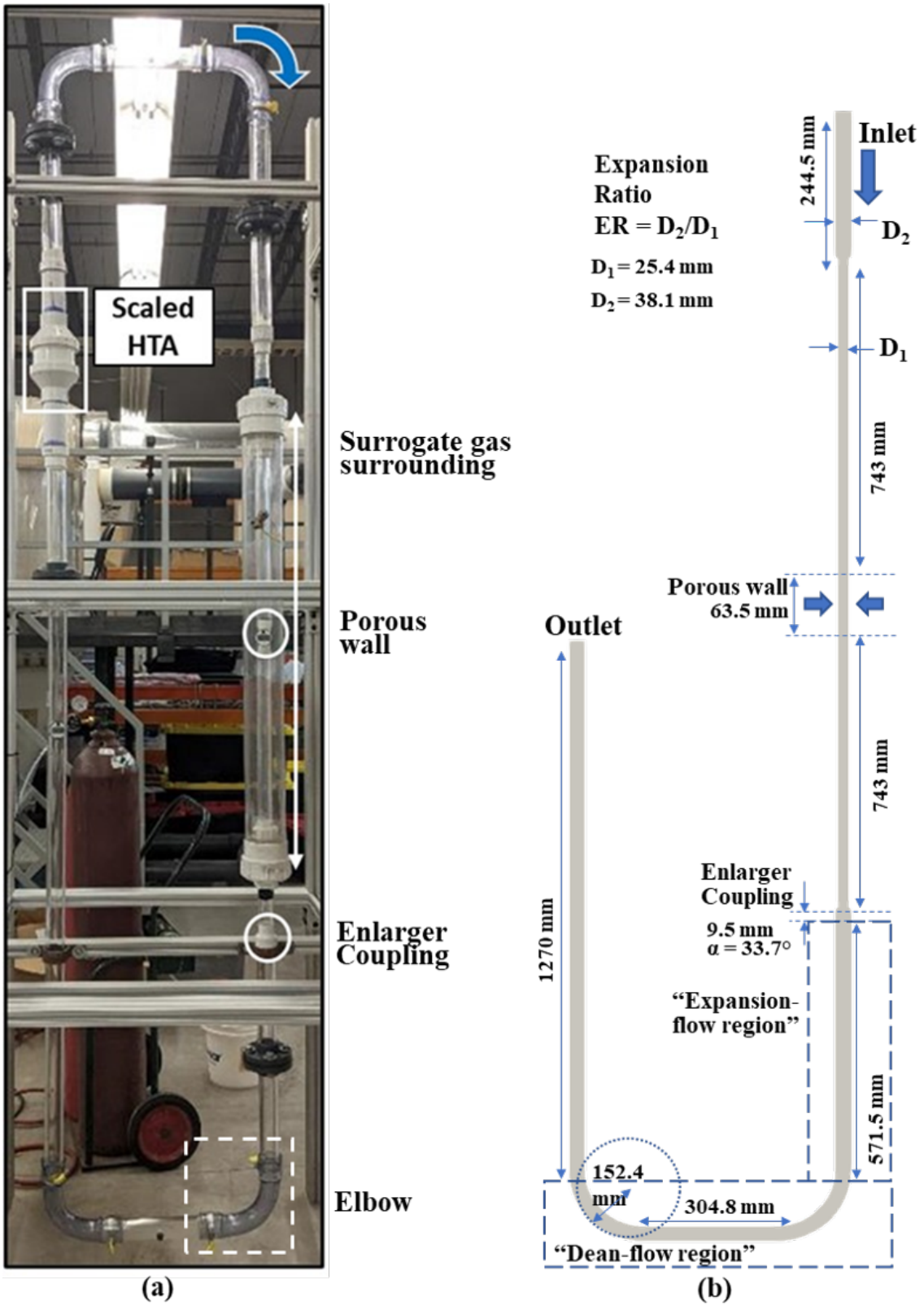


Figure 4.1: (a) Low-temperature, low-pressure experimental facility, (b) Schematic geometry used in the numerical simulation, reprinted with permission from [21]

experimental facility and cartridge loop was obtained by imposing the ratio of the dimensionless numbers equal to unity. The similarity of the Froude, Richardson, and Reynolds numbers are related to length, temperature, and velocity scaling, respectively. The Schmidt number similarity is related to the thermal-fluid properties of helium and air. To guarantee the thermal-fluid dynamics similarity of the model to the prototype, the ratio of the dimensionless numbers was set to unity:

$$\Psi_R = \frac{\Psi(model)}{\Psi(prototype)} = \frac{\Psi_m}{\Psi_p} = 1 \tag{4.1}$$

where subscripts m, p and R denote the "model", "prototype", and their ratio, respectively. Through algebraic manipulation, Reynolds and Froude numbers give the velocity of the working fluid as a function of the properties of both the model and prototype and the prototypical velocity.

$$U_m = \sqrt[3]{\frac{\nu_m}{\nu_p}\frac{\rho_m^{'}}{\rho_p^{'}}U_p^3} \tag{4.2}$$

where $\nu$ is the kinematic viscosity, $\rho^{'} = \frac{\rho_{coolant}-\rho_{fissiongas}}{\rho_{coolant}}$, and $\rho$ is the density. The fluids were assumed to be under isothermal conditions. The porous region was scaled to one-to-one ($L_m/L_p = 1$) and the high temperature abosrber (HTA) has a scaling of 1 to 23 ($L_m/L_p = 1/23$). The rest of the geometric parameters were established to accommodate required flowrate.

The temperature and pressure for LPLT FPVS test faclity were specified as room temperature 300 K and atmospheric pressure , respectively. From this similitude analysis, the primary and secondary surrogate gases were identified as air and argon, respectively. For this study. the inlet velocity in the test facility was determined to be 1 m/s and 0.002856 m/s at the porous wall.

### 4.2.2 Numerical setup

Time-dependent multicomponent fluid simulation was conducted using OpenFOAM v8, an open-source CFD simulation program. The *ReactingFOAM* solver was employed. This is a *pimpleFOAM*-based multicomponent variant-density flow solver. The time step was specified as between 1x$10^{-4}$ and 1x$10^{-3}$ seconds, not to exceed Courant-Friedrichs-Lewy (CFL) value of 3 dur-

ing the simulation run. The *PimpleFOAM* iteration settings, *nOuterCorrectors*, *nCorrectors* and *nNonOrthogonalCorrectors* were set as 5, 2, and 1 respectively. Convergence at each time-step is achieved when the residual of each property was less than $1\text{x}10^{-5}$ except for the final iteration of the outer loop was $1\text{x}10^{-6}$. A second-order backward difference scheme was used to calculate the temporal derivative. The Linear-Upwind Stabilized Transport (LUST) scheme was used to calculate the spatial derivative of velocity, and the second-order central difference scheme was used to compute other spatial derivatives. Simulation runs were made for 20 seconds, and the temporally averaged velocity and turbulence quantities were calculated. Information achieved during the first 5 seconds was excluded from the calculation of the average of properties.

We adopted the LES with the WALE model [19], which can be used from the laminar to turbulent region for anisotropic flows. Li [20] conducted LES with a WALE model to reproduce the turbulent flows of twin parallel jets and observed good agreement with the PIV measurements. In addition, the results of the LES was compared with the PIV measurements made in the LPLT FPVS test facility and found to agree well. This is explained in detail in the next section. Therefore, The WALE LES model was selected as the turbulence model in this study. The velocity profile of the fully developed laminar flow in the circular pipe was used as the inlet velocity condition. To initiate the turbulence in the pipe flow, a random fluctuation in velocity was introduced at the pipe inlet and a normal component of velocity was introduced at the inlet (0.1$\sim$1% of the axial velocity). The built-in boundary condition *turbulentInlet* of the OpenFOAM v8 is employed as a inlet boundary condition. The velocity equation at the inlet is written as:

$$\boldsymbol{U}_{in} = (1-\alpha)\boldsymbol{U}_{old} + \alpha(\boldsymbol{U}_{ref} + C_{rms}|\boldsymbol{U}_{ref}|I\mathbb{R}) \tag{4.3}$$

$$\boldsymbol{U}_{ref} = \delta U_b\, \mathbf{e_x} + 0\, \mathbf{e_y} + U_b\, \mathbf{e_z} \tag{4.4}$$

where $U_{in}$ is the velocity at the inlet, $U_{old}$ is the inlet velocity of previous time step, $U_{ref}$ is the reference velocity, $|U_{ref}|$ is the magnitude of the reference velocity, $\delta$ is the fraction of flow disturbance compared with mainstream flow, $\alpha$ is the fraction of new random component added to

previous time value, $C_{rms}$ is the RMS coefficient, the z coordinate is the axial direction, $U_b$ is the mean velocity, $I$ is the turbulence intensity and $\mathbb{R}$ is the random function ranged between -0.5 and 0.5. .

### 4.2.3 Experimental measurement technique

The basic working principle behind Particle Image Velocimetry (PIV) measurement technique deals with quantifying the pixel displacement of the seeding particles in the fluid for sequential images. An instantaneous velocity vector can be calculated by estimating the pixel displacement between consecutive images. The main components to perform the measurement technique include reflective seeding particles, a light source, optical instruments, and a camera. In this study, a 10 W monochromatic continuous laser of a visible wavelength of 532 nm is employed along with a CMOS Phantom M310 camera. The laser paired with a collimator and optical lenses (TSI 610026) illuminates the seeding particles and reflected light is captured by the camera sensor to create images. Both the laser head and the camera were mounted on separate motorized-traverses to adjust the positioning. Figure 4.2 shows the facility used for carrying out an experimental measurement using the PIV technique. The LPLT experimental facility was designed to simulate pressure driven flow in GA's $EM^2$ FPVS system. The facility is constructed of clear acrylic plastic to aid flow visualization techniques. The coolant gas was mixed with smoke particulates in a chamber prior to injection at the inlet. Air was injected at 1 m/s and verified using a hot-wire anemometer. An average 2-D velocity plane was calculated over a period of 3 seconds (3,000 frames). From the 2-D plane, a line velocity profile was used for numerical comparison. The locations of the line profiles are shown in Figure 4.2.

### 4.2.4 Experimental uncertainty

The collected 12-bit depth images were processed by multi-pass, multi-grid, PIV algorithms commonly referred to as PRANA that employs robust phase correlations RPC [68]. A three-step process was applied. The initial interrogation window was a 64 x 64 pixel area, followed by two interrogation areas of 32 x 32 pixels. All passes had a window overlap of 50% . The PIV

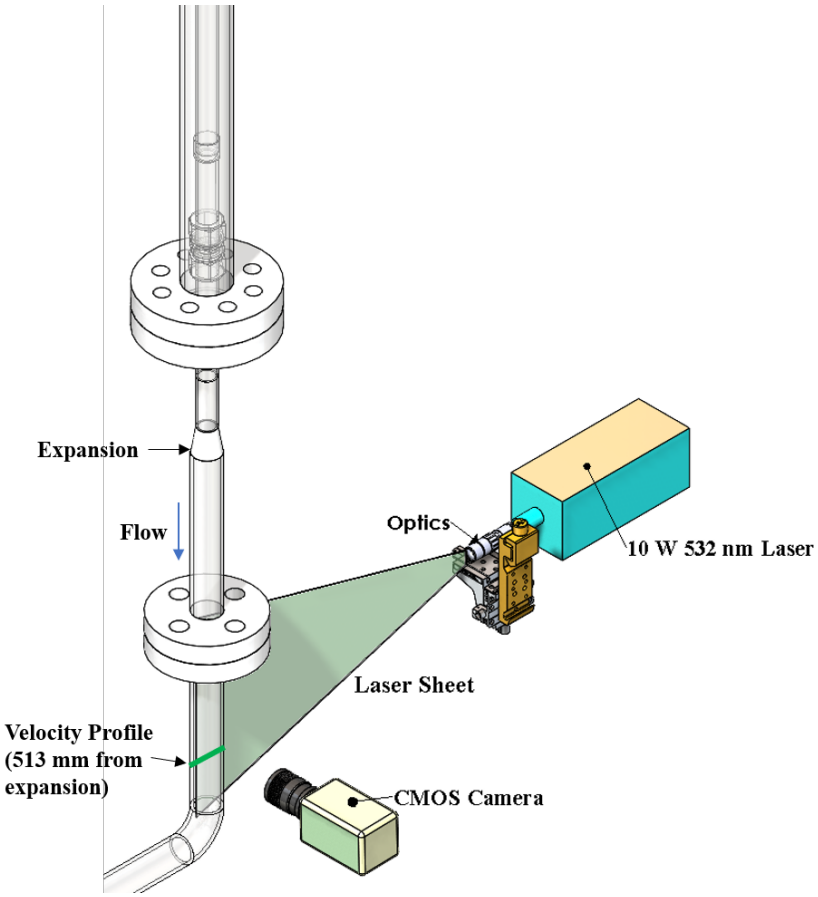


Figure 4.2: Particle image velocimetry (PIV) experimental setup in the LPLT facility, reprinted with permission from [21]

measurement had 50 x 80 instantaneous velocity vectors. Cross-correlations were executed by RPC algorithm, which reduces errors in the presence of high rotational motion compared to standard algorithms [69]. Universal outlier detection approach proposed by Westerweel [70] was applied to determine spurious vectors and replaced via interpolation. The spurious and erroneous vectors for the velocity were evaluated to be less than 1.5%. The study of Timmins [71] estimated the uncertainty of PRANA to be approximately 0.1 pixels. The PIV uncertainty propagation discussed in the reference [72] was estimated for the statistical results and uncertainty associated with the velocity was estimated to be less than 2%, which agrees well with previous literature such as the works of Hyun [73] and Elahi [74].

## 4.3 Validation of the Numerical Model

### 4.3.1 Grid Convergence Test

Grid convergence test was performed with a simplified geometry of gradual expansion flow as illustrated in Figure 4.3. First, The cross-sectional mesh varied from non-uniformly sized 405 to 1,280 cells, with constant axial direction mesh size of 3 mm. On finest mesh, the cell sizes in the vicinity of the wall are $8.414\times10^{-5}$ m and 3.008 $\times10^{-4}$ m for small and large diameter pipe, respectively, which were of the order of $y^+$ for given Reynolds number of 3,591 based on small diameter pipe. The grid independence for this step was established by monitoring the grid convergence index (GCI) suggested by Roache [52], defined as GCI $= F_s\epsilon/(r^p - 1)$ where $F_s$ is safety factor of 1.25, $\epsilon = (f_1 - f_2)/f_1$ is relative error, $r$ is grid ratio and $p$ is order of method. The reattachment length is chosen as $f_1$, $f_2$ and $f_3$ for each mesh, respectively. Grid independence was declared when the GCI ceased to vary by more than 1% (Table 4.1). To establish overall grid independence, the cross-sectional mesh size (number of cells) was maintained constant at 1,280 and applied to the geometry shown in Figure 4.1-(b). The axial height of the mesh size was varied from 2.822 mm to 9.474 mm such that the total number of cells varied from 0.66 million to 2.23 million. The reattachment length downstream of the expansion was calculated, and the results are listed in Table 4.2. The error was defined in relation to the adjacent case with a sparse mesh. With an axial cell height of 3.449 mm or less, the calculated error was reduced within 1%. Accordingly, grid independence was declared with an axial cell height of 3 mm. All simulation runs were performed in this study with an cross-sectional mesh of 1,280 cells and an axial mesh size of 3 mm.

### 4.3.2 Comparison with PIV measurements

A flow visualization experiment was conducted in the LPLT FPVS test facility to validate the numerical model. Air was injected at the inlet without any injection through the porous wall. The bulk velocity at the inlet was measured using a hot-wire anemometer and controlled approximately 1 m/s, corresponding to a Reynolds number of 2,394 downstream of the expansion (equivalent

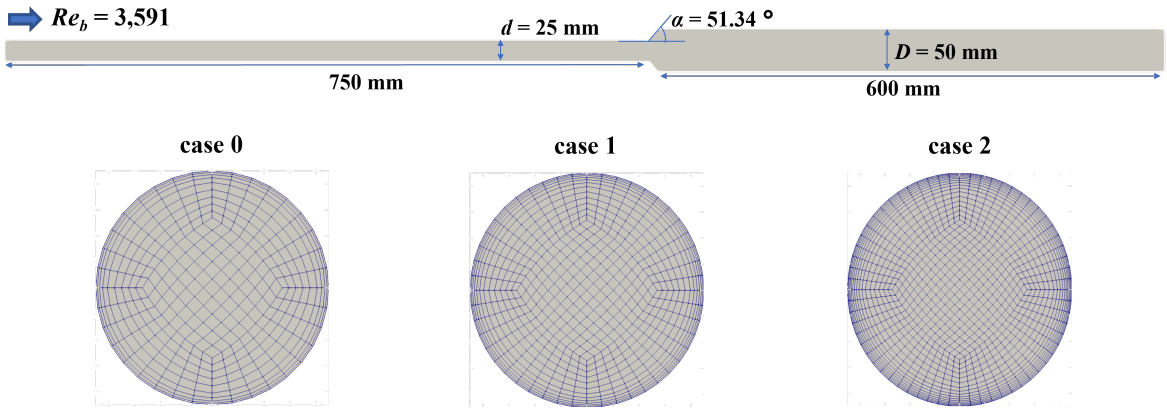


Figure 4.3: Geometry and mesh used for grid independence, adapted with permission from [21]

Table 4.1: Grid convergence index with different cross-sectional mesh, adapted with permission from [21]

| Case | Expansion Ratio | Number of Cells in a Cross-Section | Number of Cells | Reattachment Length [m] | Order of convergence: p | Grid Convergence Index (GCI) |
|---|---|---|---|---|---|---|
| ER1.8_case 0 | 1.8 | 405 | 183,870 | 0.2511 | - | - |
| ER1.8_case 1 | 1.8 | 720 | 326,880 | 0.2843 | 9.1760 | 1.119 % |
| ER1.8_case 2 | 1.8 | 1,280 | 581,120 | 0.2866 | 9.1760 | 0.079 % |
| ER2.0_case 0 | 2.0 | 405 | 183,870 | 0.2769 | - | - |
| ER2.0_case 1 | 2.0 | 720 | 326,880 | 0.3034 | 5.5240 | 2.79 % |
| ER2.0_case 2 | 2.0 | 1,280 | 581,120 | 0.3088 | 5.5240 | 0.56 % |

Table 4.2: Grid independence test with different axial cell heights, adapted with permission from [21]

| Case | Expansion Ratio | Number of Cells in a Cross-Section | Axial Cell Height [mm] | Number of Cells | Reattachment Length [m] | Error [%] |
|---|---|---|---|---|---|---|
| Axial Case 1 | 1.5 | 1,280 | 9.474 | 665,600 | 0.3013 | - |
| Axial Case 2 | 1.5 | 1,280 | 6.350 | 990,720 | 0.3465 | 13.06 |
| Axial Case 3 | 1.5 | 1,280 | 4.233 | 1,486,080 | 0.3316 | 4.51 |
| Axial Case 4 | 1.5 | 1,280 | 3.449 | 1,825,280 | 0.3299 | 0.52 |
| Axial Case 5 | 1.5 | 1,280 | 2.822 | 2,232,320 | 0.3328 | 0.87 |
| Axial Case 6 | 1.5 | 1,280 | 2.300 | 2,736,640 | 0.3299 | 0.84 |

to *Re* of 3,591 based on small pipe diameter). The PIV measurements were made at 0.513 m downstream of the expansion in the "expansion-flow-region" ( see the location in Figure 4.4-(a)). Accurate measurement of turbulence intensity at the inlet was not available, so LES calculations were made with 5, 10, 15, and 20% turbulence intensity values and compared with the PIV measurements. Figure 4.4-(b) shows the axial velocity profiles as function of radial location with both PIV measurements and estimated by LES. Green line with circle mark represents axial velocity profile by the PIV measurement, and straight lines represents the numerical simulation with four LES with different turbulence intensity (5, 10, 15, and 20%) at the inlet. Table 4.3 represents the maximum and bulk velocity and the associated relative percent difference compared to the PIV measurement at the location seen in Figure 4.4-(a). The bulk velocity is calculated by taking the surface integral of the velocity profile and both the PIV measurements and LES calculations yield bulk velocity of 1 m/s, similar to the measurement made by the anemometer at the inlet. The LES result shows axial velocity profiles and its maximum velocity are sensitive to turbulence intensity. Maximum axial velocity from LES result with turbulence intensity of 5% has 92.48% difference compared to PIV measurement while that with turbulence intensity of 20% has 3.06% difference. It is observed that the PIV measurement and LES simulation result with turbulence intensity of 20% are in good agreement. In conclusion, the LES with the WALE model has good agreement with the experimental measurements downstream of "expansion-flow-region" with assumed value of turbulence intensity of 20%.

## 4.4 Results and Discussion

The numerical simulations were conducted for multicomponent gas flow in the LPLT FPVS test facility to study the mixing of air and argon. The primary flow including air and argon with a mass ratio of 9:1 was introduced at the inlet with a velocity of 1 m/s with turbulence intensity of 20% and x-direction artificial disturbance of 0.1% of magnitude of bulk velocity. The secondary high argon concentration flow (7:3 mass ratio) was injected at the porous wall into the loop with a radial velocity of 0.002854 m/s. The Reynolds numbers at the inlet is about 2,400. Note that Reynolds number is based on large pipe diameter and bulk velocity.

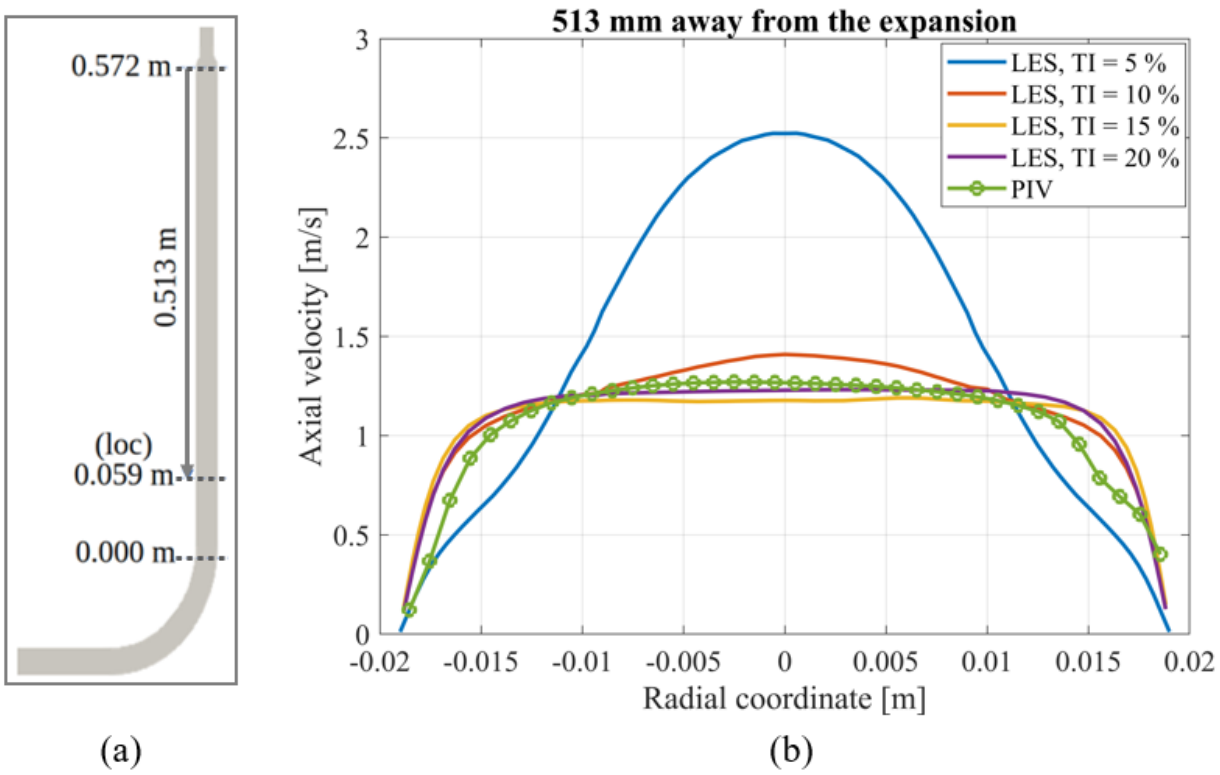


Figure 4.4: Axial velocity profile downstream of the expansion, reprinted with permission from [21]

Table 4.3: Comparison between PIV measurements and LES results, reprinted with permission from [21]

| Location | 0.513 m away from the expansion | | | | |
|---|---|---|---|---|---|
| Method<br>Turbulence Intensity | PIV | LES<br>T =5% | LES<br>TI=10% | LES<br>TI=15% | LES<br>TI=20% |
| Bulk velocity [m/s]<br>Difference [%] | 1.0382±0.0208<br>- | 1.0031<br>3.3804 | 1.0037<br>3.3214 | 1.0017<br>3.5109 | 1.0023<br>3.4605 |
| Max velocity [m/s]<br>Difference [%] | 1.2704±0.0254<br>- | 2.4452<br>92.484 | 1.4091<br>10.919 | 1.1900<br>6.3243 | 1.2315<br>3.0584 |

Flow behavior and component mixing was investigated in the both "expansion-flow region" and "Dean-flow region" numerically. Figure 4.5 shows contour graph of the instantaneous velocity, averaged velocity, average mass fraction of argon, and turbulence kinetic energy (TKE), respectively, in an axial planar view of the “expansion-flow region”, dashed box in the inset of Figure 4.5. On the porous wall of location (1) in Figure 4.5, highly concentrated argon gas introduced through the porous wall formed a high-concentration layer on the rim of the cross section of the pipe. Upstream of the enlarger coupling, at location (2) in Figure 4.5, the concentration gradually decreases and along the wall in the flow direction. Argon diffuses radially, but it is not significant enough to mix them fully. Two different concentration layers were maintained up to the “Expansion-flow-region”. Downstream of the enlarger coupling, at location (3) in Figure 4.5, the flow has two distinct concentric layers and high TKE is observed between the interfaces of the two layers due to recirculation near the corner. The reattachment point is observed at the 0.2877 m downstream of the end of the gradual expansion. Near the reattachment point, at location (4) in Figure 4.5, the stratified two-layer flow becomes unstable. The flow strongly fluctuates and oscillates, referred to as localized turbulence, and thus highest TKE is observed in this region, an order of magnitude higher than that in other regions of the test facility. It may be noted that the TKE in the Figure 4.5-(d) is represented in log-scale. Due to turbulent mixing, it can said that the major part of component mixing is also completed in this region. However, flow distribution is little different compared with component mixing. A pair of secondary vortices, called Dean flow, are generated in the curved region (location 5 in Figure 4.5), making slanted distribution of velocity profile.

Figure 4.6 shows contour graphs of temporally-averaged velocity and turbulence kinetic energy in the Dean-flow region. The U-shaped contour shows the axial planar view of the “Dean-flow region" and the circular contour graphs labeled as (a) to (j) show cross-sectional views at the corresponding location (A) to (J) in Figure 4.6. Each location is 0.1524 m apart through straight pipe and 45$^\circ$ apart in 90$^\circ$ pipe bend region. The top of the circular contour graph is facing toward the inner corner of the loop, and the black arrows in the cross-sectional views represent the

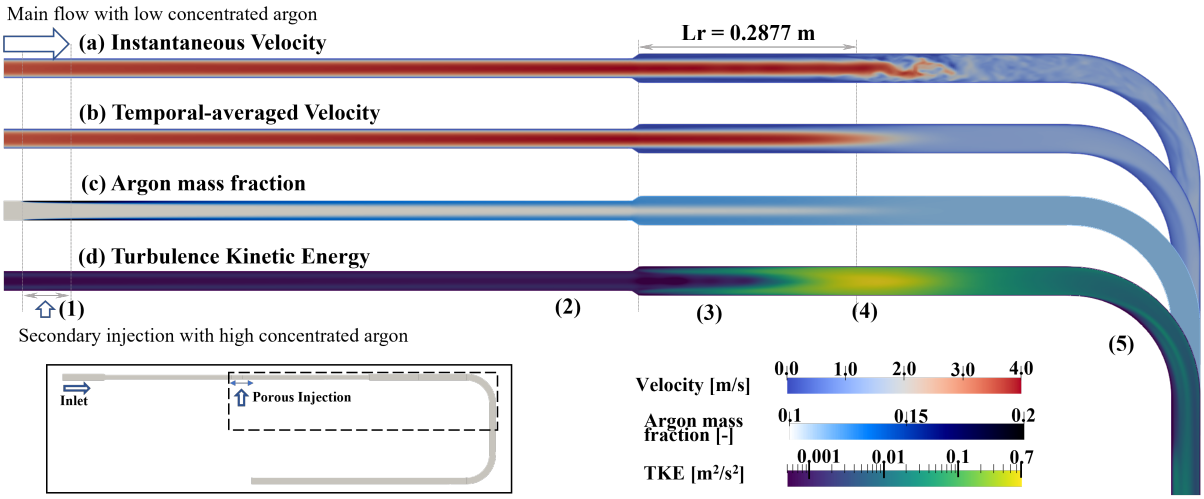


Figure 4.5: Contour graph for two-species simulation (a) instantaneous velocity magnitude, (b) averaged velocity magnitude, (c) averaged argon fraction, and (d) turbulence kinetic energy, reprinted with permission from [21]

direction and magnitude of the secondary flow. A pair of deformed secondary vortices are clearly observed at locations (C) and (G) in Figure 4.6. The secondary flow at the vertical center of the cross-section moves toward the outer wall, resulting in a biased stream-wise flow at outer region of the cross-section. Flow separation and reattachment is not observed in "Dean-flow region" as [63] mentioned that no separation exists for the geometries with CR of 3.0, but there still exists a calm inner region of the cross-section and high values of TKE is observed at the interface of the stagnant region. It seems that it is related to swirl switching.

A series of elbows induces interesting flow behavior. The flow downstream of the first elbow location (E), and (F) has not recovered to the flow profile at location (B), and as the flow passes the second elbow, the axial velocity profiles downstream of the second elbow (locations (I) and (J)) is more biased towards the outward direction than that of downstream of the first elbow. Biased main flow toward outer region of the cross-section requires a longer distance to be recovered to a fully developed flow. It can be concluded that the location at the elbow and downstream of the elbow are not good locations for measuring the velocity, temperature, or concentration.

To quantify the amount of mixing between air and argon through the loop, the concept of

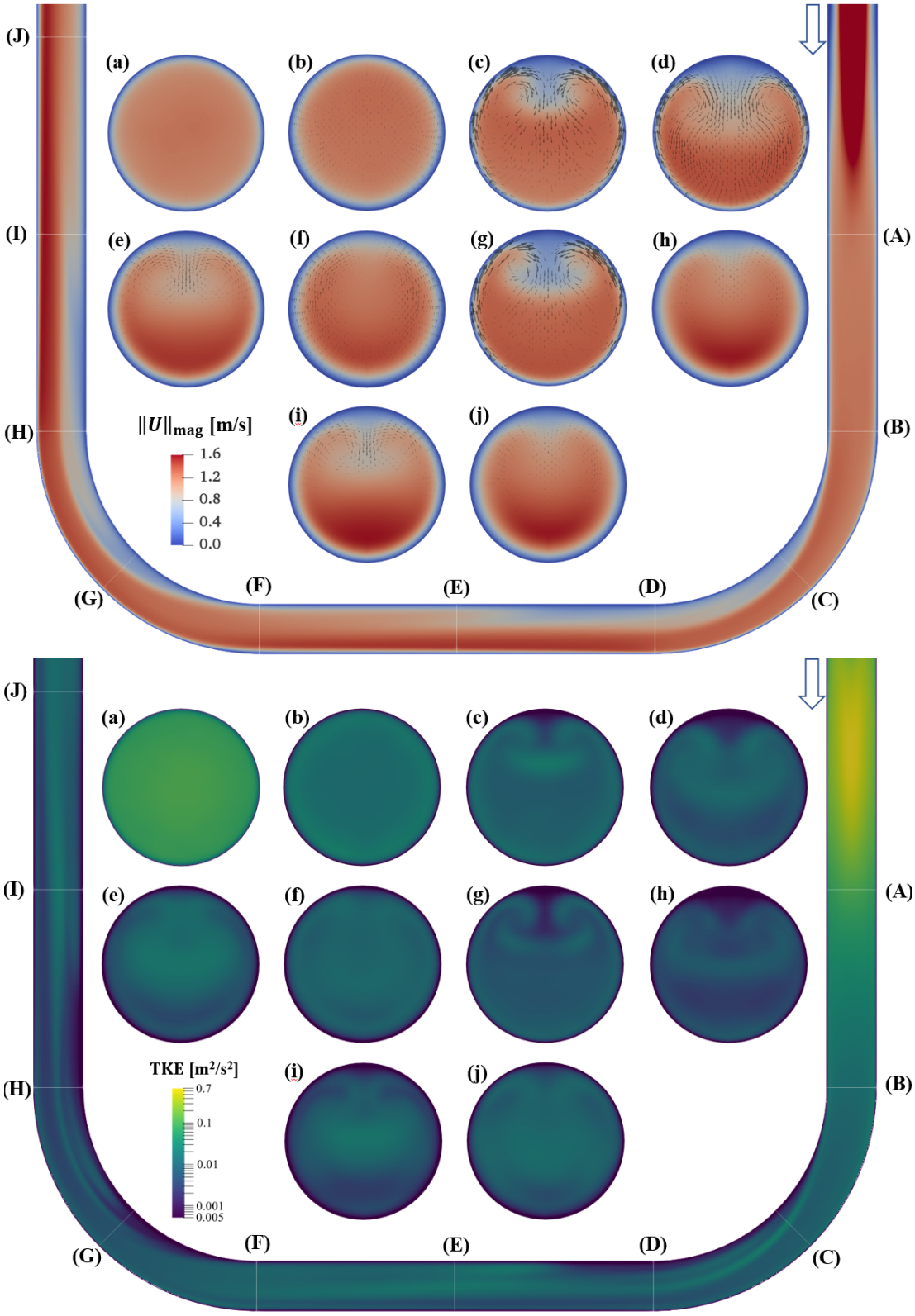


Figure 4.6: Contour graph of temporally-averaged velocity magnitude (top) and turbulent kinetic energy (bottom), respectively in the Dean-flow region, reprinted with permission from [21]

absolute mixing index (AMI) was introduced. The AMI is defined as the Eq.4.5. It is the ratio of the standard deviation of the mass fraction of argon over a cross section to the averaged mass fraction over the cross section. An AMI of 0 indicates that the mixture is homogeneously mixed, while an AMI of 1 indicates that the two components are totally unmixed.

$$\textbf{AMI} = \frac{\sigma_w}{< \overline{w}_i(x,y,z) >} = \frac{\sqrt{\frac{1}{A}\int_A \{\overline{w}_i(x,y,z) - < \overline{w}_i(x,y,z) >\}^2 dA}}{< \overline{w}_i(x,y,z) >} \tag{4.5}$$

where $\overline{w}_i(x,y,z)$ is the temporally averaged mass fraction of surrogate gas *i* at a specific point on the cross section, $\langle \overline{w}_i(x,y,z) \rangle$ is the averaged mass fraction of surrogate gas *i* over the cross section, $\sigma_w$ is the standard deviation of $\overline{w}_i(x,y,z)$ over the the cross section, and A is the cross-sectional area. The value of AMI is monotonically decreasing downstream of the point of injection of the secondary flow. The slope of the AMI in the Figure 4.7 can be interpreted as the mixing rate. The steeper the slope is, the more rapid the mixing is.

Figure 4.7 represents the AMI based on the argon mass fraction along the flow loop for a given operating condition with a Reynolds number of 2,400 and with the injection of secondary gas, and slope of the AMI. Red, blue, yellow and green lines of the graph represent upstream of the expansion, downstream of the expansion, first elbow, and downstream of first elbow, respectively.

At the beginning, a high concentration of argon injected through the porous wall diffuses and mixes along the flow loop. The value of the AMI reaches 0.425 and starts to decrease. The mass fraction distribution has a rim with high concentration of argon, which is not mixed well. Steep slope of the AMI value is observed in the location (a) of Figure 4.7. It looks that advection of radial velocity of the injected surrogating gas at the porous wall is the dominant reason for steep mixing in location (a) of Figure 4.7. As fluid flows, the effect of radial advection is attenuated and slope of the AMI becomes less steep because only naturally generated turbulence eddy near the wall and molecular diffusion is dominant effects of the mixing upstream of the expansion in location (b). During the gradual expansion at location (c), the distribution of the argon mass fraction is stretched out and smoothed as the diameter of the pipe increases. This is the reason for the steep drop in

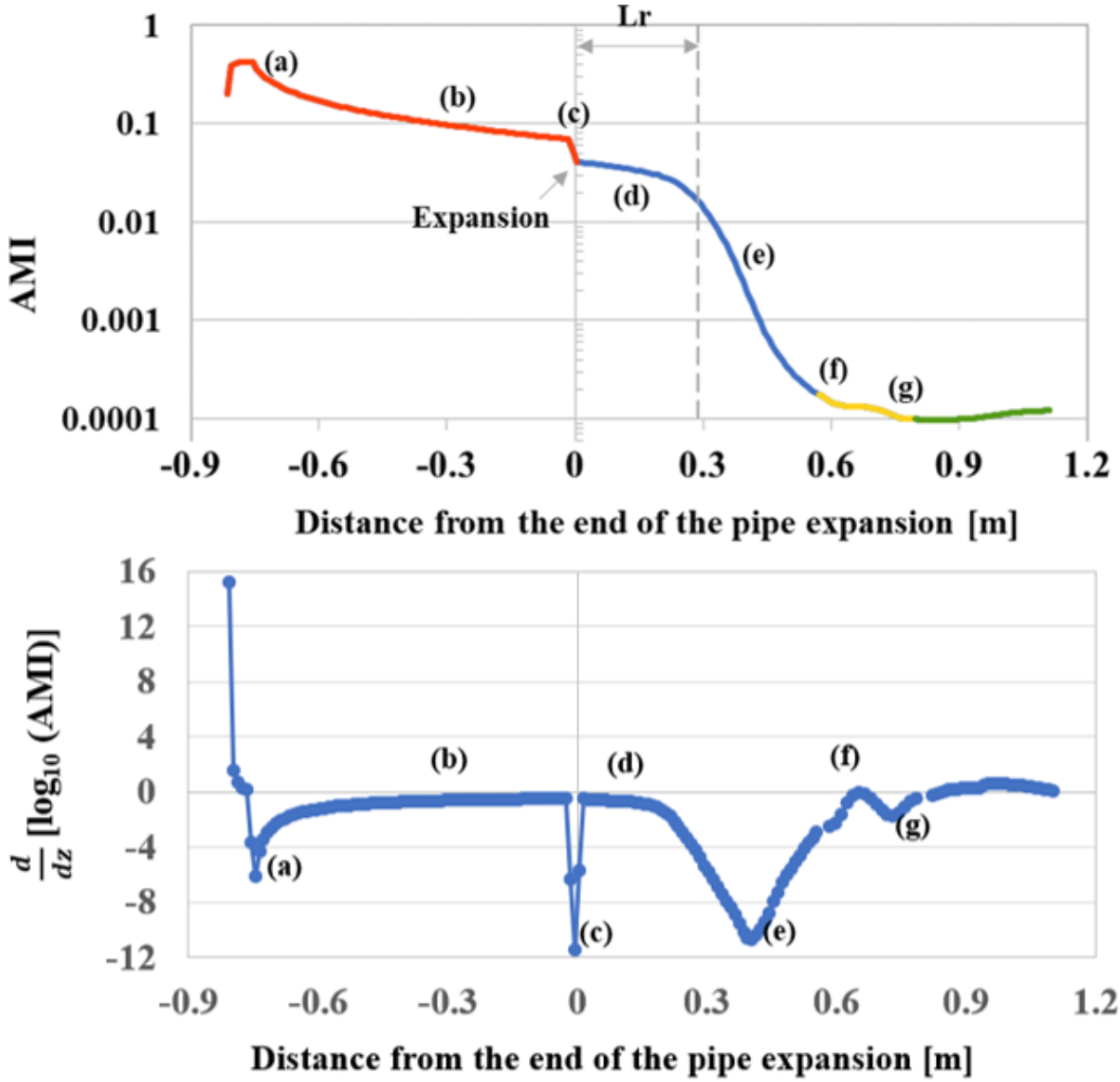


Figure 4.7: AMI based on argon mass fraction along the location of the loop (top) and slope of AMI (bottom), reprinted with permission from [21]

AMI is observed at the expansion. The slope of the AMI downstream of the expansion is as small as that of the slope of the AMI upstream of the expansion. It seems that the recirculation itself does not affect the mixing at location (d). It is supported by the result that the flow looks stratified as recirculation and mainstream flow as depicted in Figure 4.5-(b). The maximum change in the AMI within the loop is located downstream of the expansion near the reattachment point where the localized turbulence occurs at location (e) where the turbulence intensity is order of magnitude higher than that at any other location in the LPLT FPVS. Steepest slope of the AMI is located 0.40 m downstream of the expansion at location (e). Three standard deviation of the mean covers the 99.73% of normal distribution, and thus it is sufficient to state that the flow is well mixed when the AMI of the argon mass fraction is below 0.001. Mixing length is defined as the length between the end of the gradual expansion and the location where the AMI is 0.001 in current study. As mixing length lies between location (d) and (e), we can conclude that mixing is completed within the "expansion-flow region" upstream of "Dean-flow region". The 90 degree elbow in the "Dean-flow region" (location (g)) also have a steep slope of the AMI than that of the diffusion dominant regions like location (b) and (d) but it's magnitude of change is less than the change in "expansion-flow region". Rather, the redistribution of the component concentration is of interest within the elbow due to secondary flow. However, standard deviation (or the AMI) cannot quantify this phenomena. The skewness of the component concentration might be required to quantify the redistribution but it is beyond the scope of the current study.

To check the effect of secondary injection at the porous wall on the mixing process, a sensitivity study was performed for scaled FPVS test facility. The velocity at the inlet was set at 1 m/s and a different secondary flowrate was applied at the porous wall. Figure 4.8 shows reattachment l (blue square) and mixing lengths with the AMI of 0.001 (orange diamond) as a function of the "flowrate ratio". The flow rate ratio is defined as the flowrate at the inlet over that at the porous wall. The trend of the mixing length determined by the AMI is similar to the that of the reattachment length, meaning that flow behavior dominates the mixing of components in this system. Small introduction of the flow at the porous wall affects about 5$\sim$6% on reattachment and mixing lengths.

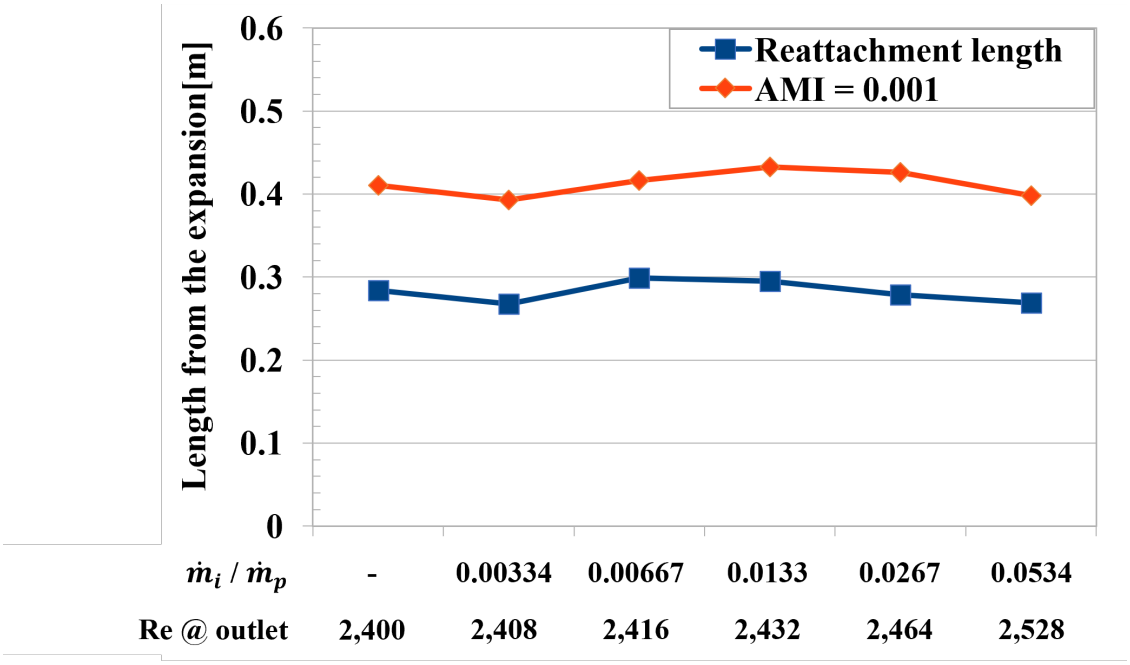


Figure 4.8: Reattachment and mixing lengths with different flowrate at the porous wall. $\dot{m}_i$ and $\dot{m}_p$ are flowrate at the inlet and the porous wall, respectively, reprinted with permission from [21]

Interestingly, the introduction of secondary injection at the porous wall with 0.33% of bulk mass flowrate ($\dot{m}_i$) can reduce reattachment length by 5.9% compared with no injection at the porous wall introduction. In contrast, the introduction of 0.66% bulk mass flowrate at the porous wall can increase the reattachment length by 11.7% compared with 0.33% of bulk mass flowrate at the porous wall. It seems that the change of reattachment length by small secondary injection at the porous wall is related to distortion of velocity profiles and increase of turbulence disturbance due to the introduction of the secondary flow at the porous wall. Further study is necessary for future studies. The decreasing trends in the AMI and reattachment length noticed in Figure 4.8 are attributed to increase in bulk velocity at the axial flow.

## 4.5 Conclusions

The numerical model combined with the solver, *reactingFOAM* and LES WALE model in OpenFOAM v8 is validated to simulate fluid flow through a geometry of gradual expansion pipe by comparing with the PIV measurements [21]. The PIV measurements of velocity profiles down-

stream of the expansion are in reasonable agreement with the LES calculations with appropriate flow disturbance (turbulence intensity of 20% and x-direction artificial disturbance of 0.1% of magnitude of bulk velocity) at the inlet.

Using this validated model, numerical simulations were performed for the LPLT FPVS test facility. The concept of standard deviation of argon mass fraction over cross-section of the pipe (AMI) was used to quantify the mixing of components through out the loop. The mixing rate is defined as the slope of $\log_{10}(\mathsf{AMI})$ and is used to quantify the rate of mixing in the current study. High values of mixing is observed (1) downstream of the porous wall injection, (2) at the gradual expansion joint, (3) downstream of the gradual expansion where localized turbulence is induced, and (4) downstream of the pipe bend. The highest change of $\log_{10}(\mathsf{AMI})$ occurred around the location (e) in Figure 4.7, near the reattachment of gradual expansion. As standard deviation of argon mass fraction become smaller than 0.001, it can be considered that component concentration is fully mixed downstream of the location (e) in Figure 4.7.

However, not all downstream of the location (e) in Figure 4.7 is a good location to measure certain properties. The axisymmetric axial velocity distribution shifted and biased toward outer region of the cross-section at the $90^\circ$ pipe bend, and this biased distribution remains furthur downstream of the pipe bend. A series of the $90^\circ$ elbow enhances biased distribution and elongates the recovery length required for velocity distribution to be fully developed downstream of the pipe bend. It can be a huge problem especially when closed loop is considered. At an elbow and downstream of an elbow is not a good location to measure flow fields or mixing.

Therefore, best location to measure velocity and concentration is the location between downstream of the expansion and upstream of the first elbow, or between location (A) and (B) in Figure 4.6. Parametric study with different injection rates of surrogate fission product gas at the porous Wall shows that the trend of mixing length is similar to the reattachment length. Thus, Figure 3.6 could suggest a specific location between location (A) and (B) in Figure 4.6 to measure concentration and flow rate. However, it should be noted that ER considered in Figure 3.6 is 2.0 while that of FPVS system is 1.5.

Since both x-direction linear disturbance and turbulence intensity are introduced at the inlet, it is hard to directly compare the numerical results with the experimental results. Each factor needs to be separated and studied in the future. In addition, the amount of attenuation for turbulence intensity upstream of the expansion need to be considered for better comparison in the future studies.

In conclusion, the contributions in this chapter are: (1) estimation of the turbulence intensity of the scaled FPVS test facility at inlet by comparing with the result of LES study; (2) introduction of the Absolute Mixing Index (AMI) and it's slope to quantify component mixing and the rate of mixing, respectively; (3) demonstration of relationship between the mixing length and the reattachment length downstream of the expansion; and (4) identification of the best location for measuring velocity and concentration in the LPLT FPVS.

# 5. PARTICLE DEPOSITION IN A CHANNEL FLOW

## 5.1 Introduction

In high temperature gas cooled fast reactors the primary coolant carries graphite particulates from the core and deposits on the walls of the Fission Product Venting System (FPVS). It is estimated that over a period of one year over 10 kgs of particulate matter is transported and/or deposited on the wall of the FPVS and eventually degrading the thermal output of the reactor. this situation could be exacerbating under accidental conditions. So it is important to characterize the particle transport in rectangular channels from both the fundamental physics and application points of view. It has numerous applications such as heating, ventilation, and air conditioning (HVAC) systems; microelectronics manufacturing; inhalation pathways; and general filtration systems. This chapter focuses on the numerical simulation of the particle transport in a rectangular channel and much of the content of this chapter is reported in a paper by Chavez [1] and the author of this dissertation is a coauthor of the paper. The dissertation author was responsible for the numerical modeling while others were responsible for the experimental work. Fischer [75] used graphite dust and helium to simulate the motion of a particle-laden coolant in a gas-cooled reactor. The purpose of scaling gas-cooled reactor conditions for research is to design and develop methods for capturing particles from the flow during both normal operating conditions and depressurization scenario. Thus, numerical simulation and experimental work can be used to gain an understanding of the mechanisms governing particle deposition.

The Eulerian approach to describe the flow of particles assumes that the particles are a continuum that has limitations, particularly when studying deposition. However, several difficulties exist in using the Lagrangian approach for particle simulation. The Lagrangian approach requires the injection and tracking of thousands to millions of particles to obtain a solution that is independent of the number of particles injected. Property gradients within a medium could generate forces on particles, which will impact their trajectories. Lift, drag, and Basset forces impact particle trajec-

tories. The thermophoresis force is observed if there is a temperature gradient. Further, external body forces such as gravitational and electromagnetic forces can influence particle motion. Limited studies have been reported on the simulation of particle motion in non-circular ducts, whereas a considerable number of simulations of particle motion in circular ducts have been reported in the literature. Zhang and Ahmadi [76] performed a particle simulation based on the DNS fluid fields. They considered the drag, Brownian, lift, and gravitational forces. Tian and Ahmadi [77] solved a kind of RSTM to obtain the flow fields and performed a particle simulation using their PARTICEL code, implementing the stochastic continuous filter white-noise model of Thomson [78]. Sharma [79] reported the results of a DNS study of fluid flow and particle tracking in a square channel. In this study, only the influence of the drag and gravity force was considered. Zhang [24] also studied the drag, lift, gravity, and collision forces using the discrete element method for fluid fields in DNS, and found that the gravity force and secondary flow played major roles in the distribution of particles of a specific size. To introduce the effect of turbulence on the averaged velocity profile estimated from the RANS-based equation, Dehbi [80] proposed a state-of-the-art Lagrangian approach combined with a random walk diffusion model to simulate particle transport in a square channel.

Particle deposition in a horizontal circular duct can be interpreted as a competition between gravitational settling and turbulence diffusion. Turbophoresis is another kind of force to be considered in turbulent effect in general. Turbophoresis is induced by the gradient of the fluctuation velocity in this region [81]. Unlike drag and gravity force, no concise force equation for turbophoresis has been proposed. Instead, the random walk model allows for the application of turbulence effect to particles by generating a fluctuating velocity proportional to the square root of the turbulence kinetic energy (TKE). This mechanism becomes statistically reasonable when large number of particles are introduced. Turbulent diffusion and turbophoresis can be treated using a Monte Carlo model such as the descrete random walk (DRW) model or continuous random walk (CRW) model.

A particle simulation model for square channel flow is presented in this chapter. The flow filed

was predicted by using an RSTM model and particle tracking was performed using a Lagrangian approach. The flow condition is specified as $Re_\tau$ of 150, and the corresponding relaxation time is between the diffusion and turbophoresis regions. The geometry considered for this study included a series of three square duct test sections, each with a 3-inch-square cross-section and a 24-in length, for a combined total length of 72 in. The numerical simulation domain was built to match the geometrical dimensions of the experimental facility. The main stream flow field in the channel was solved using the Eulerian approach, while the motion of the particles was tracked in a Lagrangian framework. It was assumed that a well-mixed air-particle mixture at a constant temperature was injected into a horizontal channel. Various turbulence models in discussed in Chapter 2 were considered and it was found that the RSTM was best suited for flow simulation considering the computational cost in a square channel. However, the LES is known to perform better than RSTM which incurs higher computational cost. As a compromise between accuracy and the computational cost, the RSTM model was then used to study turbulent flow in a square channel. The gravity, drag, and turbulence effects were considered in the simulation. The turbulence effect was expressed as a random walk model built in OpenFOAM v7. The simulation results reported here were validated by comparing them with the experimental data in the associated literature [82], as well as with our own measurements [1] or the experimental measurements of Barth [83] as a function of deposition velocity.

## 5.2 Background knowledge for particle deposition

### 5.2.1 Lagrangian particle approach

The motion of particles is governed by the Newton's second law of motion:

$$m\frac{dU_p}{dt} = \Sigma F_i \tag{5.1}$$

The forces governing particle motion in a square duct include the gravitational force and turbulent diffusion, which is also called turbophoresis. In addition, secondary vortices, which are not observed in circular ducts, are generated at the corners of a square duct and could affect the

trajectories of particles. The drag force cannot be neglected because it not only attenuates particle settlement due to gravity, but also moves particles along the secondary vortices. The lift and Basset forces were neglected in this study. Brownian motion was not considered because the minimum size of particles studied in the current case is 1 $\mu$m, limited to the effect of particle motion. Moreover, no other gradient-induced forces such as thermophoresis, were considered in this study. Therefore, this study considers three types of forces: drag force, gravitational force, and turbophoresis. The drag force term is expressed below. It should be noted that the drag force is exerted not only in the stream-wise direction, but also in the cross-stream direction.

$$F_d = \frac{1}{8} C_D \pi d_p^2 \rho_f \left| U_f - U_p \right| \tag{5.2}$$

where $C_D = 24 Re_p^{-1}(1 + 0.15 Re_p^{0.687})$ is Schiller-Naumann drag correlations; $\rho_f$ is fluid density; $U_f$ and $U_p$ is fluid and particle velocities, respectively; $d_p$ is particle dimater; and $Re_p = d_p \left| U_f - U_p \right| / \nu_f$ is the particle Reynolds number.

The gravity force is a tpye of body force inducing a buoyancy force. Thus, this force is expressed as the difference between the gravity force and following buoyancy force.

$$F_G = m_p(1 - \rho_f/\rho_p)g \tag{5.3}$$

where $m_p$ is the particle mass; $\rho_f$ and $\rho_p$ are the fluid and particle densities, respectively; and $g$ is gravitational acceleration.

A thermodynamic property gradient generates a force on a particle in the direction opposite to the gradient. For example, if particles lay in a non-uniform temperature field, they are subjected to a force called thermophoresis in the negative direction of the temperature gradient. A gradient in the fluctuating velocities gives rise to a force called turbophoresis, which is critical near the wall due to inhomogeneity of the turbulent flow in a channel flow. This force is applied using a different method compared to the drag and gravitational forces. Instead of adding the force term, the fluid velocity used in this type of particle force is updated to the actual velocity by adding the fluctuation

velocity to the average velocity.

$$U_f = \bar{U}_f + u \tag{5.4}$$

where $U_f$ is the actual velocity, $\bar{U}_f$ is the average fluid velocity, $u$ is the fluctuation velocity due to turbulence. If the turbulence kinetic energy is assumed to be isotropic, the fluctuating velocity can be estimated from the following Discrete Random Walk (DRW) model:

$$u_{turb} = \sqrt{2k/3}(2\mathbb{R}) \tag{5.5}$$

where $k$ is the TKE and $\mathbb{R}$ is the random function ranged between -0.5 and 0.5.

The turbulence is anisotropic in the channel flow, in which the Reynols stress in the secondary direction is less than that in the primary direction. If the DRW model (5.5) is employed for a channel flow, the turbulent effects might be overestimated. To make it accurate, a damping function for the turbulence kinetic energy can be introduced to reduce its effect near the wall. Another method is to employ a Reynolds stress model that calculates each component of the Reynolds stress. Without the isotropic assumption, the fluctuation velocity can be directly estimated from the corresponding components of Reynolds stress.

This mechanism becomes statistically reasonable when a large number of particles are introduced and tracked. The particle penetration efficiency or deposition rate in a duct can be numerically estimated by counting the number of particles deposited on each wall.

### 5.2.2 Stokes number

The Stokes number is defined as a ratio of the characteristics time off a particle to the characteristic time of the flow. The Stokes number was considered to ensure the particle in the flow followed streamlines closely. Particles follow the flow's streamline if Stokes number is small, whereas particles maintain their moving direction if Stokes number is larges. This non-dimensionless value is expressed as below.

$$Stk = \frac{\tau_p}{\tau_f} = \frac{\rho_p d_p^2 C_c}{18\mu} \frac{U_b}{W} \tag{5.6}$$

where $\tau_p$ is the characteristic time of particle, $\tau_f$ is the characteristic time of flow, $d_p$ is the diameter of particle, $\rho_p$ is the density of particle, $\mu_f$ is the dynamic viscosity of fluid, $U_b$ is the fluid bulk velocity, W is the width of the square duct, and $C_c$ is the Cunningham correction factor.

When the particle diameter is the same order as the mean free path of the medium fluid, the resisting force offered by the fluid is smaller than that predicted by Stokes law. To compensate this non-continuum effect, the Cunningham correction factor was introduced into Stokes law and expressed as

$$C_c = 1 + \frac{2\lambda_{mfp}}{d_p}\left[1.257 + 0.4\exp(-1.1 d_p/(2\lambda_{mfp})\right] \tag{5.7}$$

where $\lambda_{mfp}$ is the mean free path of the suspending fluid and $d_p$ is the particle's diamter

### 5.2.3 Deposition velocity

This study examined two methods to determine the particle deposition velocity. The quantification of particle deposition in a channel flow is traditionally presented in the form of non-dimensionless deposition velocity, which is given as follow:

$$u_d^+ = \frac{J}{C_0 u_\tau^*} \tag{5.8}$$

where $J$ is the particle flux at the wall, $C_0$ is the particle concentration near the wall, and $u_\tau^*$ is flow shear velocity. Superscript * refers to the average along the perimeter.

In the computational simulation using Lagrangian approach, the definition of the deposition velocity (Eq. 5.8) should be modified to fit the numerical calculation. For the second method, the particle deposition velocity by Ahmadi ([76, 77, 84, 85]) group is given as follows:

$$u_d^+ = \frac{N_d/t_d^+}{N_0/y_0^+} \tag{5.9}$$

where $N_d$ is the number of deposited particles in the time duration $t_d$, which should be selected in the quasi-equilibrium of $N_d/t_d$; $N_0$ is the initial number of particles uniformly distributed in a region within a distance $y_0^+$ from the wall; $y_0^+ = y_0 u_\tau^*/\nu$; and $t_d^+ = t_d(u_\tau^*)^2/\nu$;

This method is named as Method A in the current study and the obtained results are presented in Figure 5.1-(up).

The second method for measuring the deposition velocity was proposed in this study. Calculating the correct concentration and flux using the Lagrangian approach is not easy because numerous particle simulations are required to fulfill the statistical significance. In the region where the gravitational force is dominant, the concept of the deposition velocity can be interpreted as the terminal velocity, meaning a constant vertical velocity in the the bottom wall as the drag force becomes equal to the gravity force and the particle settles down. The average velocity of vertical direction for each particle can be estimated using the Lagrangian approach, and the mean of the average velocity can be considered to be the deposition velocity as follows:

$$u_d^+ = \frac{1}{N u_\tau^*} \sum_{i=1}^{N} (\Delta y_i / \Delta t_i) \tag{5.10}$$

where $N$ is the number of particles within the channel domain, $u_\tau^*$ is friction velocity, and $\Delta y_i$ is the displacement of a particles in gravity direction in the time interval $\Delta t_i$ .

This method to measure the deposition velocity is named as Method B in the current study and the corresponding results are presented in Figure 5.1-(down).

### 5.2.4 Wood correlation

A semi-empirical correlation to estimate normalized deposition velocity $u_d^+$ as a function of normalized relaxation time $\tau^+$, comprised of three terms with physical meanings, was proposed by Wood [82] and given as follows:

$$u_d^+ = 0.057\, Sc^{-2/3} + 4.5 \times 10^{-4} (\tau^+)^2 + \tau^+ g^+ \tag{5.11}$$

where $Sc$ is the Schmidt number, $\tau^+$ is the normalized relaxation time and $g^+$ is the normalized gravitational acceleration. The first term in the above equation is related to Brownian motion and eddy diffusion, as derived by [86], and is dominant when the non-dimensionless relaxation time is

low. The magnitude of the diffusivity can be enhanced by the turbulence viscosity. The Schmidt number is defined as the ratio of kinematic viscosity $\nu$ to particle mass diffusivity $D$, which can be estimated by the following Einstein relation:

$$D = \frac{k_b T}{3\pi\mu d_p} C_c \tag{5.12}$$

where $k_b$ is the Boltzmann constant of $1.38 \times 10^{-23}$ $[m^2 kg/s^2 K]$, $T$ is the temperature, $\mu$ is the dynamic viscosity of the fluid, $d_p$ is the particle diameter, and $C_c$ is the Cunningham correction factor.

The second term is related to eddy diffusion-impaction as suggested by Wood [82], and is dominant at a medium relaxation time in a vertical channel, where the gravitational effect does not exist. The normalized relaxation time $\tau^+$ is expressed as follow:

$$\tau^+ = \tau_p \frac{(u_\tau^*)^2}{\nu} = \frac{(\rho_p/\rho_f) {d_p}^2 (u_\tau^*)^2}{18\nu^2} C_c \tag{5.13}$$

where $\rho_p$ and $\rho_f$ are the particle and fluid density, respectively, $d_p$ is the particle diameter, $u_\tau^*$ is the shear velocity, $\nu$ is the kinematic viscosity of the fluid and $C_c$ is the Cunningham correction factor.

The third term accounts for the effect of gravitational settling in the channel, which is more dominant than eddy diffusion-impaction at a medium relaxation time. It is an essential third term in a horizontal channel and is expressed as follows:

$$\tau^+ g^+ = \tau^+ \frac{\nu}{(u_\tau^*)^3} g \tag{5.14}$$

### 5.3 Numerical simulation setting

Particle simulation with lagrangian approach was conducted using OpenFOAM v7. The simulation domain was built on the geometrical dimensions of a square channel, which is comprised of 3-inch-square cross-section and length of $8\pi h$, where $h$ is the half height of a channel. The simulation grid was generated by *blockMesh*, which is a built-in program in OpenFOAM. The grid

spacing along the stream-wise direction (x axis) was constant, except near the entrance, while the cross-stream (y axis) and span-wise directions (z axis) had uniform grids, fulfilling the grid size independence test. After performing GCI analysis using centerline velosity, a 101 $\times$ 101 uniform mesh in the cross-section and 101 mesh along streamwise was determined to be acceptable.

The built-in *simpleFoam* solver was used to solve the SSG turbulence model. Velocity and TKE field within the channel is solved under cyclic boundary condition as discussed in Chapter 2. After that, particle simulation was performed under steady state flow fields using the built-in solver *icoUncoupledKinematicParcelFoam* to solve the trajectory of particles with the Lagrangian approach. The drag force, gravitational force, and stochastic dispersion options (*stochasticDispersionRNS*) were adopted. The transport and depositions of particles within the duct were monitored to determine how many particles stuck to the wall, enabling a quantified evaluation of the particle deposition, including the deposition velocity and penetration efficiency. One hundred thousand (100,000) particles were randomly injected at the inlet surface of the duct. Particles are assumed to stick to the wall when their trajectories intersect with the wall and a particle passes through the outlet move back to inlet maintaining its velocity and cross-sectional location. The fluid is assumed to be air at room temperature. The density of particles is specified as 42 $kg/m^3$, and diameter of particles are ranged from 10$\sim$50 $\mu m$, which are identical to those used in the experimental validation [1].

The minimum number of particles to be tracked to ensure that the penetration efficiency was independent of the number of particles tracked is investigated. A series of tests were conducted by tracking 100,000 particles and it was concluded that more than 10,000 particles had to be injected and tracked to establish that the penetration efficiency to be independent of the number of particles tracked.

## 5.4 Results and Discussion

### 5.4.1 Particle deposition velocity

The particle deposition velocity estimated using Eq.5.9 (method A) is presented in Figure 5.1-(down). The deposition velocity had an order of magnitude of $10^{-2}$ and did not change significantly as the relaxation time varied (see colored markers in Figure 5.1). Tian and Ahmadi [77] carried out a similar particle numerical simulation using the LLR model [16] in a two-dimensional channel, and argued that a specialized wall function was required to fit the Wood correlation [82]. Otherwise, the particle deposition velocity remained constant as the relaxation time varies. Mofakham and Ahmadi [84] explained that the Reynolds stress near the wall resulted in a particle concentration of up to 30 times that of the initial concentration, leading to a fit with the Wood correlation. It should be noted that the previously mentioned studies could not be directly compared to the current simulation. This was because these studies utilized two-dimensional simulations for the fully developed profiles of the particle concentration, while the current simulation was carried out for three-dimensional developing flow regimes with the velocity profiles, TKE and particle concentration. This could explain the different results for the particle deposition velocity computed using Eqs. 5.10 and 5.9. For a fully developed flow, it is known that there is a peak in the turbulence kinetic energy profile near the wall, where particles can be trapped [84]. However, such a region is not present in a developing flow channel, leading to a low concentration and high deposition velocity. This was confirmed in the current study, which was carried out in the developing flow region, and the turbulent kinetic energy profile did not show a clear peak. In fact, the computed particle concentration profile along the wall in the normal $y$-direction shown in Figure 5.2 indicates that no dominant peak occurred in the vicinity of the wall. The term $C_0$ is the initial averaged particle concentration in the channel.

On the contrary, measurements of the deposition velocity using Eq. 5.10 (method B) resulted in a different trend, as seen in Figure 5.1-(down), compared to those based on Eq. 5.9 (method A), in which plots of the normalized deposition velocity are shown as a function of the normalized

relaxation time in a horizontal channel. The bold colored and dashed lines represent mean values estimated using Wood correlation [82] in a Reynolds number range of $3{,}000$-$7{,}000$ in increments of 1,000, while the colored dots represent values found using the current simulation. The black hollow dots represent the experimental data of Chavez [1]. The narrow black lines represent the portions of each term in the Wood correlation [82]. There are two distinct regions in the plot of the non-dimensional particle deposition velocity as a function of the non-dimensional relaxation time in Figure 5.1-(up). In a region where the non-dimensional relaxation time ($\tau^+$) is greater than $10^{-3}$ the simulated values of deposition velocity agrees well with the Wood correlation [82] and the experimental data of Chavez and Barth [1, 83]. Similar to the current study, Barth [83] varied the particle diameter by maintaining the friction velocity constant at 0.08 in their experiment. Chavez [1] varied the fluid velocity instead of varying the particle diameter. The average particle diameter was held constant at 32 $\mu$m. The Wood correlation [82] has gravitational, turbulence eddy, and diffusion terms. The gravitational effects increased with the relaxation time. In the region of $\tau^+ > 10^{-3}$, the gravitational term was dominant and had the most influence on particle deposition. This observation is also consistent with flow physics because the relaxation time is the time required for a particle to adjust to a change in the velocity field. Particles with large relaxation times are more affected by an external force. In this case, the gravitational force resulted in greater particle deposition. In the lower relaxation time region, the gravitational term had less impact on the particle deposition. In the low relaxation time region ($\tau^+ < 10^{-3}$) the non-dimensional deposition velocity increased with a decrease in the relaxation time. In this region, the diffusion term in the Wood correlation [82] was dominant. The particle and turbulence diffusivity increased as the relaxation time decreased because particles were quick to react to changes in the velocity fields, which increased the possibility of particle deposition. In addition, the square cross section channel had secondary vortices at the corners, thus increasing the further possibility of particle deposition at the walls.

In the comparison of the two methods for calculating the particle deposition velocity using Eqs. 5.10 and 5.9, the main difference was the spatial locations of the particles considered in the

calculations. Eq. 5.10 can be interpreted as the overall deposition velocity in the channel while Eq. 5.9 can be understood to be the local deposition velocity near the wall. If the flow had reached the fully developed region, then the particle deposition velocity estimated by Eq. 5.10 will be equal to that estimated by Eq. 5.9.

The Lagrangian particle tracking method could also be used to calculate the deposition distribution at the wall. Figure 5.3 shows the positions of the particles deposited on each wall (bottom, left, top and right surface walls) when 100,000 particles were injected into the channel (left-hand side of the graph), with a particle size of 40 $\mu$m. The Reynolds number based on the average velocity is approximately 6,000. Most of the particles were deposited on the bottom surface, implying that gravity settling (gravitational term) was the most dominant in this $\tau^+$ range ($\tau^+ > 10^{-3}$). However, in this region, the turbulence effects also impacted the particles. Although some particles were deposited on the left and right walls, most of the particles were deposited on the bottom wall. If simulations were conducted without considering the turbophoresis force, all of the particles would be deposited on the bottom wall. The turbulence deposition was estimated to be the result of a combination of turbophoresis and the secondary drag force. Particles were trapped in the secondary vortices generated at channel corners, increasing the probability that particles would remain in the proximity of the wall. The turbulence effects and secondary vortices increased the particle deposition velocity. This explains the deposition patterns observed at the bottom wall.

### 5.4.2 Penetration efficiency

The penetration efficiency ($P$) is defined as the ratio of the number of particles leaving the channel to the number of particles injected into the channel at its entrance. Figure 5.4 shows the variation in the penetration efficiency ($P$) with the Reynolds number ($Re$) and Stokes number ($Stk$). It can be seen in Figure 5.4-(a) that for a given Reynolds number, the penetration efficiency decreases with an increase in the Stokes number. This behavior is expected because the Stokes number is the ratio of the particle relaxation time to the fluid characteristic time. Thus, with a higher Stokes number, there is a higher tendency for particles to not adhere to the flow streamline, and this is proportional to the square of the particle size. The penetration efficiency decreases

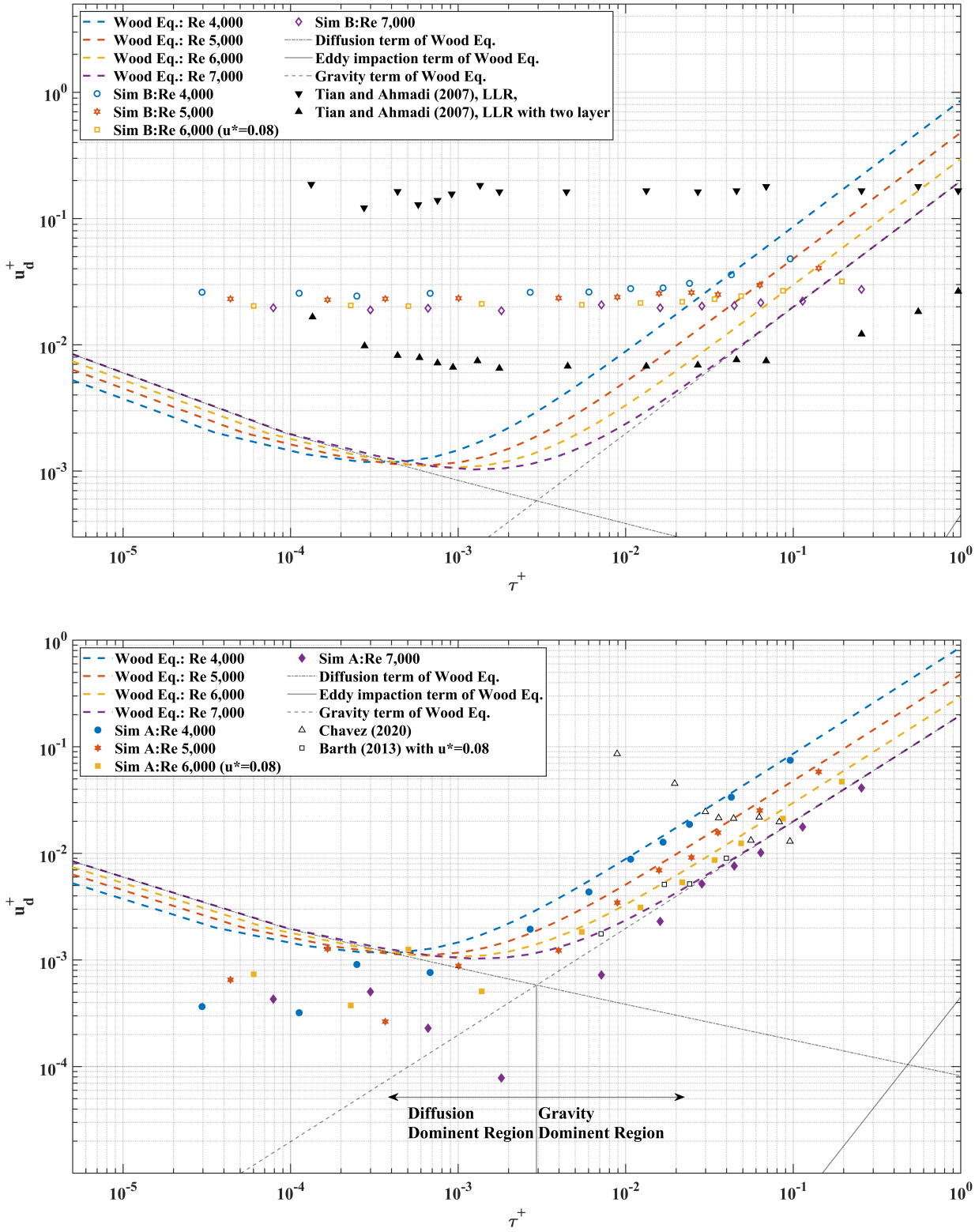


Figure 5.1: Graph of normalized deposition velocity as a function normalized relaxation time using the method A (up, Eq. 5.9) and the method B (down, Eq. 5.10), adapted with permission of [87]

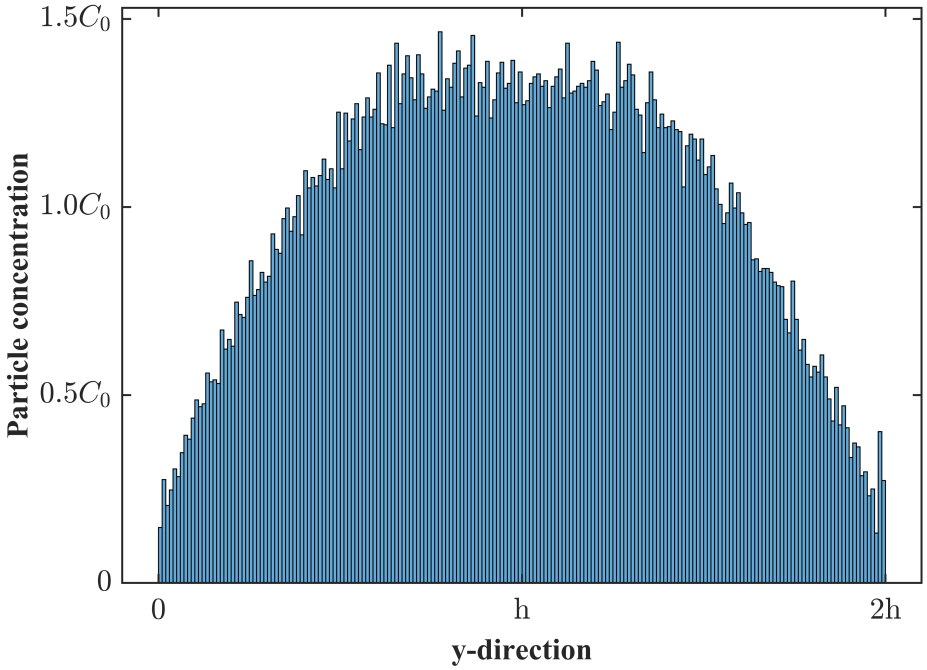


Figure 5.2: Particle concentration as a function of y-direction

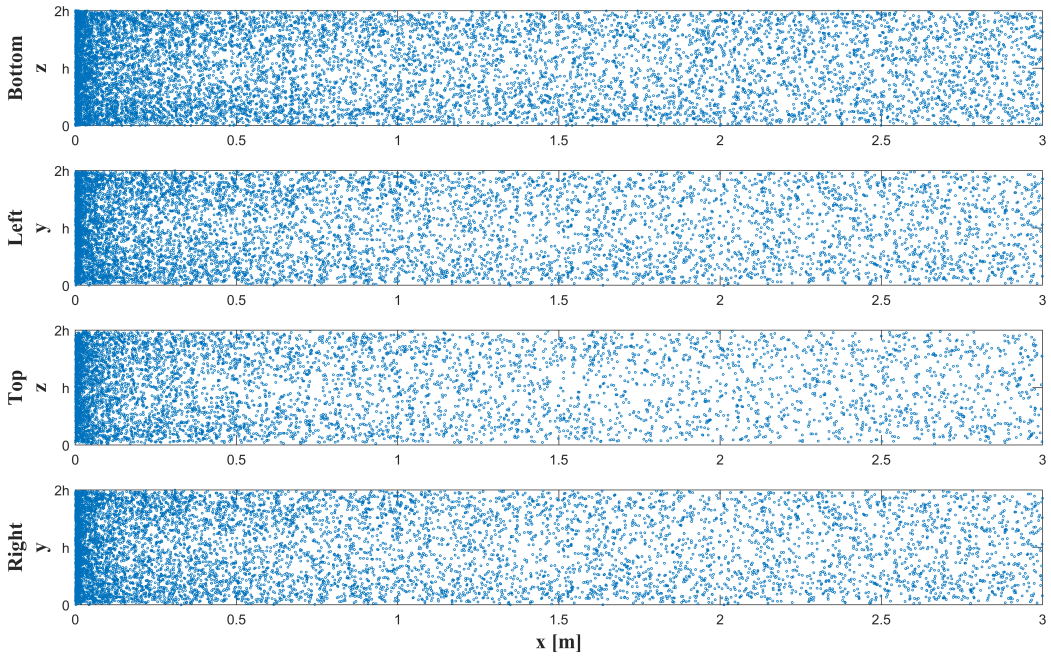


Figure 5.3: Location of particle deposited on each wall

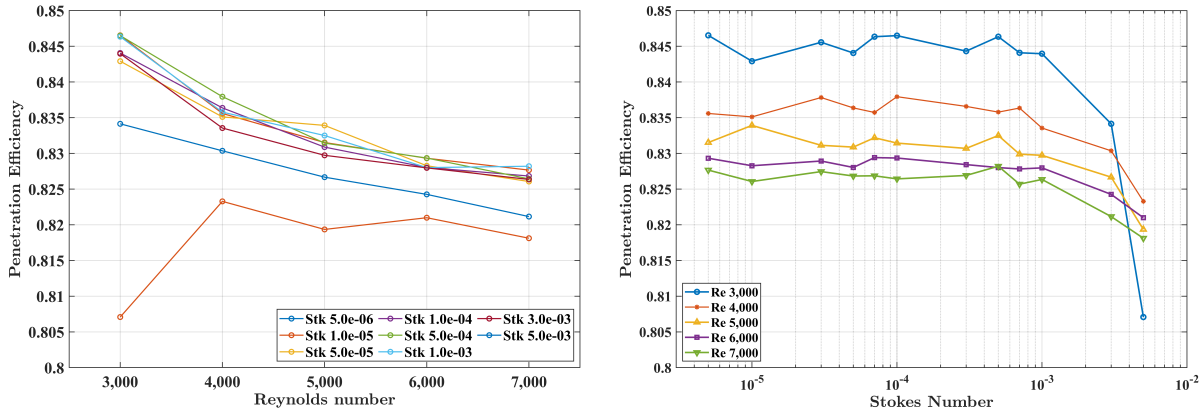


Figure 5.4: (a) Variations of penetration efficiency as a function of Reynolds number $Re$ for different Stokes numbers $Stk$. (b) Variations of penetration efficiency as a function of Stokes number $Stk$ for different Reynolds numbers $Re$.

with an increase in the Reynolds number for a fixed Stokes number because of the increase in particle deposition due to the increase in the turbulence effects with an increase in the Reynolds number. The same behavior is observed in Figure 5.4-(b), where the penetration efficiency is plotted against the Reynolds number for different Stokes numbers. However, at low Reynolds numbers (≈3,000) the penetration efficiency rapidly decreases at high Stokes numbers ($Stk > 3\times10^{-3}$). If the calculations were to be extended for $Stk > 10^{-2}$, one would expect the penetration efficiency curves for different Reynolds numbers to cross because of the competing gravitational and turbulent forces.

### 5.4.3 Continuous Random Walk (CRW) Model

A preliminary particle simulations with CRW model were performed. Instead of the DRW model (Eq. 5.5), the CRW model was employed to reproduce the fluctuation velocity as expressed below. Based on the model proposed by Dehbi [88], a Langevin equation is modified to fit our geometry. Each term in the right-hand side represents the effect of the previous time step, random generation, and the mean drift correction term, respectively.

$$d(\frac{u_1}{\sigma_1}) = -(\frac{u_1}{\sigma_1})\frac{dt}{\tau_1} + \sqrt{\frac{2}{\tau_1}}d\xi_1 + [\frac{\partial(\overline{u_1u_2}/\sigma_1)}{\partial x_2}\frac{dt}{1+Stk} + \frac{\partial(\overline{u_1u_3}/\sigma_1)}{\partial x_2}\frac{dt}{1+Stk}] \tag{5.15}$$

$$d(\frac{u_2}{\sigma_2}) = -(\frac{u_2}{\sigma_2})\frac{dt}{\tau_2} + \sqrt{\frac{2}{\tau_2}}d\xi_2 + \frac{\partial(\overline{u_2u_2}/\sigma_2)}{\partial x_2}\frac{dt}{1+Stk} \tag{5.16}$$

$$d(\frac{u_3}{\sigma_3}) = -(\frac{u_3}{\sigma_3})\frac{dt}{\tau_3} + \sqrt{\frac{2}{\tau_3}}d\xi_3 + \frac{\partial(\overline{u_3u_3}/\sigma_3)}{\partial x_3}\frac{dt}{1+Stk} \tag{5.17}$$

where $u$ is fluctuation velocity; $\sigma$ is rms of velocity; $\overline{u_iu_j}$ is Reynolds stress; $Stk$ is Stokes number; $\tau$ is Lagrangian time scale; $dt$ is time step; $d\xi$ is a series of uncorrelated Gaussian random numbers with zero mean and variance $dt$; and subscripts 1,2 and 3 are streamwise, wall-normal and spanwise directions respectively.

Figure 5.5-(a) and (b) represent particle distributions on cross-sections of horizontal rectangular channels estimated by DNS [79] and the current CRW model. Contour of 5.5-(b) represents TKE, in which red is high values and blue is low. Both results shows high particle concentrations on the mid-point of each edge where high TKE is observed. Figure 5.5-(c) presents the particle concentration profile over the dashed line in Figure 5.5-(b). Here, $C_0$ is averaged particle concentration at the injection. Compared to the DNS study [79], the particle distribution obtained from the CRW model (Figure 5.5-(c)) is estimated better than that from the DRW model (Figure 5.2). Particles concentration at the mid point of the wall is 5-6 times higher than initial particle concentration injected.

## 5.5 Conclusion

In this study, Particle tracking simulation was performed using the Lagrangian approach for a horizontal square channel. The RSTM SSG model [17] was selected to simulate fluid flow. In the current study particle deposition velocity was numerically predicted and compared with the Wood correlation [82] and with the result of experimental measurements [1, 83]. The deposition velocity evaluated using the newly proposed Method B (Eq. 5.10) in the current study had good agreement in the gravity-dominant region, where the relaxation time $\tau^+$ was large ($\tau^+ > 10^{-3}$); however,

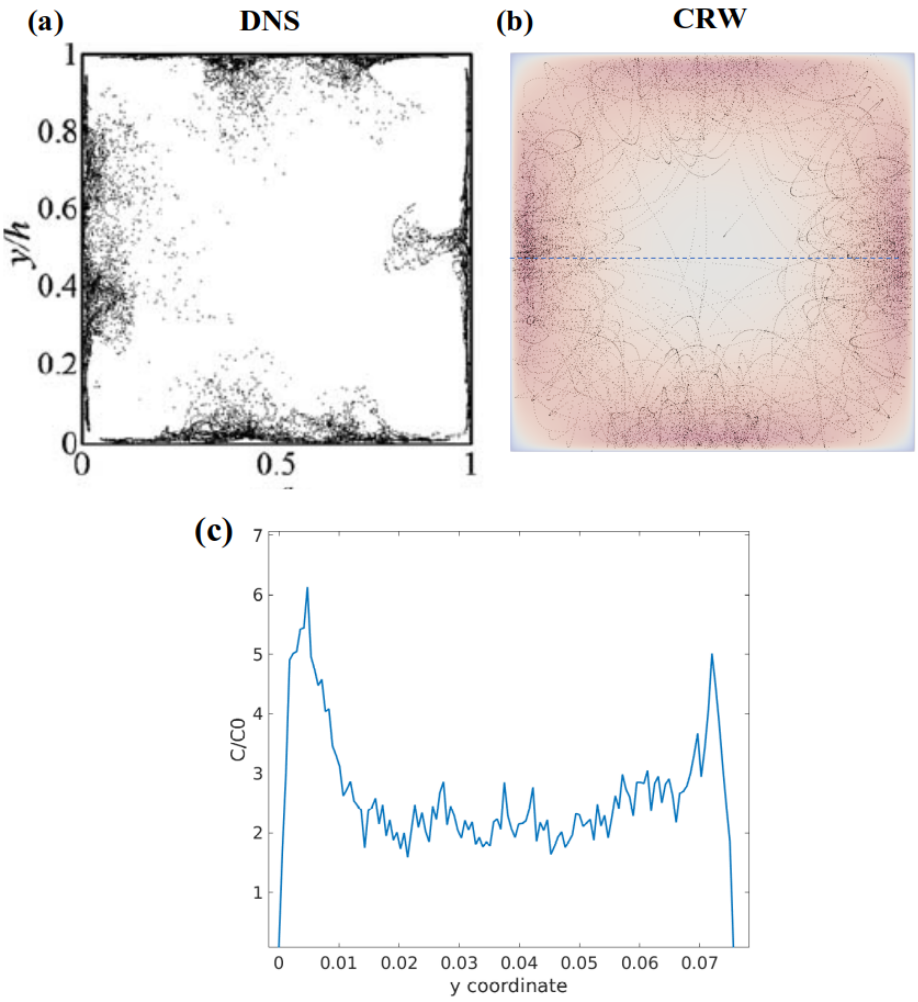


Figure 5.5: (a) Particle distribution obtained from DNS. Reprinted with permission from [79], (b) Particle distribution obtained from current CRW model, and (c) Particle concentration profiles estimated by CRW model

the results estimated at low relaxation times were not in good agreement with the experimental results. On the contrary, the deposition velocity obtained using Method A (Eq. 5.9) were higher than the experimental values, having a nearly constant value in the region below $\tau^+ < 10^{-1}$. Similar trends can be observed in other numerical simulation [77]. One possible explanation is that the high particle concentration near the walls was not represented clearly using the model. The penetration efficiency was found to decrease with an increase in the Reynolds number for a fixed Stokes number in the range of parameters considered in this study ($10^{-5} < Stk < 3 \times 10^{-3}$).

The DRW model assumed isotropic turbulence flows but turbulent flow through a pipe is known to be anisotropic. The CRW model was able to consider anisotropic turbulence flow. Preliminary simulations with the CRW model were able to reproduce particle distributions similar to those obtained from a DNS study [79]. Thus, the CRW model is recommended for further particle deposition studies.

# 6. SUMMARY

Numerical Simulations of turbulent flow and mixing in a piping system that mimics the Fision Product Venting System (FPVS) of a Gas Cooled Fast Reactor were performed. A variety of RANS models and LES models were investigated with low Reynolds numbers, and the results were compared with experimental measurements [1], and result of the DNS stduy [2]. It was found that the RSTM SSG and LES WALE models are required to reproduce TKE (or Reynolds stress) to be similar to that of the DNS results for pipe flows.

One of the easy methods for enhancing the mixing of fluids is to employ a sudden expansion in a flow path. Numerical studies of flow through an axisymmetric sudden expansion were performed using the LES WALE model, revealing that not only the Reynolds number ($Re$) but also the turbulence Intensity (TI) at the inlet flow determine the flow characteristics, accompanying reattachment length, and mixing. The two critical points to demarcate laminar/transition and transition/turbulence regions were demonstrated, and their correlations are suggested as Eqs. 3.8 and 3.9, respectively. A Proper orthogonal decomposition (POD) study was performed. The pattern changes observed in first eigenmode and peak of first eigenvalue obtained were similar to the critical Reynolds number correlation suggested in this study (Table 3.3). Finally, the overall correlation for the reattachment length was proposed. The reattachment length is proportional to Reynolds number in the laminar region (Eqs.3.10, 3.13a, and 3.13b), whereas it is inversely proportional to the Reynolds number in the turbulent region (Eq.3.11, 3.13c, and 3.13d). The transition between laminar and turbulent flows can be expressed as the interpolation of solutions obtained for laminar and turbulent flow regions(Eq. 3.12). Since the reattachment length is heavily correlated to turbulence mixing as discussed in Chapter 4, the universal correlation for the reattachment length proposed in the chapter 3 is the answer for the location where the mixing is completed.

A numerical simulation of gaseous multicomponent flow was conducted to characterize and quantify mixing in fission product venting system (FPVS) which includes flow downstream of an expansion and 90°. By introducing the concept of Absolute Mixing Index (AMI) (Eq.4.5), mixing

of primary coolant and fission product surrogate gases was characterized. The results show that the mixing to be completed at the downstream of the expansion near the reattachment length, where the TKE is an order of magnitude higher than at any other location. A series of 90° elbows does not impact mixing of the multicomponent flow as much as downstream of the expansion. Instead, it elongates the recovery length required for velocity distribution to be fully developed downstream of the pipe bend. This can be a significant problem, especially when a closed loop is considered. This is the technique to show how flow are mixed through a pipe. Based on this the best sampling location for mixing was identified to be between downstream of the sudden expansion and upstream of the first 90° bend.

Lastly, numerical simulations of particulate transport within the rectangular duct were performed with the Lagrangian approach. Using a discrete random walk (DRW) model and Method B (Eq. 5.10), deposition velocity calculated and found to agree well with the results reported in the literature [82, 83, 1] in the gravity dominant region. It was determined that the continuous random walk model (CRW) is required to improve the prediction of particle deposition in a square duct.

# REFERENCES


[1] R. Chavez, D. Orea, T. N. B. Choi, R. Vaghetto, N. Anand, Y. Hassan, and P.Sabharwall, "Experimental study," 2020.

[2] S. Gavrilakis, "Numerical simulation of low-reynolds-number turbulent flow through a straight square duct," *Journal of Fluid Mechanics*, vol. 244, p. 101–129, 1992.

[3] J. G. M. Eggels, F. Unger, M. H. Weiss, J. Westerweel, R. J. Adrian, R. Friedrich, and F. T. M. Nieuwstadt, "Fully developed turbulent pipe flow: a comparison between direct numerical simulation and experiment," *Journal of Fluid Mechanics*, vol. 268, p. 175–210, 1994.

[4] B. Pak, Y. I. Cho, and S. U. Choi, "Separation and reattachment of non-newtonian fluid flows in a sudden expansion pipe," *Journal of Non-Newtonian Fluid Mechanics*, vol. 37, no. 2, pp. 175–199, 1990.

[5] D. J. Latornell and A. Pollard, "Some observations on the evolution of shear layer instabilities in laminar flow through axisymmetric sudden expansions," *The Physics of Fluids*, vol. 29, no. 9, pp. 2828–2835, 1986.

[6] H. Zhang, F. X. Trias, A. Gorobets, Y. Tan, and A. Oliva, "Direct numerical simulation of a fully developed turbulent square duct flow up to re=1200," *International Journal of Heat and Fluid Flow*, vol. 54, pp. 258 – 267, 2015.

[7] S. Pirozzoli, D. Modesti, P. Orlandi, and F. Grasso, "Turbulence and secondary motions in square duct flow," *Journal of Fluid Mechanics*, vol. 840, p. 631–655, 2018.

[8] M. Uhlmann, A. PINELLI, G. KAWAHARA, and A. SEKIMOTO, "Marginally turbulent flow in a square duct," *Journal of Fluid Mechanics*, vol. 588, p. 153–162, 2007.

[9] A. Sekimoto, G. Kawahara, K. Sekiyama, M. Uhlmann, and A. Pinelli, "Turbulence- and buoyancy-driven secondary flow in a horizontal square duct heated from below," *Physics of Fluids*, vol. 23, no. 7, p. 075103, 2011.

[10] C. M. Hrenya, E. J. Bolio, D. Chakrabarti, and J. L. Sinclair, "Comparison of low reynolds number k turbulence models in predicting fully developed pipe flow," *Chemical Engineering Science*, vol. 50, no. 12, pp. 1923 – 1941, 1995.

[11] B. Launder and B. Sharma, "Application of the energy-dissipation model of turbulence to the calculation of flow near a spinning disc," *Letters in Heat and Mass Transfer*, vol. 1, no. 2, pp. 131 – 137, 1974.

[12] C. Lam and K. Bremhorst, "A modified form of the k-$\epsilon$ model for predicting wall turbulence," *Journal of Fluids Engineering*, vol. 103, no. 3, pp. 456 – 460, 1981.

[13] F. Lien and M. Leschziner, "A Pressure-Velocity Solution Strategy for Compressible Flow and Its Application to Shock/Boundary-Layer Interaction Using Second-Moment Turbulence Closure," *Journal of Fluids Engineering*, vol. 115, pp. 717–725, 12 1993.

[14] F.-S. Lien, W. Chen, and M. A. Leschziner, "Low-reynolds-number eddy-viscosity modelling based on non-linear stress-strain/vorticity relations," 1996.

[15] W. Rodi, "A new algebraic relation for calculating the Reynolds stresses," *Gesellschaft Angewandte Mathematik und Mechanik Workshop Paris France*, vol. 56, p. 219, Mar. 1976.

[16] B. Launder, G. Reece, and W. Rodi, "Progress in the development of a reynolds-stress turbulence closure," *Journal of Fluid Mechanics*, vol. 68, no. 3, p. 537–566, 1975.

[17] C. G. Speziale, S. Sarkar, and T. B. Gatski, "Modelling the pressure–strain correlation of turbulence: an invariant dynamical systems approach," *Journal of Fluid Mechanics*, vol. 227, p. 245–272, 1991.

[18] B. J. Daly and F. H. Harlow, "Transport equations in turbulence," *The Physics of Fluids*, vol. 13, no. 11, pp. 2634–2649, 1970.

[19] F. Nicoud and F. Ducros, "Subgrid-scale stress modelling based on the square of the velocity gradient tensor," *Flow, Turbulence and Combustion*, vol. 30, p. 183–200, 1999.

[20] H. Li, N. K. Anand, Y. A. Hassan, and T. Nguyen, "Large eddy simulation of the turbulence fflows of twin parallel jets," *International Journal of Heat and Mass Transfer*, vol. 129, pp. 1263–1273, 2019.

[21] B.-H. Choi, D. Orea, R. Chavez, N. K. Anand, and P. Sabharwall, "Numerical study of multicomponent flow and mixing in a scaled fission product venting system," *Nuclear Engineering and Design*, vol. 391, p. 111714, 2022.

[22] L. Prandtl, "Turbulent flow," tech. rep., University of Zurich, Department of Informatics, 1927.

[23] B. Launder and D. Spalding, "The numerical computation of turbulent flows," *Computer Methods in Applied Mechanics and Engineering*, vol. 3, no. 2, pp. 269 – 289, 1974.

[24]

[25] C. G. Speziale, "On turbulent secondary flows in pipes of noncircular cross-section," *International Journal of Engineering Science*, vol. 20, no. 7, pp. 863–872, 1982.

[26] B.-H. Choi, Y. A. Anand, N. K.and Hassan, and P. Sabharwall, "Large eddy simulation of flow through an axisymmetric sudden expansion," *Physics of Fluids*, vol. 34, no. 6, p. 065117, 2022.

[27] M. C. Chaturvedi, "Flow characteristics of axisymmetric expansions," *Journal of the Hydraulics Division*, vol. 89, no. 3, pp. 61–92, 1963.

[28] B. T. Yang and M. H. Yu, "The flow field in a suddenly enlarged combustion chamber," *AIAA Journal*, vol. 21, no. 1, pp. 92–97, 1983.

[29] L. Khezzar, J. H. Whitelaw, and M. Yianneskis, "Round sudden-expansion flows," *Proceedings of the Institution of Mechanical Engineers, Part C: Journal of Mechanical Engineering Science*, vol. 200, no. 6, pp. 447–455, 1986.

[30] R. M. C. So, "Inlet centerline turbulence effects on reattachment length in axisymmetric sudden-expansion flows," *Experiments in Fluids*, vol. 5, pp. 424–426, 1987.

[31] R. M. C. So and S. A. Ahmed, "Rotation effects on axisymmetric sudden-expansion flows," *Journal of Propulsion and Power*, vol. 4, no. 3, pp. 270–276, 1988.

[32] R. P. Durrett, W. H. Stevenson, and H. D. Thompson, "Radial and Axial Turbulent Flow Measurements With an LDV in an Axisymmetric Sudden Expansion Air Flow," *Journal of Fluids Engineering*, vol. 110, pp. 367–372, 12 1988.

[33] E. Lukács and J. Vad, "Flow topology and loss analysis of a square-to-square sudden expansion relevant to hvac systems: A case study," *Journal of Building Engineering*, vol. 41, p. 102802, 2021.

[34] A. Iribarne, F. Frantisak, R. L. Hummel, and J. W. Smith, "An experimental study of instabilities and other flow properties of a laminar pipe jet," *AIChE Journal*, vol. 18, no. 4, pp. 689–698, 1972.

[35] L. H. Back and E. J. Roschke, "Shear-Layer Flow Regimes and Wave Instabilities and Reattachment Lengths Downstream of an Abrupt Circular Channel Expansion," *Journal of Applied Mechanics*, vol. 39, pp. 677–681, 09 1972.

[36] K. R. Sreenivasan and P. J. Strykowski, "An instability associated with a sudden expansion in a pipe flow," *The Physics of Fluids*, vol. 26, no. 10, pp. 2766–2768, 1983.

[37] T. Mullin, J. R. T. Seddon, M. D. Mantle, and A. J. Sederman, "Bifurcation phenomena in the flow through a sudden expansion in a circular pipe," *Physics of Fluids*, vol. 21, no. 1, p. 014110, 2009.

[38] H. Gach and I. Lowe, "Measuring flow reattachment lengths downstream of a stenosis using mri," *Journal of Magnetic Resonance Imaging*, vol. 12, p. 939–948, 200.

[39] N. Furuichi, Y. Takeda, and M. Kumada, "Spatial structure of the flow through an axisymmetric sudden expansion," *Experiments in Fluids*, vol. 34, pp. 643–650, 2003.

[40] K. Selvam, J. Peixinho, and A. P. Willis, "Localised turbulence in a circular pipe flow with gradual expansion," *Journal of Fluid Mechanics*, vol. 771, p. R2, 2015.

[41] E. Sanmiguel-Rojas, C. del Pino, and C. Gutiérrez-Montes, "Global mode analysis of a pipe flow through a 1:2 axisymmetric sudden expansion," *Physics of Fluids*, vol. 22, no. 7, p. 071702, 2010.

[42] D. Fletcher, S. Maskell, and M. Patrick, "Heat and mass transfer computations for laminar flow in an axisymmetric sudden expansion," *Computers & Fluids*, vol. 13, no. 2, pp. 207–221, 1985.

[43] N. Moallemi and J. Brinkerhoff, "Instability and localized turbulence associated with flow through an axisymmetric sudden expansion," *International Journal of Heat and Fluid Flow*, vol. 72, pp. 161–173, 2018.

[44] E. Sanmiguel-Rojas and T. Mullin, "Finite-amplitude solutions in the flow through a sudden expansion in a circular," *J. Fluid Mech.*, vol. 691, pp. 201–213, 2012.

[45] B. Lebon, M. Q. Nguyen, J. Peixinho, M. S. Shadloo, and A. Hadjadj, "A new mechanism for periodic bursting of the recirculation region in the flow through a sudden expansion in a circular pipe," *Physics of Fluids*, vol. 30, no. 3, p. 031701, 2018.

[46] M. Q. Ngyuen, M. S. Shadloo, A. Hadjadj, and B. Lebon, "Perturbation threshold and hysteresis associated with the transition to turbulence in sudden expansion pipe flow," *International Journal of Heat and Fluid Flow*, vol. 76, pp. 187–196, 2019.

[47] D. V. Shenoy, M. S. Shadloo, J. Peixinho, and A. Hadjadj, "Direct numerical simulations of laminar and transitional flows in diverging pipes," *International Journal of Numerical Methods for Heat & Fluid Flow*, vol. 30, pp. 75–92, 2020.

[48] R. D. Luciano, X. Chen, and D. Bergstrom, "Discretization and perturbations in the simulation of localized turbulence in a pipe with a sudden expansion," *Journal of Fluid Mechanics*, vol. 935, p. A20, 2022.

[49] B. Lebon, J. Peixinho, S. Ishizaka, and Y. Tasaka, "Subcritical transition to turbulence in a sudden circular pipe expansion," *Journal of Fluid Mechanics*, vol. 849, p. 340–354, 2018.

[50] K. Selvam, J. Peixinho, and A. P. Willis, "Flow in a circular expansion pipe flow: effect of a vortex perturbation on localised turbulence," *Fluid Dynamics Research*, vol. 48, p. 061418, Nov 2016.

[51] C. Howard, S. Gupta, A. Abbas, T. A. Langrish, and D. F. Fletcher, "Proper orthogonal decomposition (pod) analysis of cfd data for flow in an axisymmetric sudden expansion," *Chemical Engineering Research and Design*, vol. 123, pp. 333–346, 2017.

[52] P. J. Roache, "Perspective: A method for uniform reporting of grid refinement studies," *Journal of Fluids Engineering*, vol. 116, pp. 405–413, 1994.

[53] K. Taira, S. L. Brunton, S. T. Dawson, C. W. Rowley, T. Colonius, B. J. McKeon, O. T. Schmidt, S. Gordeyev, V. Theofilis, and L. S. Ukeiley, "Modal analysis of fluid flows: An overview," *AIAA J.*, vol. 55, p. 34013, 2017.

[54] J. Lumley, "Coherent structures in turbulence," in *Transition and Turbulence*, pp. 215–242, 1981.

[55] L. Sirovich and M. Kirby, "Low-dimensional procedure for the characterization of human faces," *J. Opt. Soc. Am. A*, vol. 4, no. 3, pp. 519–524, 1987.

[56] D. Drikakis, "Bifurcation phenomena in incompressible sudden expansion flows," *Physics of Fluids*, vol. 9, no. 1, pp. 76–87, 1997.

[57] X. Li and N. Djilali, "On the scaling of separation bubbles," *JSME International Journal Series B Fluids and Thermal Engineering*, vol. 38, pp. 541–548, 1995.

[58] G. Papadopoulos, "A functional relationship for modeling laminar to turbulent flow transitions," *Journal of Fluids Engineering*, vol. 139, 06 2017.

[59] M. Avila and B. Hof, "Nature of laminar-turbulence intermittency in shear flows," *Phys. Rev. E*, vol. 87, p. 063012, Jun 2013.

[60] K. Sudo, M. Sumida, and H. Hibara, "Experimental investigation on turbulent flow in a circular-sectioned 90-degree bend," *Experiments in Fluids*, vol. 25, p. 42–49, 1998.

[61] P. Dutta, S. K. Saha, N. Nandi, and N. Pal, "Numerical study on flow separation in 90° pipe bend under high reynolds number by $k-\epsilon$ modelling," *Engineering Science and Technology, an International Journal*, vol. 19, no. 2, pp. 904–910, 2016.

[62] P. Dutta and N. Nandi, "Numerical study on turbulent separation reattachment flow in pipe bends with different small curvature ratio," *Journal of The Institution of Engineers (India): Series C*, vol. 100, p. 995–1004, 2019.

[63] F. Rütten, W. Schröder, and M. Meinke, "Large-eddy simulation of low frequency oscillations of the dean vortices in turbulent pipe bend flows," *Physics of Fluids*, vol. 17, no. 3, p. 035107, 2005.

[64] A. Kalpakli Vester, R. Örlü, and P. H. Alfredsson, "Turbulent Flows in Curved Pipes: Recent Advances in Experiments and Simulations," *Applied Mechanics Reviews*, vol. 68, no. 5, p. 050802, 2016.

[65] C. Carlsson, E. Alenius, and L. Fuchs, "Swirl switching in turbulent flow through 90° pipe bends," *Physics of Fluids*, vol. 27, no. 8, p. 085112, 2015.

[66] A. Noorani, G. El Khoury, and P. Schlatter, "Evolution of turbulence characteristics from straight to curved pipes," *International Journal of Heat and Fluid Flow*, vol. 41, pp. 16–26, 2013.

[67] L. Hufnagel, J. Canton, R. Örlü, O. Marin, E. Merzari, and P. Schlatter, "The three-dimensional structure of swirl-switching in bent pipe flow," *Journal of Fluid Mechanics*, vol. 835, p. 86–101, 2018.

[68] A. Eckstein and P. P. Vlachos, "Digital particle image velocimetry (DPIV) robust phase correlation," *Measurement Science and Technology*, vol. 20, p. 055401, apr 2009.

[69] A. Eckstein and P. P. Vlachos, "Assessment of advanced windowing techniques for digital particle image velocimetry (DPIV)," *Measurement Science and Technology*, vol. 20, no. 7, p. 075402, 2009.

[70] J. Westerweel, "Efficient detection of spurious vectors in particle image velocimetry data," *Experiments in Fluids*, vol. 16, no. 3, p. 236–247, 1994.

[71] B. H. Timmins, B. W. Wilson, B. L. Smith, and P. Vlachos, "A method for automatic estimation of instantaneous local uncertainty in particle image velocimetry measurements," *Experiments in Fluids*, vol. 53, no. 4, pp. 1133–1147, 2012.

[72] A. Sciacchitano, "Uncertainty quantification in particle image velocimetry," *Measurement Science and Technology*, vol. 30, p. 092001, jul 2019.

[73] B. S. Hyun, R. Balachandar, K. Yu, and V. C. Patel, "Assessment of piv to measure mean velocity and turbulence in open-channel flow," *Experiments in Fluids*, vol. 35, no. 3, p. 262–267, 2003.

[74] S. S. Elahi, E. A. Lange, and S. P. Lynch, *Experimental Measurements of Turbulent Junction Flow Using High Speed Stereo PIV and IR Thermography*. 2017.

[75] F. Fischer, A. Andris, W. Lippmann, and A. Hurtado, "Particle deposition by thermophoresis under high-temperature conditions in a helium flow," *Journal of Nuclear Engineering and Radiation Science*, vol. 4, no. 4, p. 041020, 2018.

[76] H. Zhang and G. Ahmadi, "Aerosol particle transport and deposition in vertical and horizontal turbulent duct flows," *Journal of Fluid Mechanics*, vol. 406, p. 55–80, 2000.

[77] L. Tian and G. Ahmadi, "Particle deposition in turbulent duct flows—comparisons of different model predictions," *Journal of Aerosol Science*, vol. 38, no. 4, pp. 377 – 397, 2007.

[78] D. J. Thomson, "Criteria for the selection of stochastic models of particle trajectories in turbulent flows," *Journal of Fluid Mechanics*, vol. 180, p. 529–556, 1987.

[79] G. Sharma and D. J. Phares, "Turbulent transport of particles in a straight square duct," *International Journal of Multiphase Flow*, vol. 32, no. 7, pp. 823 – 837, 2006.

[80] A. Dehbi, "A cfd model for particle dispersion in turbulent boundary layer flows," *Nuclear Engineering and Design*, vol. 238, pp. 707–715, 2008.

[81] A. Guha, "A unified eulerian theory of turbulent deposition to smooth and rough surfaces," *Journal of Aerosol Science*, vol. 28, no. 8, pp. 1517 – 1537, 1997.

[82] N. Wood, "A simple method for the calculation of turbulent deposition to smooth and rough surfaces," *Journal of Aerosol Science*, vol. 12, no. 3, pp. 275 – 290, 1981.

[83] T. Barth, G. Lecrivain, and U. Hampel, "Particle deposition study in a horizontal turbulent duct flow using optical microscopy and particle size spectrometry," *Journal of Aerosol Science*, vol. 60, pp. 47 – 54, 2013.

[84] A. A. Mofakham and G. Ahmadi, "Particles dispersion and deposition in inhomogeneous turbulent flows using continuous random walk models," *Physics of Fluids*, vol. 31, no. 8, p. 083301, 2019.

[85] A. A. Mofakham and G. Ahmadi, "On random walk models for simulation of particle-laden turbulent flows," *International Journal of Multiphase Flow*, vol. 122, p. 103157, 2020.

[86] J. Cleaver and B. Yates, "A sub layer model for the deposition of particles from a turbulent flow," *Chemical Engineering Science*, vol. 30, no. 8, pp. 983 – 992, 1975.

[87] *Deposition Velocity and Penetration Efficiency in a Square Channel Using a Lagrangian-Based Modeling Approach*, vol. Volume 1: Beyond Design Basis; Codes and Standards; Computational Fluid Dynamics (CFD); Decontamination and Decommissioning; Nuclear Fuel and Engineering; Nuclear Plant Engineering of *International Conference on Nuclear Engineering*, 08 2020. V001T03A026.

[88] A. Dehbi, "Validation against dns statistics of the normalized langevin model for particle transport in turbulent channel flows," *Powder Technology*, vol. 200, no. 1, pp. 60–68, 2010.

APPENDIX A

PROGRAM CODE

Appendix A includes OpenFOAM v7 code used for the parametric simulation of flow through an axisymmetric sudden expansion in the Chapter 3.

## A.1 File Tree

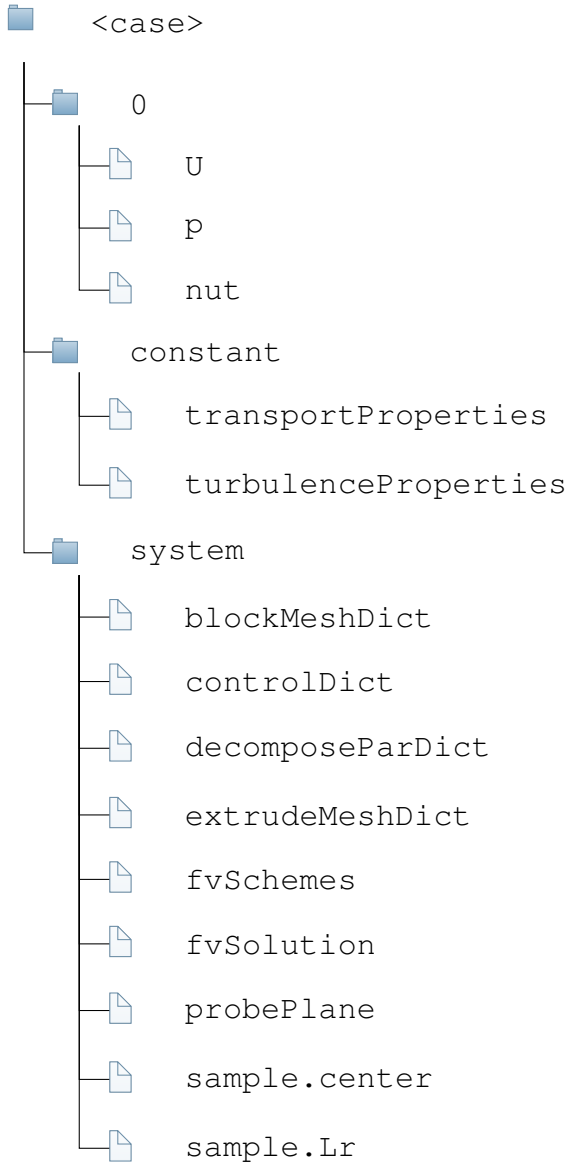

## A.2 OpenFoam Code

**<case>/0/U**

```
/*--------------------------------*- C++ -*----------------------------------*\
  =========                 |
  \\      /  F ield         | OpenFOAM: The Open Source CFD Toolbox
   \\    /   O peration     | Website:  https://openfoam.org
    \\  /    A nd           | Version:  6
     \\/     M anipulation  |
\*---------------------------------------------------------------------------*/
FoamFile
{
    version     2.0;
    format      ascii;
    class       volVectorField;
    location    "0";
    object      U;
}
// * * * * * * * * * * * * * * * * * * * * * * * * * * * * * * * * * * * * //

dimensions      [0 1 -1 0 0 0 0];

internalField   uniform (0 0 0);

boundaryField
{

    inlet
    {
        type            codedFixedValue;
        value           uniform (0 0 #calc "0.6432/1000*650");
        redirectType    inletProfile;
        name            inletProfile;

        codeInclude
        #{
        #include "Random.H"
        #};

        codeOptions
        #{
            -I$(LIB_SRC)/finiteVolume/lnInclude
        #};

        codeLibs
        #{
            -lfiniteVolume
        #};

        code
        #{
         const fvPatch& boundaryPatch = patch(); //generic
         const vectorField& Cf = boundaryPatch.Cf(); //generic
         vectorField field = *this; //*this;
```

```
52          vectorField referenceField = field;
53          Random randObj(clock::getTime());
54          Field<vector> randomField(this->size());
55
56          const scalar TI      = 0.01;
57          const vector fluctuationScale = TI*vector(1, 1, 1);
58          const scalar alpha   = 0.1;
59          const scalar rmsCorr = sqrt(12*(2*alpha - sqr(alpha)))/alpha;
60
61          // definition of the maximum velocity
62          const scalar Umean   = 0.6432/1000*650;
63          const scalar Umax    = Umean*2;
64          // radius of small pipe
65          const scalar IR      = 0.025/2;
66
67          // loop over all the patch faces
68          forAll(referenceField, faceI)
69          {
70          // x coordinate of the faces i
71          const scalar x = Cf[faceI].x()-0*0.0254;
72          // y coordinate of the faces i
73          const scalar y = Cf[faceI].y();
74          // compute radius from center patch
75          const scalar radius = pow(x*x+y*y,0.5);
76          referenceField[faceI] = vector(0, 0, Umax*(1-(radius/IR)*(radius/IR)));
77          randomField[faceI] = cmptMultiply(fluctuationScale, randObj.sample01<vector>()
78  -0.5*vector(1,1,1));
79          //randomField[faceI] = cmptMultiply(fluctuationScale,
80          //2*randObj.sample01<vector>()-vector(1,1,1));
81          }
82
83          field =
84                (1 - alpha)*field
85              + alpha*
86                (
87                    referenceField
88                  + rmsCorr*randomField*mag(referenceField)
89                );
90
91          operator==(field);
92        #};
93      }
94
95      outlet
96      {
97          type            inletOutlet;
98          value           $internalField;
99          inletValue      uniform (0 0 0);
100     }
101
102     "(wall0|wall1)"
103     {
104         type        noSlip;
105     }
106 }
```

```
109 // ************************************************************************* //
```

**<case>/0/p**

```
1  /*--------------------------------*- C++ -*----------------------------------*\
2    =========                 |
3    \\      /  F ield         | OpenFOAM: The Open Source CFD Toolbox
4     \\    /   O peration     | Website:  https://openfoam.org
5      \\  /    A nd           | Version:  6
6       \\/     M anipulation  |
7  \*---------------------------------------------------------------------------*/
8  FoamFile
9  {
10     version     2.0;
11     format      ascii;
12     class       volScalarField;
13     object      p;
14 }
15 // * * * * * * * * * * * * * * * * * * * * * * * * * * * * * * * * * * * * * * * //

17 dimensions      [0 2 -2 0 0 0 0];

19 internalField   uniform 0;

21 boundaryField
22 {

24     inlet
25     {
26         type            zeroGradient;
27     }

29     outlet
30     {
31         type            fixedValue;
32         value           uniform 0;
33     }

35     "(wall0|wall1)"
36     {
37         type            zeroGradient;
38     }
39 }


42 // ************************************************************************* //
```

**<case>/0/nut**

```
1  /*--------------------------------*- C++ -*----------------------------------*\
2    =========                 |
3    \\      /  F ield         | OpenFOAM: The Open Source CFD Toolbox
4     \\    /   O peration     | Website:  https://openfoam.org
```

```
\\    /    A nd           | Version:  6
 \\/     M anipulation  |
\*---------------------------------------------------------------------------*/
FoamFile
{
    version     2.0;
    format      ascii;
    class       volScalarField;
    location    "0";
    object      nut;
}
// * * * * * * * * * * * * * * * * * * * * * * * * * * * * * * * * * * * * * * * //

dimensions      [0 2 -1 0 0 0 0];

internalField   uniform 1e-15;

boundaryField
{
    inlet
    {
        type            calculated;
        value           uniform 0;
    }
    outlet
    {
        type            calculated;
        value           uniform 0;
    }

    "(wall0|wall1)"
    {
        type            calculated;
        value           uniform 0;
    }
}


// ************************************************************************* //
```

**<case>/constant/transportProperties**

```
/*--------------------------------*- C++ -*----------------------------------*\
  =========                 |
  \\      /  F ield         | OpenFOAM: The Open Source CFD Toolbox
   \\    /   O peration     | Website:  https://openfoam.org
    \\  /    A nd           | Version:  6
     \\/     M anipulation  |
\*---------------------------------------------------------------------------*/
FoamFile
{
    version     2.0;
    format      ascii;
    class       dictionary;
    location    "constant";
```

```
    object      transportProperties;
}
// * * * * * * * * * * * * * * * * * * * * * * * * * * * * * * * * * * * * * * * * * * * * //

transportModel  Newtonian;

nu              [0 2 -1 0 0 0 0] 1.608e-05;
rhoInf          [ 1 -3 0 0 0 0 0 ] 1.164;

// ************************************************************************* //
```

**<case>/constant/turbulenceProperties**

```
/*--------------------------------*- C++ -*----------------------------------*\
  =========                 |
  \\      /  F ield         | OpenFOAM: The Open Source CFD Toolbox
   \\    /   O peration     | Website:  https://openfoam.org
    \\  /    A nd           | Version:  6
     \\/     M anipulation  |
\*---------------------------------------------------------------------------*/
FoamFile
{
    version     2.0;
    format      ascii;
    class       dictionary;
    location    "constant";
    object      turbulenceProperties;
}
// * * * * * * * * * * * * * * * * * * * * * * * * * * * * * * * * * * * * * * * * * * * * //

simulationType LES;

LES
{
    LESModel        WALE;
    turbulence      on;
    printCoeffs     on;
    delta           cubeRootVol;

    cubeRootVolCoeffs
    {
        deltaCoeff      1;
    }

    PrandtlCoeffs
    {
        delta           cubeRootVol;
        cubeRootVolCoeffs
        {
            deltaCoeff      1;
        }

        smoothCoeffs
        {
            delta           cubeRootVol;
```

```
            cubeRootVolCoeffs
            {
                deltaCoeff      1;
            }

            maxDeltaRatio   1.1;
        }

        Cdelta          0.158;
    }

    vanDriestCoeffs
    {
        delta           cubeRootVol;
        cubeRootVolCoeffs
        {
            deltaCoeff      1;
        }

        smoothCoeffs
        {
            delta           cubeRootVol;
            cubeRootVolCoeffs
            {
                deltaCoeff      1;
            }

            maxDeltaRatio   1.1;
        }

        Aplus           26;
        Cdelta          0.158;
    }

    smoothCoeffs
    {
        delta           cubeRootVol;
        cubeRootVolCoeffs
        {
            deltaCoeff      1;
        }

        maxDeltaRatio   1.1;
    }
}


// ************************************************************************* //
```

**<case>/system/blockMeshDict**

```
/*--------------------------------*- C++ -*----------------------------------*\
  =========                 |
  \\      /  F ield         | OpenFOAM: The Open Source CFD Toolbox
   \\    /   O peration     | Website:  https://openfoam.org
```

```
\\    /    A nd           | Version:  6
 \\/     M anipulation  |
\*---------------------------------------------------------------------------*/

FoamFile
{
    version     2.0;
    format      ascii;
    class       dictionary;
    object      blockMeshDict;
}

// * * * * * * * * * * * * * * * * * * * * * * * * * * * * * * * * * * * * * * * * * * * * //
convertToMeters 0.001;

pr1     #calc "25.0 / 2";     //innercircle size
pr2     #calc "50.0 / 2";

pr0     #calc "$pr1 * 0.65";

qr2     #calc "-1*$pr2";
qr1     #calc "-1*$pr1";
qr0     #calc "-1*$pr0";

sr2     #calc "$pr2 /pow(2,1.0/2.0)";
sr1     #calc "$pr1 /pow(2,1.0/2.0)";
sr0     #calc "$pr0 /pow(2,1.0/2.0)*0.8";

tr2     #calc "-1*$sr2";
tr1     #calc "-1*$sr1";
tr0     #calc "-1*$sr0";
/*
r2 = 1.0/2;
r1 = r2*0.65;
q2 = r2/sqrt(2);
q1 = r1/sqrt(2)*0.8;

pa2 = [-r2 0 0 1; 0 r2 0 1; r2 0 0 1; 0 -r2 0 1]';
pa1 = [-r1 0 0 1; 0 r1 0 1; r1 0 0 1; 0 -r1 0 1]';
pb2 = [-q2 +q2 0 1; +q2 +q2 0 1; +q2 -q2 0 1; -q2 -q2 0 1]';
pb1 = [-q1 +q1 0 1; +q1 +q1 0 1; +q1 -q1 0 1; -q1 -q1 0 1]';
*/

Mx      16;
My0     8;
My1     12;

Mz0     450;
z1      1500;

//Mesh11  ((0.15 0.25 5) (0.7 0.5 1) (0.15 0.25 0.2));
Mesh11  ((0.7 0.5 1) (0.15 0.25 0.2));
Mesh12  ((0.15 0.25 5) (0.7 0.5 1));        //outer

Mesh21  ((0.65 0.5 1) (0.35 0.5 0.2));
```

```
Mesh22   ((0.35  0.5  5) (0.65  0.5  1));

MzS01    1;

vertices
(
    ($qr0   0     0)  // 0
    (0      $pr0  0)  // 1
    ($pr0   0     0)  // 2
    (0      $qr0  0)  // 3

    ($qr1   0     0)  // 4
    (0      $pr1  0)  // 5
    ($pr1   0     0)  // 6
    (0      $qr1  0)  // 7

    ($qr2   0     0)  // 8
    (0      $pr2  0)  // 9
    ($pr2   0     0)  // 10
    (0      $qr2  0)  // 11

    (0  0  0)  // 12
    (0  0  0)  // 13
    (0  0  0)  // 14
    (0  0  0)  // 15

    (0  0  0)  // 16
    (0  0  0)  // 17
    (0  0  0)  // 18
    (0  0  0)  // 19

    ($qr0   0     $z1)  // 20
    (0      $pr0  $z1)  // 21
    ($pr0   0     $z1)  // 22
    (0      $qr0  $z1)  // 23

    ($qr1   0     $z1)  // 24
    (0      $pr1  $z1)  // 25
    ($pr1   0     $z1)  // 26
    (0      $qr1  $z1)  // 27

    ($qr2   0     $z1)  // 28
    (0      $pr2  $z1)  // 29
    ($pr2   0     $z1)  // 30
    (0      $qr2  $z1)  // 31
);

blocks
(
    // cylinder straigh
    hex (0 1 5 4 20 21 25 24)   ($Mx $My0 $Mz0) simpleGrading (1 $Mesh21 $MzS01)
    hex (1 2 6 5 21 22 26 25)   ($Mx $My0 $Mz0) simpleGrading (1 $Mesh21 $MzS01)
    hex (7 6 2 3 27 26 22 23)   ($Mx $My0 $Mz0) simpleGrading (1 $Mesh22 $MzS01)
    hex (4 7 3 0 24 27 23 20)   ($Mx $My0 $Mz0) simpleGrading (1 $Mesh22 $MzS01)
```

```
    hex (0 3 2 1 20 23 22 21)  ($Mx $Mx $Mz0) simpleGrading (1 1 $MzS01)

    hex (4   5  9 8 24 25 29 28)  ($Mx $My1 $Mz0) simpleGrading (1 $Mesh11 $MzS01)
    hex (5   6 10 9 25 26 30 29)  ($Mx $My1 $Mz0) simpleGrading (1 $Mesh11 $MzS01)
    hex (11 10  6 7 31 30 26 27)  ($Mx $My1 $Mz0) simpleGrading (1 $Mesh12 $MzS01)
    hex (8  11  7 4 28 31 27 24)  ($Mx $My1 $Mz0) simpleGrading (1 $Mesh12 $MzS01)
);

edges
(

    arc     0     1       ($tr0 $sr0 0)
    arc     1     2       ($sr0 $sr0 0)
    arc     2     3       ($sr0 $tr0 0)
    arc     3     0       ($tr0 $tr0 0)

    arc     4     5       ($tr1 $sr1 0)
    arc     5     6       ($sr1 $sr1 0)
    arc     6     7       ($sr1 $tr1 0)
    arc     7     4       ($tr1 $tr1 0)

    arc     8      9       ($tr2 $sr2 0)
    arc     9     10       ($sr2 $sr2 0)
    arc     10    11       ($sr2 $tr2 0)
    arc     11     8       ($tr2 $tr2 0)

    arc     20     21       ($tr0 $sr0 $z1)
    arc     21     22       ($sr0 $sr0 $z1)
    arc     22     23       ($sr0 $tr0 $z1)
    arc     23     20       ($tr0 $tr0 $z1)

    arc     24     25       ($tr1 $sr1 $z1)
    arc     25     26       ($sr1 $sr1 $z1)
    arc     26     27       ($sr1 $tr1 $z1)
    arc     27     24       ($tr1 $tr1 $z1)

    arc     28     29       ($tr2 $sr2 $z1)
    arc     29     30       ($sr2 $sr2 $z1)
    arc     30     31       ($sr2 $tr2 $z1)
    arc     31     28       ($tr2 $tr2 $z1)

);


boundary
(
    inlet
    {
        type mappedPatch;
        sampleMode     nearestCell;
        sampleRegion   region0;
        samplePatch    none;
        offset         (0 0 1.2);
        faces
```

```
        (
            (0 3 2 1)

            (0 4 5 1)
            (5 6 2 1)
            (3 2 6 7)
            (0 3 7 4)
        );
    }

    wall0
    {
        type wall;
        faces
        (
         (5 4 9 8)
         (5 6 10 9)
         (11 10 6 7)
         (8 11 7 4)
        );
    }

    outlet
    {
        type patch;
        faces
        (
(20 23 22 21)

(20 24 25 21)
(25 26 22 21)
(23 22 26 27)
(20 23 27 24)

(25 24 29 28)
(25 26 30 29)
(31 30 26 27)
(28 31 27 24)

        );
    }

    wall1
    {
        type wall;
        faces
        (

(8 9 29 28)
(9 10 30 29)
(10 11 31 30)
(11 8 28 31)

/*
(4 7 27 24)
```

```
(7 6 26 27)
(5 6 26 25)
(4 5 25 24)
*/
        );
    }
);

// ************************************************************************* //
// ************************************************************************* //
```

**<case>/system/extrudeMeshDict**

```
/*--------------------------------*- C++ -*----------------------------------*\
  =========                 |
  \\      /  F ield         | OpenFOAM: The Open Source CFD Toolbox
   \\    /   O peration     | Website:  https://openfoam.org
    \\  /    A nd           | Version:  7
     \\/     M anipulation  |
\*---------------------------------------------------------------------------*/
FoamFile
{
    version     2.0;
    format      ascii;
    class       dictionary;
    object      extrudeProperties;
}
// * * * * * * * * * * * * * * * * * * * * * * * * * * * * * * * * * * * * * //

constructFrom mesh;
sourceCase "$FOAM_CASE";
sourcePatches (inlet);

flipNormals         false;
extrudeModel        linearDirection;

nLayers             35;
expansionRatio      1.0;

linearDirectionCoeffs
{
    axisPt          (0 0 0);
    direction       (0 0 -1);
    thickness       #calc "25*0.001*5"; //84
}

mergeFaces false;

// * * * * * * * * * * * * * * * * * * * * * * * * * * * * * * * * * * * * * //
```

**<case>/system/decomposeParDict**

```
/*--------------------------------*- C++ -*----------------------------------*\
| =========                 |                                                 |
| \\      /  F ield         | OpenFOAM: The Open Source CFD Toolbox           |
```

```
|  \\      /   O peration      | Version:   plus                                 |
|   \\    /    A nd            | Web:       www.OpenFOAM.com                     |
|    \\/      M anipulation    |                                                 |
\*---------------------------------------------------------------------------*/
FoamFile
{
    version      2.0;
    format       ascii;
    class        dictionary;
    object       decomposeParDict;
}
// * * * * * * * * * * * * * * * * * * * * * * * * * * * * * * * * * * * * * * * * * * * * * * * * * * * * * * * * * * * * * * * * //

numberOfSubdomains 96;
method             scotch; // hierarchical;

hierarchicalCoeffs
{
    n                (2 2 18);
    delta            0.00001;
    order            zxy;
}

distributed      no;

roots            ( );



// ************************************************************************* //
```

**<case>/system/fvSchemes**

```
/*--------------------------------*- C++ -*----------------------------------*\
  =========                 |
  \\      /  F ield         | OpenFOAM: The Open Source CFD Toolbox
   \\    /   O peration     | Website:  https://openfoam.org
    \\  /    A nd           | Version:  6
     \\/     M anipulation  |
\*---------------------------------------------------------------------------*/
FoamFile
{
    version      2.0;
    format       ascii;
    class        dictionary;
    location     "system";
    object       fvSchemes;
}
// * * * * * * * * * * * * * * * * * * * * * * * * * * * * * * * * * * * * * * * * * * * * * * * * * * * * * * * * * * * * * * * * //

ddtSchemes
{
    default          backward;   // backward;
}
```

```
gradSchemes
{
    default         Gauss linear;
}

divSchemes
{
    default          none;
    div(phi,U)       Gauss LUST grad(U);
    div(phi,R)       Gauss limitedLinear 1;
    div(phi,k)       Gauss limitedLinear 1;
    div(phi,epsilon) Gauss limitedLinear 1;
    div(phi,omega)   Gauss limitedLinear 1;
    div(phi,v2)      Gauss limitedLinear 1;
    div(phi,K)       Gauss limitedLinear 1;
    div(phi,h)       Gauss limitedLinear 1;
    div(phi,B)      Gauss limitedLinear 1;
    div(phi,nuTilda) Gauss limitedLinear 1;

    div((nu*dev2(T(grad(U))))     Gauss linear;
    div((nuEff*dev2(T(grad(U))))) Gauss linear;
    div(((rho*nuEff)*dev2(T(grad(U))))) Gauss linear;

    div(nonlinearStress)          Gauss linear;
    div(R)                        Gauss linear;
    div(B)                        Gauss linear;

    div(phi,Yi)          Gauss limitedLinear01 1;
    div(phi,Yi_h)        Gauss limitedLinear01 1;
}

laplacianSchemes
{
    default         Gauss linear corrected;
}

interpolationSchemes
{
    default         linear;
}

snGradSchemes
{
    default         corrected;
}

wallDist
{
    method meshWave;
}


// ************************************************************************* //
```

**<case>/system/fvSolution**

```
/*--------------------------------*- C++ -*----------------------------------*\
  =========                 |
  \\      /  F ield         | OpenFOAM: The Open Source CFD Toolbox
   \\    /   O peration     | Website:  https://openfoam.org
    \\  /    A nd           | Version:  6
     \\/     M anipulation  |
\*---------------------------------------------------------------------------*/
FoamFile
{
    version     2.0;
    format      ascii;
    class       dictionary;
    location    "system";
    object      fvSolution;
}
// * * * * * * * * * * * * * * * * * * * * * * * * * * * * * * * * * * * * * //

solvers
{
    "(p|rho)"
    {
        solver          GAMG;
        tolerance       1e-5;
        relTol          0.001;
        smoother        GaussSeidel;
    }

    "(p|rho)Final"
    {
        $p;
        tolerance       1e-6;
        relTol          0;
    }

    "(R|U|k|epsilon|omega|f|v2|nuTilda|h|Yi)"
    {
        solver          smoothSolver;
        smoother        GaussSeidel;
        tolerance       1e-6;
        relTol          0.001;
    }


    "(R|U|k|epsilon|omega|f|v2|nuTilda|h|Yi)Final"
    {
        $U;
        tolerance       1e-6;
        relTol          0;
    }
}

PIMPLE
{
    momentumPredictor no;
    nOuterCorrectors 5;
```

```
    nCorrectors     2;
    nNonOrthogonalCorrectors 1;

    outerCorrectorResidualControl
    {
        "(U|p)"
        {
            relTol 0;
            tolerance 0.001;
        }
    }
}

relaxationFactors
{
    fields
    {
        p       1;
        pFinal  1;  // Last outer loop
    }

    equations
    {
        U       1;
        UFinal  1;  // Last outer loop
    }
}
```

**<case>/system/controlDict**

```
/*--------------------------------*- C++ -*----------------------------------*\
  =========                 |
  \\      /  F ield         | OpenFOAM: The Open Source CFD Toolbox
   \\    /   O peration     | Website:  https://openfoam.org
    \\  /    A nd           | Version:  7
     \\/     M anipulation  |
\*---------------------------------------------------------------------------*/
FoamFile
{
    version     2.0;
    format      ascii;
    class       dictionary;
    location    "system";
    object      controlDict;
}
// * * * * * * * * * * * * * * * * * * * * * * * * * * * * * * * * * * * * //

application     pimpleFoam;

startFrom       latestTime;

startTime       0;

stopAt          endTime;
```

```
endTime         60;

deltaT          0.0004;

writeControl    timeStep;

writeInterval   2500;

purgeWrite      3;

writeFormat     ascii;

writePrecision  6;

writeCompression on;

timeFormat      general;

timePrecision   6;

runTimeModifiable true;

OptimisationSwitches
{
        fileHandler collated;
}

cacheTemporaryObjects
(

);

functions
{
    fieldAverage1
    {
        type                fieldAverage;
        libs                ("libfieldFunctionObjects.so");
        writeControl        writeTime;

        restartOnRestart    false;
        restartOnOutput     false;
        periodicRestart     false;
        //restartPeriod     5;
        timeStart           10;

        fields
        (
            U
            {
                mean        on;
                prime2Mean  on;
                base        time;
            }
```

```
81              p
82              {
83                  mean            on;
84                  prime2Mean      off;
85                  base            time;
86              }
87          );
88      }
89
90      force1
91      {
92          type            forces;
93          libs            ("libforces.so");
94          writeControl    timeStep;
95          writeInterval   1;
96
97          patches
98          (
99              wall1
100         );
101
102         CofR (0 0 0);
103         rho           rhoInf;
104         rhoInf        1.164;
105     }
106
107     surfaces1
108     {
109         type             surfaces;
110         libs             ("libsampling.so");
111         writeControl     timeStep;
112         writeInterval    5;
113         timeStart        10;
114
115         surfaceFormat    vtk;
116         interpolationScheme cellPoint;
117
118         fields         (U);
119
120         surfaces
121         (
122             yNormal
123             {
124                 type            cuttingPlane;
125                 planeType       pointAndNormal;
126                 pointAndNormalDict
127                 {
128                 basePoint       (0 0 0);
129                 normalVector    (0 1 0);
130                 }
131                 interpolate     true;
132             }
133         );
134     }
```

```
    #includeFunc probePlane

/*---------------------------------------------------------------------------
    writeObjects1
    {
        type        writeObjects;
        libs        ("libutilityFunctionObjects.so");

        writeControl    timeStep;
        writeInterval   10;

        writeOption   anyWrite;

        objects       ( U p );
    }
---------------------------------------------------------------------------*/

}


// ************************************************************************* //
```

**<case>/system/probePlane**

```
/*--------------------------------*- C++ -*----------------------------------*\
  =========                 |
  \\      /  F ield         | OpenFOAM: The Open Source CFD Toolbox
   \\    /   O peration     | Website:  https://openfoam.org
    \\  /    A nd           | Version:  7
     \\/     M anipulation  |
\*---------------------------------------------------------------------------*/
FoamFile
{
    version     2.0;
    format      ascii;
    class       dictionary;
    location    "system";
    object      probe;
}
// * * * * * * * * * * * * * * * * * * * * * * * * * * * * * * * * * * * * //
type     probes;
libs     ("libsampling.so");
interpolationScheme cellPoint;
writeControl     timeStep;
writeInterval    5;
startTime        10;
fields           (U p);
probeLocations (
   ( 0.00000 -0.02499 0.00000 )
   ( 0.00000 -0.02400 0.00000 )
   ( 0.00000 -0.02300 0.00000 )
   ( 0.00000 -0.02200 0.00000 )
   ( 0.00000 -0.02100 0.00000 )
   ( 0.00000 -0.02000 0.00000 )
   ( 0.00000 -0.01900 0.00000 )
```

```
    ( 0.00000 -0.01800 0.00000 )
    ( 0.00000 -0.01700 0.00000 )
    ( 0.00000 -0.01600 0.00000 )
    ( 0.00000 -0.01500 0.00000 )
    ( 0.00000 -0.01400 0.00000 )
    ( 0.00000 -0.01300 0.00000 )
    ( 0.00000 -0.01200 0.00000 )
    ( 0.00000 -0.01100 0.00000 )
    ( 0.00000 -0.01000 0.00000 )
    ( 0.00000 -0.00900 0.00000 )
    ( 0.00000 -0.00800 0.00000 )
    ( 0.00000 -0.00700 0.00000 )
    ( 0.00000 -0.00600 0.00000 )
    ( 0.00000 -0.00500 0.00000 )
    ( 0.00000 -0.00400 0.00000 )
    ( 0.00000 -0.00300 0.00000 )
    ( 0.00000 -0.00200 0.00000 )
    ( 0.00000 -0.00100 0.00000 )
    ( 0.00000 0.00000 0.00000 )
    ( 0.00000 0.00100 0.00000 )
    ( 0.00000 0.00200 0.00000 )
    ( 0.00000 0.00300 0.00000 )
    ( 0.00000 0.00400 0.00000 )
    ( 0.00000 0.00500 0.00000 )
    ( 0.00000 0.00600 0.00000 )
    ( 0.00000 0.00700 0.00000 )
    ( 0.00000 0.00800 0.00000 )
    ( 0.00000 0.00900 0.00000 )
    // ...
    //continue ....
    // ...
    ( 0.00000 0.02100 1.50000 )
    ( 0.00000 0.02200 1.50000 )
    ( 0.00000 0.02300 1.50000 )
    ( 0.00000 0.02400 1.50000 )
    ( 0.00000 0.02499 1.50000 )
);
```

**<case>/system/sample.center**

```
/*--------------------------------*- C++ -*----------------------------------*\
  =========                 |
  \\      /  F ield         | OpenFOAM: The Open Source CFD Toolbox
   \\    /   O peration     | Website:  https://openfoam.org
    \\  /    A nd           | Version:  7
     \\/     M anipulation  |
\*---------------------------------------------------------------------------*/
FoamFile
{
    version     2.0;
    format      ascii;
    class       dictionary;
    location    "system";
    object      sample.center;
}
```

```
// * * * * * * * * * * * * * * * * * * * * * * * * * * * * * * * * * * * * * * * * * //

type sets;
libs            ("libsampling.so");

interpolationScheme cellPoint;

setFormat       raw;

sets
(
    line_centreProfile
    {
        type    lineCell;
        axis    distance;
        start   ( 0 0 0);
        end     ( 0 0 0.6 );
    }
);

fields          ( p pMean U UMean );

// postProcess -func sample.center -latestTime
// ************************************************************************
```

**<case>/system/sample.Lr**

```
/*--------------------------------*- C++ -*----------------------------------*\
  =========                 |
  \\      /  F ield         | OpenFOAM: The Open Source CFD Toolbox
   \\    /   O peration     | Website:  https://openfoam.org
    \\  /    A nd           | Version:  7
     \\/     M anipulation  |
\*---------------------------------------------------------------------------*/
FoamFile
{
    version     2.0;
    format      ascii;
    class       dictionary;
    location    "system";
    object      sample.Lr;
}
// * * * * * * * * * * * * * * * * * * * * * * * * * * * * * * * * * * * * * * * * * //
type    sets;
libs    ("libsampling.so");
interpolationScheme cellPatchConstrained;
setFormat       raw;
fields          (U UMean);
sets (

    Axial_rhWall.000
    {
        type    lineCell;
        axis    distance;
        start   (0.02495000 0.00000000 0.00000000);
```

```
        end     (0.02495000 0.00000000 2.00000000);
    }

    Axial_rhWall.005
    {
        type    lineCell;
        axis    distance;
        start   (0.02485506 0.00217454 0.00000000);
        end     (0.02485506 0.00217454 2.00000000);
    }

    Axial_rhWall.010
    {
        type    lineCell;
        axis    distance;
        start   (0.02457095 0.00433252 0.00000000);
        end     (0.02457095 0.00433252 2.00000000);
    }

    Axial_rhWall.015
    {
        type    lineCell;
        axis    distance;
        start   (0.02409985 0.00645754 0.00000000);
        end     (0.02409985 0.00645754 2.00000000);
    }

    //continued   ...

    Axial_rhWall.350
    {
        type    lineCell;
        axis    distance;
        start   (0.02457095 -0.00433252 0.00000000);
        end     (0.02457095 -0.00433252 2.00000000);
    }

    Axial_rhWall.355
    {
        type    lineCell;
        axis    distance;
        start   (0.02485506 -0.00217454 0.00000000);
        end     (0.02485506 -0.00217454 2.00000000);
    }
);
```